Insights into Proton-Coupled Electron Transfer from Computation

A DISSERTATION
SUBMITTED TO THE FACULTY OF
UNIVERSITY OF MINNESOTA
BY

Makenzie R. Provorse

IN PARTIAL FULFILLMENT OF THE REQUIREMENTS
FOR THE DEGREE OF
DOCTOR OF PHILOSOPHY

Professor Jiali Gao, Adviser

June 2014

Abstract

Proton-coupled electron transfer (PCET) is utilized throughout Nature to facilitate essential biological processes, such as photosynthesis, cellular respiration, and DNA replication and repair. The general approach to studying PCET processes is based on a two-dimensional More O'Ferrall-Jencks diagram in which electron transfer (ET) and proton transfer (PT) occur in a sequential or concerted fashion. Experimentally, it is difficult to discern the contributing factors of concerted PCET mechanisms. Several theoretical approaches have arisen to qualitatively and quantitatively investigate these reactions. Here, we present a multistate density functional theory (MSDFT) method to efficiently and accurately model PCET mechanisms. The MSDFT method is validated against experimental and computational data previously reported on the hydrogen exchange reactions of the isoelectronic series of $(PhX)_2H\bullet$ (X = O, NH, CH_2) and a model complex specifically designed to study long-range ET through a hydrogen-bonded salt-bridge interface. MSDFT is shown to provide both qualitatively and quantitatively model PCET reactions. Further application of this method to the hydrogen atom abstraction of ascorbate by a nitroxyl radical demonstrates the sensitivity of the thermodynamic and kinetic properties to solvent effects. In particular, the origin of the unusual kinetic isotope effect is investigated. Lastly, the MSDFT is employed in a combined quantum mechanical/molecular mechanical (QM/MM) approach to explicitly model PCET in condensed phases.

Table of Contents

List of Tables

List of Figures

List of Abbreviations

BLDFT	Block-localized density functional theory
BLKS	Block-localized Kohn-Sham
BO	Born-Oppenheimer
CASSCF	Complet active space self-consistent field
CDC	Consistent diabatic configuration
CPET	Coupled proton-electron transfer
CSF	Configuration state function
CT	Charge transfer
CVT	Canonical variational transition state theory
DFT	Density functional theory
DHF	Dihydrofolate
DHFR	Dihydrofolate reductase
DME	Dimethoxyethane
DNOA	Donor-amidinium-carboxylate-acceptor
DONA	Donor-carboxylate-amidinium-acceptor
ET	Electron transfer
HAT	Hydrogen atom transfer
HF	Hartree-Fock
IR	Infrared
IRC	Internal reaction coordinate
KIE	Kinetic isotope effect

KS	Kohn-Sham
KS-DFT	Kohn-Sham density functional theory
KSE	Kinetic solvent effect
LC	Long-range correction
LCT	Large-curvature tunneling
MCSCF	Multiconfigurational self-consistent field
ME	Multiexciton
MEP	Minimum energy path
MLCT	Metal-to-ligand charge transfer
MO	Molecular orbital
μOMT	Microcanonical optimized multidimensional tunneling
MSDFT	Multistate density functional theory
NADPH	Nicotinamide adenine dinucleotide phosphate
PCET	Proton-coupled electron transfer
PCM	Polarizable contiuum model
PES	Potential energy surface
PT	Proton transfer
QM/MM	Quantum mechanical/molecular mechanical
RDC	Rule of diabatic crossing
RNR	Ribonucleotide Reductase
SCT	Small-curvature tunneling
SOMO	Singly-occupied molecular orbital

SPLET	Sequential proton-loss electron transfer
SVB	Simple valence bond
TEMPO	2,2,6,6-tetramethyl-piperidin-1-oxyl
THF	Tetrahydrofolate
TS	Transition state
TST	Transition state theory
VB	Valence bond
VBCMD	Valence bond configuration mixing diagram
VBSCD	Valence bond state correlation diagram
VBSCF	Valence bond self-consistent field
VDC	Variational diabatic configuration

Chapter 1. Introduction

1.1 Motivation

Nature has fine-tuned the mechanism of proton-coupled electron transfer (PCET) to facilitate essential biological processes, including water oxidation in photosystem II,[1] radical transport to initiate the catalysis of nucleotide reduction in ribonucleotide reductase,[2] and abstraction of a reducing equivalent from ascorbic acid in cytochrome oxidase b531.[3] In each of these examples, Nature utilizes PCET to facilitate reduction-oxidation (redox) chemistry[4–8] and we would like to understand the factors used to control these processes. Experimentally, PCET mechanisms are distinguishable as stepwise or concerted mechanisms, where sequential electron transfer (ET)/proton transfer (PT), or, alternatively, PT/ET mechanisms are identified by the presence of an observable intermediate species and two distinct mechanistic steps.[9–11] On the other hand, concerted PCET mechanisms couple ET and PT in one mechanistic step with no observable intermediate species. Recent theoretical work has identified a range of mechanisms within the concerted regime based on the degree of coupling between ET and PT, known as the electronic adiabaticity of the reaction.[12–14] Although concerted mechanisms are difficult to discern experimentally,[9,10] the basic understanding of the factors that dictate not only whether a PCET process is stepwise or concerted, but also where a concerted PCET process lies along the electronic adiabaticity continuum is essential to understanding how Nature controls redox processes in biological systems.

A remarkable example of a series mechanistically diverse PCET processes can be found within a single enzyme, ribonucleotide reductase (RNR).[2,5,6] Responsible for the

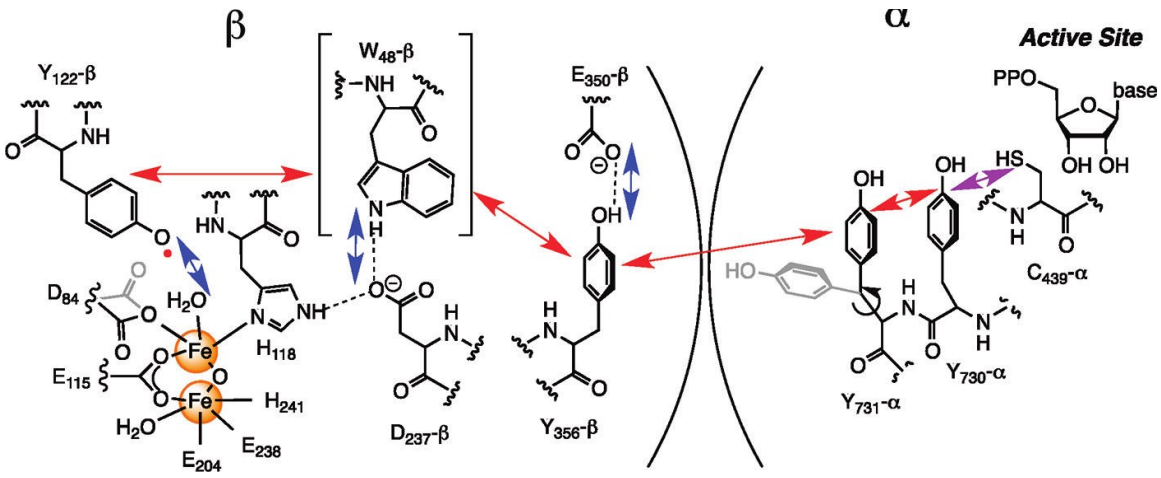

Figure 1.1 Proposed PCET pathway in *E. coli* class Ia RNR. Red/blue arrows indicate orthogonal ET/PT coordinates and the purple arrow indicates a collinear reaction coordinate. Reprinted with permission from Yokoyama, K.; Smith, A. A.; Corzilius, B.; Griffin, R. G.; Stubbe, J. *J. Am. Chem. Soc.* **122**, 18420 (2011).

sole production of deoxyribonucleotides and maintenance of nucleotide pools, RNR is essential to the synthesis of DNA and the pathways through which cells monitor and repair damaged DNA.[15,16] There are several classes of RNR enzymes, but one of particular interest is class Ia RNRs. These enzymes consist of two subunits that must form a complex for nucleotide reduction to occur.[17,18] The active site of nucleotide reduction is located within one subunit (α2), while a diiron-tyrosyl radical cofactor (Y122•) is located over 35 Å away in the second subunit (β2). Long-range, reversible radical transport between Y122• and C439 has been demonstrated in class Ia *E. coli* RNR.[2,19] Given the observed catalytic rate and the relatively long distance for direct electron transfer between these residues, a hopping mechanism was proposed along a set of conserved residues spatially connecting Y122• and C439. Systematic studies, most notably by Stubbe and co-workers,[2] have investigated the mechanism of radical transport

along this pathway, ultimately leading to the proposed series of PCET reactions shown in Figure 1.1. It has been shown that PCET occurs in an orthogonal fashion within subunit β2, while residues in subunit α2 are more spatially compact and have demonstrated a dependence on a strong hydrogen bonding network, indicating collinear PCET within subunit α2.

Given the diverse set of PCET mechanisms implicated in the proposed catalytic mechanism of nucleotide reduction in class Ia *E. coli* RNR,[2] it is of interest to elucidate the electronic, structural, and kinetic properties that govern PCET reaction in small molecule systems. For example, the hydrogen abstraction of phenol molecules, formally a hydrogen atom transfer (HAT) process, has been shown to display unusual variations in rate and equilibrium constants with respect to the polarity and hydrogen-bonding nature of the solvent.[9] These reactions are thought to occur within the same bond, similar to collinear PCET in RNR subunit α2. However, concerted PCET has been shown to occur in systems that differ in the relative ET and PT donor-acceptor distance.[10,20] In addition, electrostatic effects are thought to have a significant impact on the observed rates of reaction and driving force.[20] Lastly, these local environmental changes are compounded by conformational fluctuations in protein environments.[21–23] To investigate these effects on PCET mechanisms, a series of studies on small molecule systems have been carried out using a computationally efficient density function method capable of treating the multireference nature of PCET reactions.

1.2 Summary of Chapters

First, a survey of terminology, definitions, and classifications of PCET mechanisms[10,11] is provided in Chapter 2. In addition, the current theoretical approaches to modeling PCET reactions and the relevant experimental observables are presented.[9,24–28] In Chapter 3, the multistate density functional theory (MSDFT) method[29,30] developed in our group is presented with an emphasis on its application to PCET mechanisms.

Chapter 4 and 5 provide validation studies of the MSDFT method as a quantitatively and qualitatively accurate approach to modeling PCET reactions. Specifically, Chapter 4 presents published work on the MSDFT analysis of the self-exchange reactions of the isoelectronic series $Ph_2X_2H^{\bullet}$ (X = O, NH, CH_2).[31] In agreement with previous computational studies using higher levels of theory, a simple diagnostic test based on MSDFT results is shown to accurately characterize the benzyl/toluene radical and the phenol/phenoxyl radical self-exchange reactions in terms of electronic adiabaticity. In addition, this work presents the formulation of a three-dimensional More O'Ferrall-Jencks diagram useful for discerning the underlying characteristics of PCET mechanisms. Alessandro Cembran, Changwei Wang, Wei Wu, and Jiali Gao are acknowledged as co-authors of Chapter 4.

Chapter 5 extends the validation of the MSDFT method to a model complex developed by Daniel G. Nocera in which the electron and proton are localized on spatially difference donor-acceptor sites.[20] Application of MSDFT to this complex demonstrates the inherent coupling of ET and PT present in the system despite the difference in ET and PT distances. In addition, the electrostatic effects on the rate and

driving force are discussed and compared to previous theoretical studies.[32,33] Jiali Gao is acknowledged as a co-author of Chapter 5.

Chapters 6 and 7 investigate the mechanism of hydrogen atom abstraction of ascorbic acid by a nitroxyl radical. This reaction displays unusual kinetic solvent effects (KSE) and kinetic isotope effects (KIE) compared to hydrogen atom abstractions of phenol type substrates.[9,34,35] In Chapter 6, the MSDFT approach outlined in Chapters 3-5 is used to elucidate the underlying mechanistic nature of the ascorbate/TEMPO radical reaction and provide an interpretation of the MSDFT results with respect to the physical properties of the system. Jiali Gao is acknowledged as a co-author of Chapter 6.

One key experimental observable used to study PCET reactions is the KIE and its solvent and temperature dependence. Experimental values indicate significant tunneling in the rate-limiting step of the reaction, consistent with an electronically non-adiabatic process.[34,35] In Chapter 7, we employ two rate theories[24,36] to compute the KIE and compare to experiment. In addition, we investigate the origin of the solvent and temperature dependence of the experimental KIE. Jiali Gao is acknowledged as a co-author of Chapter 7.

The role of environmental effects on PCET mechanisms are directly incorporated in MSDFT through a combined quantum mechanical/molecular mechanical (QM/MM) approach.[37,38] Chapter 8 presents a collaborative project published in *Accounts of Chemical Research* investigating the mechanism of singlet fission in pentacene and tetracene monolayers.[39] Specifically, MSDFT is used to compute the electronic coupling between various excited electronic states involved in the process of singlet fission in

which the explicit polarization of the excited state electron density is included through the QM/MM MSDFT Hamiltonian. These coupling constants are then employed in density matrix simulations to elucidate the quantum coherent mechanism of singlet fission. Wai-Lun Chan, Timothy C. Berkelbach, Nicholas R. Monahan, David R. Reichman, John R. Tritsch, Mark S. Hyberten, Jiali Gao, and X.-Y. Zhu are acknowledged as coauthors of this chapter.

Expanding the application of MSDFT QM/MM to molecular dynamics, Chapter 9 illustrates the use of MSDFT to compute free energy surfaces of a simple electron transfer between solvated iron ions. Specifically, the reactant and product diabatic states are studied using free energy perturbation methods.[37] Jiali Gao is acknowledged as a co-author of Chapter 9.

Chapter 10 investigates the electrostatic and dynamical effects of protein fluctuations on the mechanism of hydride transfer catalyzed by dihydrofolate reductase (DHFR).[40,41] This study is an ongoing investigation of DHFR catalysis and builds on previous studies from our group that probed the dynamical flexibility of a loop structure near the active site of hydride transfer.[42,43] We employ a computational technique in which the QM dipole moment operators are used to obtain the infrared spectrum of carbon-deuterium bond frequencies in the otherwise silent spectral region.[44,45] Results are compared with experimental IR spectra of wild-type DHFR[41] and the role of local electrostatic, hydrogen bonding, and structural effects on the IR spectra are discussed. Alessandro Cembran and Jiali Gao are acknowledged as co-authors of this chapter.

Chapter 2. Background

2.1 Definitions and Terminology

In general, any mechanism that involves electron and proton transfer may be considered a proton-coupled electron transfer (PCET) and characterized by four charge-localized diabatic states.[11,46,47] Figure 2.1 illustrates a two-dimensional More O'Ferrall-Jencks diagram dipicting four diabatic states represented by valence bond structures in each corner of the diagram. Here, 0 and 1 indicate the localization of the electron on its donor and acceptor sites and *a* and *b* indicate localization of the proton on its respective donor and acceptor sites. As described by Ingold, the key distinction between concerted and stepwise mechanisms is the presence of an intermediate species, indicating two separate mechanistic steps.[9] Stepwise electron transfer/proton transfer (ET/PT) and, alternatively, stepwise proton transfer/electron transfer (PT/ET) are depicted in Figure 2.1 along the edges of the diagram, where the sequential proton-loss electron transfer (SPLET) mechanism defined by Ingold is synonymous with stepwise PT/ET.

Alternatively, PCET reactions may proceed in a concerted fashion where electron and proton transfer occur within a single mechanistic step. In Figure 2.1, concerted PCET is indicated by the diagonal arrow from state 0*a* to 1*b*. However, this diagram can be misleading as there is actually a continuum of concerted PCET mechanisms ranging from concerted proton-electron transfer (CPET) to hydrogen atom transfer (HAT).[12–14] It is important to note, PCET is used here as an umbrella term to classify any process involving electron and proton transfer, including both stepwise and concerted mechanisms. Historically, any concerted mechanism in which electron and proton

transfer occur within a single kinetic step has been identified as HAT, especially within the organic chemistry community. Only recently has there been made a distinction within concerted PCET mechanisms and there remain discrepancies in the literature as to the definition of the terms used to describe such mechanisms. Here, CPET and HAT are used to distinguish between the extremes of the continuum of concerted PCET mechanisms.

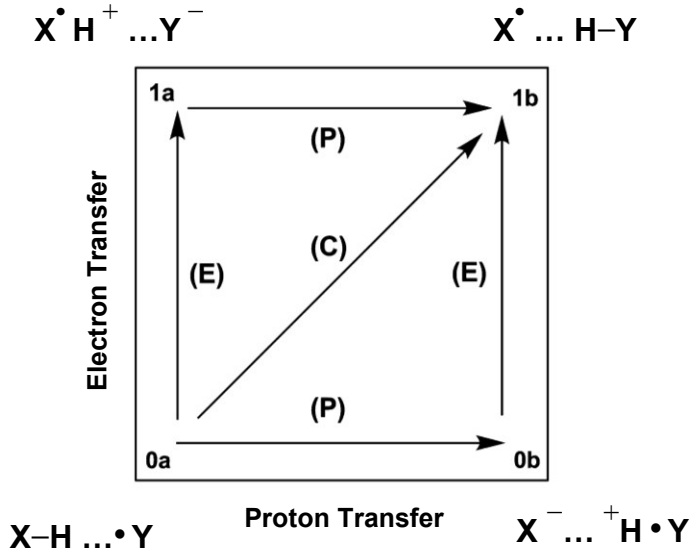

Figure 2.1 Two-dimensional More O'Ferrall-Jencks diagram depicting stepwise and concerted PCET mechanisms. Valence bond structures in each corner represent diabatic states of a formal HAT reaction, where the transferring electron and proton originate from and transfer to the same donor-acceptor pair.

2.2 Current Understanding from Theory and Experiment

As shown by Mayer,[48] concerted PCET mechanisms are often more thermodynamically favorable due to the avoidance of high-energy, charge-separated intermediates incurred by stepwise ET/PT and PT/ET. However, Ingold has demonstrated that in certain solvents, stepwise PT/ET kinetically competes with concerted PCET in hydrogen atom abstraction reactions of phenols by free radicals, as indicated by an

increased reaction rate than predicted by the hydrogen bond accepting ability of the solvent and the hydrogen bond donating ability of the phenol.[9,49] These kinetic solvent effects (KSE) are accounted for by an additive rate constant of both the formal HAT mechanism and the stepwise SPLET mechanism. The degree to which the stepwise SPLET mechanism contributes to the overall hydrogen atom abstraction is explained in terms of the ionization potential of the phenol, solvent effects on the ionization potential of the phenol, and the electron affinity of the free radical.[9] In the end, Ingold acknowledges a mechanistic distinction within the regime of concerted PCET (i.e. HAT and CPET), but reiterates that these mechanisms are difficult, if not impossible, to distinguish experimentally and argues that unusual KSE of formal HAT reactions are in fact due to the kinetically competitive side-reaction of SPLET contributing to the overall rate constant.

On the other hand, Mayer et al. has distinguished the concerted mechanisms CPET and HAT, although CPET is often referred to as PCET in his papers, in terms of the relative orientation of the singly occupied molecular orbital (SOMO) with respect to the proton transfer coordinate (Figure 2.2).[12] Demonstrated by the self-exchange reactions of toluene/benzyl radical and phenol/phenoxyl radical, unrestricted density functional theory calculations reveal that these concerted PCET reactions, formally HAT, involve unique electronic configurations at the optimized transition state structure. Specifically, the SOMO of the phenol/phenoxyl radical hydrogen-bonded complex consists of two *p*-type orbitals on the oxygen atoms, oriented orthogonal to the linear proton transfer coordinate. In contrast, the SOMO of the toluene/benzyl radical complex

consists of two *p*-type molecular orbitals directed along the proton transfer coordinate. Mayer et al. concludes the toluene/benzyl radical reaction involves the direct transfer of hydrogen and one of its bonding electrons from the C-H σ-bond of toluene to the *p*-like SOMO of the benzyl radical, constituting a three-electron, three-center electronic configuration (C•H•C) at the transition state structure.[12] Alternatively, the CPET mechanism consists of a proton transfer from the O-H σ-bond of phenol to a lone-pair on the phenoxyl radical and an electron from a lone-pair on the phenol to the SOMO of the phenoxyl radical.

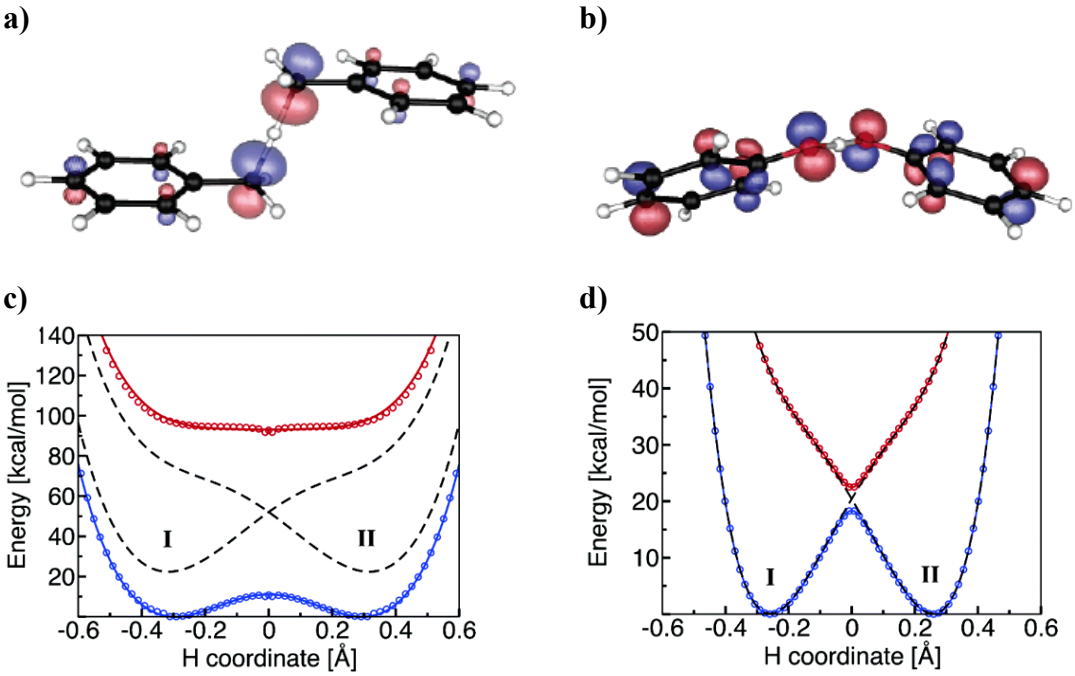

Figure 2.2 Singly-occupied molecular orbital at the optimized transition state geometry of the a) benzyl/toluene and b) phenoxyl/phenol self-exchange reactions at the unrestricted B3LYP/6-31G* level of theory. Adiabatic (open circles) and diabatic (dashed lines) potential energy curves of c) benzyl/toluene and d) phenoxyl/phenol self-exchange reactions calculated using state-averaged CASSCF. Reprinted with permission from Skone, J. H.; Soudackov, A. V.; & Hammes-Schiffer, S. *J. Am. Chem. Soc.* **128**, 16655-16663 (2006). Copyright 2006 American Chemical Society

Mayer emphasizes that the phenol/phenoxyl radical complex is able to form a hydrogen bond, thereby mediating a proton transfer between two doubly occupied molecular orbitals.[12] However, Mayer cautions that this alone is not a discerning characteristic of CPET mechanisms. The self-exchange reaction of methanol/methoxyl radical was shown to involve a three-electron, three-center bond similar to the HAT mechanism of toluene/benzyl radical complex, even though methanol/methoxyl forms a hydrogen-bonded complex. Based on analysis of unpaired spin density and atomic charges, Mayer argues that ability of the phenyl ring to delocalize unpaired spin stabilizes the transition state structure of the phenol/phenoxyl complex compared to that of methanol/methoxyl. Thus, phenol/phenoxyl prefers the CPET mechanism over HAT, while methanol/methoxyl proceeds via the lower energy HAT intermediate. It is noted that the work of Mayer et al. corroborates the KSE described by Ingold for hydrogen atom abstraction of phenols by free radicals in that hydrogen-bonds formed between the phenol and a solvent molecule inhibits the formation of the hydrogen-bonded complex of phenol and the free radical species responsible for abstracting a hydrogen atom from phenol. Furthermore, the description set forth by Mayer provides a chemically intuitive picture of CPET and HAT mechanisms based on molecular orbital theory.

A more rigorous distinction between CPET and HAT is based on the degree of electronic adiabadicity.[13,14] As shown in Figure 2.2, the HAT reaction of toluene/benzyl radical is characterized by a large energy gap between the ground and excited state potential energy surfaces (PES) at the transition state geometry, indicative of an electronically adiabatic process; whereas the CPET reaction of phenol/phenoxyl radical

has a very small energy gap at the transition state geometry, i.e. an avoided crossing of the ground and excited state PES. This avoided crossing indicates a conical intersection may lie nearby and the reaction may proceed via non-adiabatic coupling, i.e. thermal activation of the excited state, at the transition state geometry. Thus, the CPET reaction of phenol/phenoxyl is characterized as an electronically non-adiabatic process.

Hammes-Schiffer emphasizes that both CPET and HAT mechanisms are electronically non-adiabatic with respect to solvent.[11] That is, due to the quantum mechanical nature of electron and proton tunneling, both electron and proton transfer are instantaneous with respect to fluctuations within the solvent. Thus, the discerning factor between CPET and HAT mechanisms is the *electronic adiabaticity of proton transfer*. That is, the degree to which electron transfer is coupled to proton transfer. If they are strongly coupled, the electron remains in equilibrium with the proton throughout the reaction coordinate and is characterized by an electronically adiabatic potential energy surface (PES); whereas, the CPET mechanism involves very little coupling between electron and proton transfers, characteristic of an electronically non-adiabatic proton transfer, which is manifested in the PES as a small energy gap between the adiabatic ground and excited states near the transition state.

In summary, the overall process of transferring an electron and proton are classified as a stepwise ET/PT or PT/ET or a concerted mechanism. Within the concerted regime, mechanisms are classified as electronically non-adiabatic CPET, electronically adiabatic HAT, or an intermediate between these two extremes.

2.3 Theoretical Models of Proton-Coupled Electron Transfer

2.3.1 The Doubly Adiabatic Approach and Two-Dimensional Approach

Cukier developed two approaches for modeling PCET reactions. Traditional Marcus theory describing electron transfer is the basis for both methodologies; however, different assumptions are made to accommodate the tunneling proton in each method. The doubly adiabatic approach makes two Born-Oppenheimer (BO) approximations in order to simplify the multidimensional PCET reaction to a one-dimensional model.[32] The first BO approximation is that the transferring electron is much faster than atomic nuclei. As a result, the electronic effects of the transferring electron are reduced to simple coupling terms within the Hamiltonian and the proton PES becomes dependent on the electronic state, initial (*i*) or final (*f*). A double-well potential is employed by Cukier to model these electron-dependent PES (Figure 2.3). The second approximation asserts that the transferring proton is sufficiently faster than all other atomic nuclei, thereby creating four wavefunctions that are dependent on the initial and final states of the electron (*i* and *f*) and the proton (*a* and *b*). The resulting one-dimensional potential energy functions are plotted against a generalized solvent coordinate (R) in Figure 2.4. Comparing the

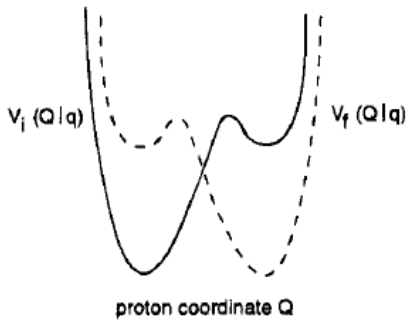

Figure 2.3 Double-well potentials of proton PESs, when the electron is in its initial $V_i(Q|q)$ and final $V_f(Q|q)$ states and the solvent is in a specific configuration q. Reprinted with permission from Cukier, R. I. *J. Phys. Chem.* **99**, 16101 (1995). Copyright 1995 American Chemical Society

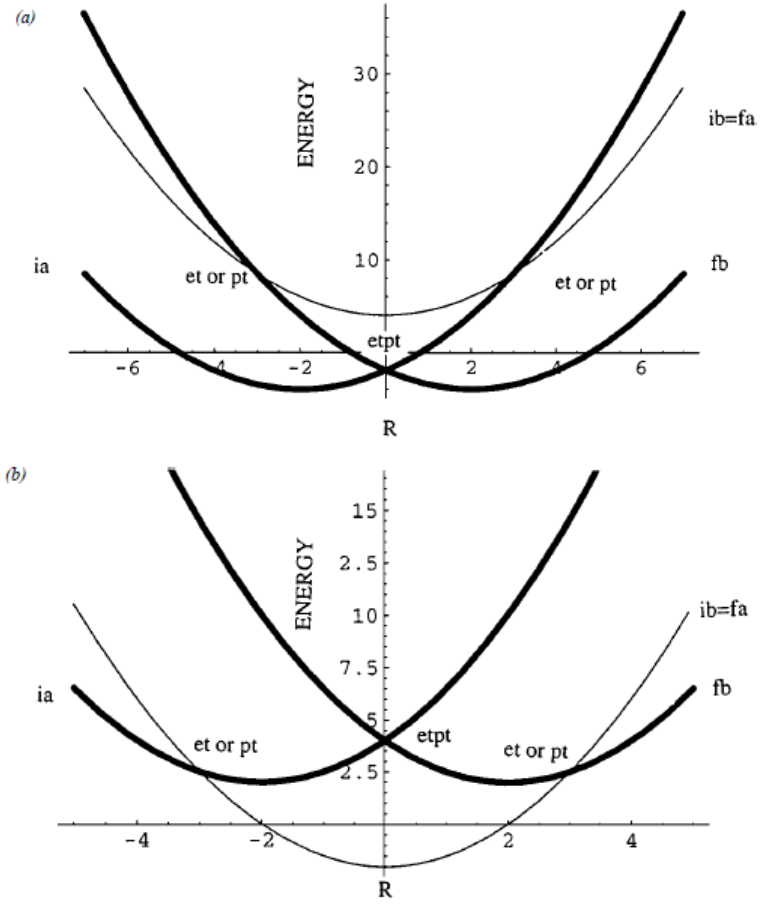

Figure 2.4 Diabatic PESs with the electron (*i*, *f*) and proton (*a*, *b*) in their respective initial and final states: a) PCET preferred b) ET preferred. Note that the *ib* and *fa* states are degenerate in this example and the reaction coordinate (R) is a generalized solvent coordinate. Reprinted with permission from Cukier, R. I. & Nocera, D. G. *Annu. Rev. Phys. Chem.* **49**, 337 (1998). Copyright 1998 Annual Reviews

activation energy, as defined by Marcus theory, for a reaction in which both the electron and proton transfer (*ia*→*fb*) to that of just ET (*ia*→*fa*), this method clearly distinguishes between stepwise and concerted PCET mechanisms. However, the transferring electron is approximated to a different extent than the transferring proton, hence the quantum mechanical nature of the two entities are not necessarily equivalent.

To ensure equal treatment of the electron and proton, Cukier presents the two-dimensional approach in which the one-dimensional Marcus theory is extended to two-dimensions.[32] A two-dimensional tunneling space is constructed based on the reaction coordinates of the electron and the proton (Figure 2.5). Concerted PCET can be visualized as occurring diagonally across the two-dimensional tunneling space (*ia*→*fb*). For concerted reactions, solvent fluctuations alter the PES such that the initial and final states of both ET and PT are degenerate. In this solvent configuration, the electron and proton tunnel in one quantum event. Stepwise PCET is characterized by a PES that favors ET, which then alters the PES to make PT thermodynamically favorable. Here, the electron and proton tunnel in two separate quantum events. However, for a given solvent configuration several proton vibrational states may be energetically accessible for one localized electronic state. To remove this complication, the electron is assumed to be sufficiently faster than the proton (i.e. BO approximation). As a result, the tunneling pathway within the two-dimensional space is restricted to a "zigzag" path. Figure 2.5 diagrams this path in which the proton displaces to a coordinate where the two-dimensional PES is degenerate for the localized electronic initial and final states. At this point, the ET occurs and then the proton finishes its transfer to the final configuration.

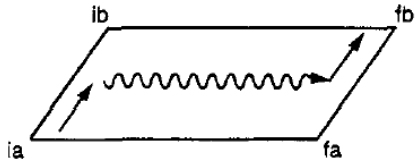

Figure 2.5 "Zigzag" pathway within Cukier's two-dimensional approach: *i*, *f* and *a*, *b* indicate the electron and proton initial and final states, respectively. Reprinted with permission from Cukier, R. I. & Nocera, D. G. *Annu. Rev. Phys. Chem.* **49**, 337 (1998). Copyright 1998 Annual Reviews

The beauty of Cukier's development is both approaches derive an equivalent rate constant expression and a simplified PCET coupling (V_{PCET}) expression.[26] Similar to electronic coupling (V_{el}), which describes the overlap between electronic wavefuctions with the electron in its initial and final state, V_{PCET} represents the overlap between the electron-proton wavefunctions with the electron and proton in their respective initial and final states.[32] Use of the Born-Oppenheimer approximation on the electron with respect to the proton allows for the PCET coupling matrix element to be approximated as $V_{PCET} \approx V_{el}\left|\left\langle \chi_{fn} \middle| \chi_{in'} \right\rangle\right|$. The Franck-Condon term $\left|\left\langle \chi_{fn} \middle| \chi_{in'} \right\rangle\right|$ is the overlap of the protonic wavefunctions corresponding to the system in the initial (*in'*) and final (*fn*) proton vibrational states (which are dependent on the electronic state *i* and *f*).[26] It is important to note that V_{el} is assumed to equal half the splitting between the symmetric and antisymmetric eigenfunctions of the system, which is true only when the overlap integral is restricted to orthonormality. Using this approximate V_{PCET}, Cukier used the Marcus-Levich[50,51] charge-transfer rate constant expression to derive a PCET rate constant valid in the electronically non-adiabatic limit for both ET and PT

$$k_{PCET} = \frac{V_{el}^2}{\hbar^2}\sqrt{\pi\hbar^2 / \lambda_s^{PCET} k_B T}\sum_{n'} \rho_{in'} \sum_{n\in b}\left|\left\langle \chi_{fn} \middle| \chi_{in'} \right\rangle\right|^2 e^{-(\lambda_s + \Delta G^\circ)^2 / 4\lambda_s k_B T} \qquad (1)$$

where $\lambda_s^{\mathrm{PCET}}$ indicates the solvent reorganization energy due to both ET and PT and $\rho_{in'}$ indicates the equilibrium proton distribution of the initial electronic state. It is summed over all bound vibrational states within the reactant well of $V_i(Q|q)$ (*n'*). The driving force is defined as $\Delta G^\circ = \Delta E^{el} + \varepsilon_{fn} - \varepsilon_{in'}$, where ΔE^{el} is the electronic structure

contribution and $\varepsilon_{fn} - \varepsilon_{in'}$ is the proton vibrational level contribution to the free energy difference between the reactant and product states.

Inspection of the PCET rate constant expression shows that the Franck-Condon overlap $\left|\left\langle \chi_{fn} \middle| \chi_{in'} \right\rangle\right|$ is summed over the vibrational states in only the product well of the proton PES. By altering this summation to include only those in the reactant well, the rate for ET may be calculated using different values for the solvent reorganization energy (λ_s^{ET}) and driving force (ΔG°). In order to accommodate the HAT mechanism, Cukier extended the derivation of PCET rate constants to the adiabatic limit of PT, while maintaining the non-adiabatic nature of ET.[47]

The terms needed for evaluating these rate constant expressions depend on an ellipsoidal dielectric continuum model. Within this model the electrostatics of the system are represented as four point charges, one for each donor and acceptor, located within an ellipsoidal cavity that is embedded in dielectric continuum.[26,32] Electronic coupling terms, vibronic coupling terms between electron-dependent protonic states, solvent reorganization energies, and the change in free energy of the system depend on the solvated PES. This solvated electron-proton PES is constructed based on a gas-phase PES, as determined from electronic structure calculations, with the addition of solvation terms calculated from the dielectric continuum ellipsoidal model.

2.3.2 Multistate Continuum Theory

Based on the work of Cukier, Hammes-Schiffer derived rate constant expressions for various limits of electronic adiabaticity.[10,11,25,26,52,53] In the regime of electronically non-adiabatic ET, the rate constant is given as

$$k = \frac{1}{\hbar}\sum_{\mu}^{\{I\}} P_{\mu}^{I} \sum_{\nu}^{\{II\}} \left|V_{\mu\nu}\right|^2 \sqrt{\frac{\pi}{\lambda_{\mu\nu} k_B T}} \exp\left(\frac{-(\Delta G^{\circ}_{\mu\nu} + \lambda_{\mu\nu})^2}{4\lambda_{\mu\nu} k_B T}\right) \tag{2}$$

where *I* and *II* indicate ET reactant and product states, and μ and v represent vibrational wavefunctions localized within electronic states *I* and *II*, respectively. As depicted in Figure 2.6, this theoretical approach is an extension of one-dimensional Marcus theory to two dimensions. The electron-localized diabatic states denoted as I and II are best represented by paraboloids within the two-dimensional tunneling space. PT is characterized by the overlap of vibration wavefunctions localized within each paraboloid. Thus, the vibronic coupling ($V_{\mu v}$) of the overall PCET process is approximated as

$$V_{\mu\nu} \approx V_{el} \left|\left\langle \varphi_{\mu}^{I} \middle| \varphi_{\nu}^{II} \right\rangle\right| \tag{3}$$

where V_{el} is analogous to Marcus theory electronic coupling and $\left\langle \varphi_{\mu}^{I} \middle| \varphi_{\nu}^{II} \right\rangle$ is the Franck-Condon overlap of proton vibrational wavefunctions φ_{μ}^{I} and φ_{ν}^{II}. Additionally, the rate constant depends on the thermodynamic terms, $\Delta G^{\circ}_{\mu v}$ and $\lambda_{\mu v}$, which are the driving force and reorganization energy, respectively. These terms are analogous to ΔG° and λ in Marcus theory, except they depend on population of vibrational states μ and v within electronic states *I* and *II*, respectively. Lastly, P_{μ}^{I} is the Boltzmann factor for electron transfer originating from vibrational state μ within electronic state *I*. It is important to note, the PCET rate constant expression derived by Hammes-Schiffer is equivalent to the expression derived by Cukier.

Hammes-Schiffer has applied the multistate continuum theory to a series of model systems and biologically relevant PCET reactions.[13,33,54–59] Typically, the input quantities

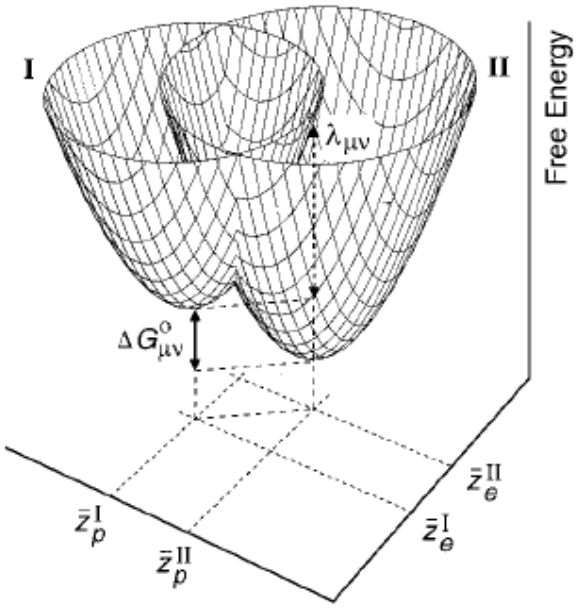

Figure 2.6 Schematic illustration of a pair of paraboloids representing the electron-proton initial (Iμ) and final (IIν) states as functions of the proton solvent coordinate (z_p) and electron solvent coordinate (z_e). The reorganization energy ($\lambda_{\mu\nu}$) and the equilibrium free energy difference ($\Delta G^{\circ}_{\mu\nu}$) are indicated. Reprinted with permission from Hammes-Schiffer, S. *Acc. Chem. Res.* **34**, 273 (2001). Copyright 2001 American Chemical Society

necessary to calculate the rate constant are determined from gas-phase electronic structure calculations, such as state-averaged complete active space self-consistent field (CASSCF), with the addition of solvation terms. These solvation terms are calculated using a dielectric continuum model, including point charges on the electron and proton donor and acceptor atoms and the transferring proton. The energies of the mixed electron/proton vibronic states are found by solving the secular equation **H'C** = **EC**, where **H'** is an effective Hamiltonian matrix with elements $H'_{i\mu,j\nu}$, **C** is a coefficient matrix and **E** is a diagonalized matrix containing energy eigenvalues. The effective Hamiltonian matrix elements ($H'_{i\mu,j\nu}$) are defined as

$$H'_{i\mu,j\nu} = \delta_{ij}\delta_{\mu\nu}\varepsilon_{\mu}^{(i)}(z_p, z_e) + (1-\delta_{ij})\left\langle \phi_{\mu}^{(i)} \middle| H_{ij} \middle| \phi_{\nu}^{(j)} \right\rangle_p \qquad (4)$$

where δ_{ij} and $\delta_{\mu\nu}$ are Kronecker delta functions and H_{ij} is an off-diagonal matrix element parameterized by solvent terms.

Notice that the secular equation employed is missing the overlap matrix (**S**). It is assumed to be a unity matrix; hence, the overlap integral between different vibronic states (i.e. $i\mu \neq j\nu$) is assumed to be zero. It has been shown for a generalized two-state model that the coupling between diabatic states 1 and 2 (V_{12}) is dependent on the overlap integral S_{12}.[30,60] Furthermore, the adiabatic ground state energy is dependent on the coupling term V_{12}. Applying this knowledge to the four-state model described by Hammes-Schiffer, the coupling of vibronic states is assumed to be zero when this value could potentially affect the adiabatic ground state energy. Furthermore, a closer look at the definition of the effective Hamiltonian matrix elements ($H_{i\mu,j\nu}$) shows that off-diagonal elements of the Hamiltonian matrix are approximated by the interaction of two vibronic states scaled by the parameterized term, H_{ij}. Using this definition, some electronic coupling is included due to each vibronic state being dependent on the electronic state. However, the ability to apply an ab initio method to represent localized electron-proton diabatic states may improve the accuracy of the PES by explicitly including electronic coupling. In light of these drawbacks of the multistate continuum theory put forth by Hammes-Schiffer, we propose an alternative method for calculating the electronic coupling, vibrational overlap, and thermodynamical quantities necessary to compute of the rate constant, namely, multistate density functional theory (MSDFT). The methodology of this approach is presented in Chapter 3 and its application and validation for the study of PCET mechanisms is the topic of the remaining chapters.

2.3.3 Phenomenological Rate Constant Expressions

Demonstrated by Ingold,[9] the rate of hydrogen atom abstraction of a phenol by a free radical is inhibited by the formation of a hydrogen bond between the phenol substrate and a hydrogen bond accepting solvent molecule (Figure 2.7). Based on empirical terms derived by Abraham et al.,[61] the rate constant of the formal hydrogen atom transfer (HAT) in a hydrogen bond forming solvent (k_{HAT}^{S}) is expressed as

$$\log(k_{HAT}^{S}) = \log(k_{HAT}^{0}) - 8.3\alpha_2^H \beta_2^H \quad (5)$$

where k_{HAT}^{0} is the HAT rate constant in a non-hydrogen bonding solvent and α_2^H and β_2^H are empirical parameters that quantify the ability of the solvent to accept and donate hydrogen bonds, respectively.[62]

Ingold[49,63] and, independently, Foti[64,65] demonstrate in certain solvents the hydrogen atom abstraction of a phenol by a free radical exhibits unusually large rate constants. These kinetic solvent effects (KSE) are explained by the involvement of a competing side-reaction named sequential proton-loss electron transfer (SPLET).[9] This mechanism is equivalent to stepwise PT/ET, as depicted in Figure 2.1, along the edges of

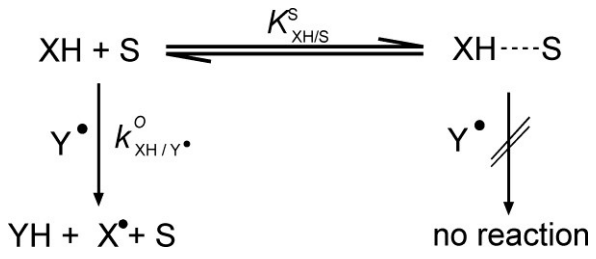

Figure 2.7 Mechanism for a "normal" HAT reaction in which hydrogen bond accepting ability of solvent molecule prohibits HAT due to substrate forming a hydrogen bond with solvent via the transferring hydrogen. Reprinted with permission from Litwinienko, G. & Ingold, K. U. *Acc. Chem. Res.* **40**, 222 (2007). Copyright 2007 American Chemical Society

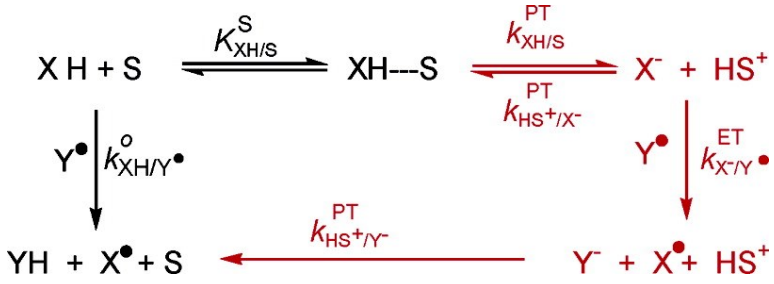

Figure 2.8 Competing SPLET mechanism accounts for unusual kinetic solvent effects of phenols in alcohol solvents. Reprinted with permission from Litwinienko, G. & Ingold, K. U. *Acc. Chem. Res.* **40**, 222 (2007). Copyright 2007 American Chemical Society

the More O'Ferrall-Jencks diagram proceeding from states *0a* → *0b* →*1b*. The overall mechanism includes contributions from both the concerted process, formally HAT, and stepwise SPLET (Figure 2.8). The total rate constant is additive where the HAT rate constant is determined by eq 5. Although no simple empirical equation is given for the SPLET rate constant, the physical properties that affect this term are discussed. Briefly, the extent to which the SPLET mechanism kinetically competes with the concerted HAT process is determined by the ionization of the phenol substrate, the solvent effects of the ionization of the phenol substrate, and the electron affinity of the free radical.[9]

Based on extensive experimental data of PCET reactions in various solvents,[46,48,66] Mayer has developed an approximate rate constant expression based on the Marcus cross relation[28,67]

$$k_{HAT} = \sqrt{k_{XH/X} k_{YH/Y} K_{HAT} f} \,. \tag{6}$$

Here, k_{HAT} is a rate constant for a generic hydrogen atom abstraction reaction, denoted as

$$X{-}H \;+\; Y \;\rightarrow\; X \;+\; H{-}Y \tag{7}$$

is determined by the cross relation of the individual self-exchange reaction rate constants of the donor (X) and acceptor (Y) molecules, the equilibrium constant (K_{HAT}) and a factor (f) based on the adiabatic collision frequency. The Marcus cross relation expression holds true for a large number of formal HAT reactions in a wide variety of solvents. As noted by Mayer,[28] the wide-spread applicability of the Marcus cross relation for reaction involving both ET and PT is surprising, especially given the known disparities in ET and PT tunneling time-scales and donor-acceptor distances. However, this phenomenological approach provides a conceptually simplified view of PCET theory, which may be both to its detriment and its success as a useful tool in prediction and interpretation of PCET rate constants.

Chapter 3. Multistate Density Functional Theory (MSDFT)

3.1 Introduction

Based on block-localized wavefunction theory,[68,69] molecular orbital-valence bond theory bridges delocalized molecular orbital (MO) theory and localized valence bond (VB) theory to give a computationally efficient method for modeling localized, i.e. diabatic, states.[29,37] Unlike diabatization schemes for electron transfer (ET)[70–76] and proton-coupled electron transfer (PCET),[77,78] this approach first defines diabatic states based on VB structures and through coupling, i.e. mixing, of diabatic states gives the resonance-stabilized adiabatic ground and excited states. Implemented at the density functional level of theory, this method is termed multistate density functional theory (MSDFT).[30,79] A key property of MSDFT is static electron correlation is treated through configuration interaction, while dynamic electron correlation is treated through the various exchange-correlation functionals employed in density functional theory (DFT).

3.2 Block-Localized Kohn-Sham (BLKS) Functions

In MSDFT, each diabatic state is defined as a single Slater determinant of block-localized Kohn-Sham (BLKS) orbitals expanded over only those basis functions assigned to a particular block. The electrons are also assigned to a particular block, which in this case are defined as the electron and proton donor and acceptor molecules.[30,79] MSDFT is a general methodology that may be applied to a variety of chemical reactions and is particularly suited for PCET reactions, because it provides an ab initio method to solving the Schrodinger equation for a given diabatic state.

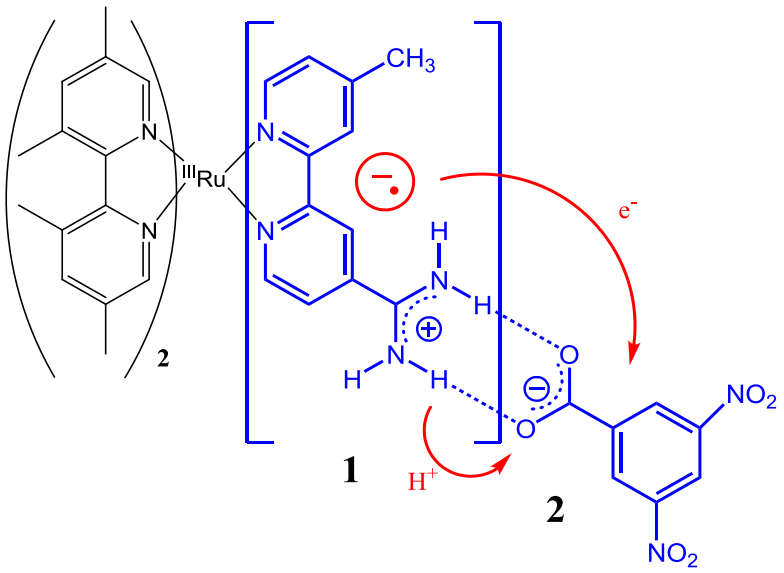

Figure 3.1. Following photo-chemically initiated metal to ligand charge transfer, PCET occurs from a Ru(II)-ligand donor to a dinitro-benzoate acceptor. The system is partitioned into two fragments (blocks), 1 and 2.

For illustrative purposes, consider the model complex shown in Figure 3.1 designed by Nocera and co-workers.[20] Following photo-excitation, the Ru(II)-ligand complex undergoes metal-to-ligand charge-transfer, localizing an excited electron on a bipyridine ligand. Great care was taken in the design of this model complex such that the excited electron is localized on a bipyridine ligand hydrogen bonded to a strong electron withdrawing group through a salt-bridge interface. In the following equations, the electron donor (D_e) is defined as the bipyridine ligand and amidinium group encased in brackets in Figure 3.1. The electron acceptor (A_e) is defined as the dinitrobenzoate molecule. The amidinium and carboxylate groups are denoted as $-NH^+$ and $-O^-$, respectively. Equations 1 – 4 define the MSDFT BLKS functions (Ψ^{BLKS}) for diabatic states 0*a*, 0*b*, 1*a*, and 1*b* with the corresponding VB structure of each state.

$$D_e^- - NH^+ \cdots O^- - A_e; \quad \Psi_{0a}^{BLKS} = \hat{A}\{\Omega_{0a}^1(D_e^- - NH^+)\Omega_{0a}^2(O^- - A_e)\} \tag{1}$$

$$D_e^- - N \cdots HO - A_e; \quad \Psi_{0b}^{BLKS} = \hat{A}\{\Omega_{0b}^1(D_e^- - N)\Omega_{0b}^2(HO - A_e)\} \tag{2}$$

$$D_e - NH \cdots O - A_e^-; \quad \Psi_{1a}^{BLKS} = \hat{A}\{\Omega_{1a}^1(D_e - NH)\Omega_{1a}^2(O - A_e^-)\} \tag{3}$$

$$D_e - N \cdots HO - A_e^-; \quad \Psi_{1b}^{BLKS} = \hat{A}\{\Omega_{1b}^1(D_e - N)\Omega_{1b}^2(HO - A_e^-)\} \tag{4}$$

For a given MSDFT diabatic state, occupied BLKS orbitals are expanded over only the basis functions allocated to a given block[29,30]

$$\varphi_{a,i}^K = \sum_{\mu=1}^{k} c_{i,\mu}\chi_{i,\mu} \tag{5}$$

where $c_{i,\mu}$ is a coefficient for basis function $\chi_{j,\mu}$, K indicates the diabatic state, i indicates the BLKS orbital, μ indicates the basis function, and k is the total number of basis functions allocated to block a. Each block (Ω_K^a) is represented as a Hartree product of occupied BLKS orbitals

$$\Omega_K^a = \varphi_{a,1}^K \alpha \varphi_{a,1}^K \beta \varphi_{a,2}^K \alpha \varphi_{a,2}^K \beta \cdots \varphi_{a,m}^K \beta \tag{6}$$

where α and β are electronic spin functions and m is the number of BLKS orbitals in block a. By taking the anti-symmerterized Hartree product of all blocks defined for diabatic state K, the BLKS function is defined as a single Slater determinant

$$\Psi_K^{BLKS} = N^K \hat{A}\left\{ \Omega_a^K \Omega_b^K \cdots \Omega_n^K \right\} \tag{7}$$

where N^K is the normalization constant, $\hat{A}$ is an antisymmetrizing operator, and n is the last block of diabatic state K.

A key feature of the BLKS formalism is the non-orthogonality of orbitals between different blocks such that each BLKS function retains the localized nature of VB theory, while orbitals within a block are orthogonal as in MO theory. As a result, the overlap (**S**) and coefficient (**C**) matrices in the generalized secular equation are given by

$$\mathbf{S} = \begin{pmatrix} S_{aa} & S_{ab} & \cdots & S_{an} \\ S_{ba} & S_{bb} & \cdots & \vdots \\ \vdots & \vdots & \ddots & \vdots \\ S_{na} & S_{nb} & \cdots & S_{nn} \end{pmatrix} \quad \text{and} \quad \mathbf{C} = \begin{pmatrix} C_a & 0 & \cdots & 0 \\ 0 & C_b & \cdots & 0 \\ \vdots & \vdots & \ddots & \vdots \\ 0 & 0 & \cdots & C_n \end{pmatrix} \tag{8}$$

where off-diagonal overlap matrix elements are non-zero and the coefficient matrix **C** is block-diagonal.[29,30]

By construction, this block-localized density functional theory (BLDFT)[30,80] is a strictly constrained density functional theory[81] in that the total electron density can be partitioned into the sum of fragment densities at the basis set level

$$\rho(\mathbf{r}) = \rho_a(\mathbf{r}) + \rho_b(\mathbf{r}) + ... + \rho_n(\mathbf{r}) . \tag{9}$$

Here, the integration of the fragmental density of block k ($k = a, b, \ldots, n$) satisfies the charge constraint $\int \rho_k(\mathbf{r})\,\mathrm{d}\,\mathbf{r} = n_k$, where n_k is the number of electrons allocated to block k. Although conceptually similar to the constrained DFT approach used by Van Voorhis and co-workers,[82] in which the electron density is constrained to a finite spatial region with the use of delocalized KS orbitals, BLKS orbitals are strictly localized due to orthogonality conditions regardless of spatial relationship, and thus provides a more generalized approach to constructing BLKS functions.[83–86]

3.3 Configuration Interaction of BLKS Functions

The resonance of VB states defined by eqs 1 – 4 yields the adiabatic ground and excited states. Thus, the MSDFT function is written as a linear combination of the four BLKS functions

$$\Phi^{MSDFT} = \sum_{K=1}^{4} c_K \Psi_K^{BLKS} \tag{10}$$

where c_K is the coefficient of state K.[29] In practice, MSDFT configuration interaction can be carried out using one of two methods: consistent diabatic configuration (CDC) or variational diabatic configuration (VDC). In CDC-MSDFT, the configuration coefficients (c_K) and the MO coefficients of the block-diagonal coefficient matrix **C** are simultaneously optimized to give the adiabatic ground state energy. In this sense, MSDFT is analogous to multiconfigurational self-consistent field (MCSCF). It has previously been shown that CDC-MSDFT accurately reproduces the adiabatic ground state energy at a lower computational cost than ab initio VB theory. Alternatively, the MO coefficients of each diabatic state can be variationally optimized and kept fixed in subsequent configuration interaction calculations. In this approach, VDC-MSDFT, the adiabatic ground state energy is necessarily equal to or higher than that of CDC-MSDFT, because the diabatic state MO coefficients are not optimized with respect to the adiabatic ground state energy. However, VDC-MSDFT has the key benefit of allowing for the construction of effective diabatic states that are useful for investigating the nature of charge-localized diabatic states.

As described by Hammes-Schiffer,[25] the four diabatic states in eqs 1 – 4 can be reduced to a two state model by taking an admixture of protonic states for a given electronic state

$$\Phi_R^{\boldsymbol{CPET}} = c_{0a}\Psi_{0a}^{\boldsymbol{BLKS}} + c_{0b}\Psi_{0b}^{\boldsymbol{BLKS}} \tag{11}$$

$$\Phi_P^{\boldsymbol{CPET}} = c_{1a}\Psi_{1a}^{\boldsymbol{BLKS}} + c_{1b}\Psi_{1b}^{\boldsymbol{BLKS}} \tag{12}$$

where R and P indicate the electron-localized reactant and product effective diabatic states. Here, we use concerted proton-electron transfer (CPET) to denote this two-state model because it characterizes an electronically non-adiabatic process. Alternatively, an electronically adiabatic process may be modeled by two proton-localized effective diabatic states,

$$\Phi_R^{\boldsymbol{HAT}} = c'_{0a}\Psi_{0a}^{\boldsymbol{BLKS}} + c'_{1a}\Psi_{1a}^{\boldsymbol{BLKS}} \tag{13}$$

$$\Phi_P^{\boldsymbol{HAT}} = c'_{0b}\Psi_{0b}^{\boldsymbol{BLKS}} + c'_{1b}\Psi_{1b}^{\boldsymbol{BLKS}} \tag{14}$$

where the configuration coefficients are different than those of the CPET states. This two-state model characterizes a hydrogen atom transfer (HAT) mechanism. It will be shown in Chapter 4 and 5 that these two-state models may be compared as a diagnostic test to classify a concerted PCET mechanism as either electronically non-adiabatic CPET or electronically adiabatic HAT.

In practice, MSDFT is used to first obtain PES of the four diabatic states (eqs 1 – 4) and, subsequently, the configuration coefficients are optimized for each set of effective diabatic states (eqs 11,12 and 13,14). Separately, the adiabatic states are determined by optimizing the configuration coefficients of all four diabatic states (eq 10). Thus, mixing

of CPET (or HAT) reactant and product states necessarily reproduces the adiabatic ground state as the lower root of the two-by-two secular equation

$$\begin{vmatrix} H_R^{CPET} - \varepsilon_g & H_{R,P}^{CPET} - \varepsilon_g S_{R,P}^{CPET} \\ H_{R,P}^{CPET} - \varepsilon_g S_{R,P}^{CPET} & H_P^{CPET} - \varepsilon_g \end{vmatrix} = \mathbf{0} \tag{15}$$

where the diagonal elements give the potential energy of the reactant and product effective diabatic states, i.e. expectation values, $H_R^{CPET} = \left\langle \Phi_R^{CPET} \middle| H \middle| \Phi_R^{CPET} \right\rangle$ and $H_P^{CPET} = \left\langle \Phi_P^{CPET} \middle| H \middle| \Phi_P^{CPET} \right\rangle$, with respect to the adiabatic ground state energy, ε_g. The off-diagonal matrix elements give the diabatic coupling element (V_{RP}) defined as

$$V_{R,P} = H_{R,P}^{CPET} - \varepsilon_g S_{R,P}^{CPET} \tag{16}$$

in terms of the exchange integral, $H_{R,P}^{CPET} = \left\langle \Phi_R^{CPET} \middle| H \middle| \Phi_P^{CPET} \right\rangle$, the overlap integral, $S_{R,P}^{CPET} = \left\langle \Phi_R^{CPET} \middle| \Phi_P^{CPET} \right\rangle$, and the adiabatic ground state energy, ε_g.

The MSDFT Hamiltonian matrix elements are defined as

$$\begin{aligned} H_{uw}^{\mathrm{MSDFT}} &\equiv E[\rho_{uw}(\mathbf{r})] \\ &= S_{uw}^{\mathrm{KS}} \{ Tr[(\mathbf{D}_{uw})^T \mathbf{h}] + \frac{1}{2} Tr[(\mathbf{D}_{uw})^T \mathbf{J} \mathbf{D}_{uw}] + E_{xc}[\rho_{uw}(\mathbf{r})] + E_{nuc} \} \end{aligned} \tag{17}$$

where **h** and **J** are the standard core and Coulomb integrals, S_{uw}^{KS} and $\mathbf{D}_{uw}$ are the KS overlap integral and density matrix for states *u* and *w*, E_{nuc} is the nuclear energy and $E_{xc}[\rho_{uw}(\mathbf{r})]$ is the exchange-correlation potential.[30] Note that eq 17 is valid both for the same state ($u = w$) and for exchange transition states ($u \neq w$) such that the coupling matrix elements (V_{RP}) can be directly computed using the MSDFT Hamiltonian $\left(H_{R,P}^{CPET} = H_{RP}^{MSDFT}\right)$ and the overlap of non-orthogonal KS functions $\left(S_{R,P}^{CPET} = S_{RP}^{KS}\right)$.

Chapter 4. Hydrogen Exchange Reactions in the Isoelectronic Series of $(PhX)_2H^{\bullet}$ (X = O, NH, CH_2)

4.1 Introduction

In this section, we use a multistate density functional theory (MSDFT)[30,79] to examine the hydrogen exchange reactions in the isoelectronic series of $(C_6H_5X)_2H$, where X = O, NH, and CH_2. We show that the hydrogen atom transfer (HAT) and concerted proton-electron transfer (CPET) reactivity is blended, and both pathways involve the same valence bond (VB) structures, albeit, to variable extents. Importantly, the difference between CPET and HAT mechanisms can be revealed in the third-dimension of a More O'Ferrall–Jencks diagram, which illustrates how the four-VB state mixing leads to almost a conical intersection (seam) in the PCET pathway of $PhO^{\bullet}$/PhOH compared to a very large energy separation between the ground and excited states in $PhCH_2^{\bullet}$/$PhCH_3$.

4.2 Previous Theoretical Studies of Hydrogen Transfer in Toluene/Benzyl Radical and Phenol/Phenoxyl Radical Self-Exchange Reactions

The reactions between phenol and the phenoxy radical and its isoelectronic analog, toluene and benzyl radical, have been studied computationally by a number of authors.[12–14,87–90] Mayer and coworkers first showed that the hydrogen exchange between phenol and phenoxyl radical follows a concerted CPET mechanism, whereas the hydrogen atom abstraction of toluene by benzyl radical is a HAT.[12] Mayer et al. examined the alignment of frontier molecular orbitals of the $PhO^{\bullet}\cdots HOPh$ complex and found that the orbital occupied by the unpaired electron is symmetrically orthogonal to

that of the donor-proton bond in the direction of proton migration. In this arrangement, there is a strong hydrogen bonding interaction, making the phenyl units essentially coplanar in the transition structure.[12] Consequently, five electrons are critically involved in the coupled proton and electron transfer, and the singly occupied molecular orbital (SOMO) is highly delocalized at the transition state. On the other hand, in the $PhCH_2^{\bullet}\cdots H_3CPh$ pair where hydrogen bonding is absent, the orbital occupied by the unpaired electron is nearly perpendicular to the two phenyl rings, but it coincides with that of the proton transfer coordinate at the transition state. In this case, a classical three-electron/three-center process is depicted, and the SOMO is localized in the C…H…C region.[12,90] This vivid orbital interaction picture is intuitive and has created a major impression in the interpretation of HAT and CPET reactions, but it is not clear on situations where there is significant mixing of orbitals in the transition states.[9,13,14,65,88–90] Subsequently, Hammes-Schiffer and coworkers,[13] who also used orbital symmetry to describe the two reactions, pointed out that the concerted proton and electron transfer in the phenol system is electronically non-adiabatic, whereas the reaction of benzyl radical and toluene takes place on the adiabatic potential energy surface. It was suggested that electronic adiabaticity can be used to differentiate CPET and HAT reactions.[13] Tishchenko et al. highlighted the involvement of both the ground and excited potential energy surfaces in CPET and emphasized competition between adiabatic barrier crossing and non-adiabatic transition through conical intersection.[14] These concepts probed the mechanistic features of CPET and HAT from different perspectives, although a common

theme in these studies is that they are based on calculations using delocalized wave functions with orthogonal orbitals.

Alternatively, the origin of the reaction barriers can be understood using valence bond (VB) theory, in which localized configurations are used.[30,91] One approach for rationalizing the origin of reaction barriers is the valence bond state correlation diagram (VBSCD) and valence bond configuration mixing diagrams (VBCMD) introduced by Shaik,[91–94] and it has been recently applied to a range of hydrogen atom transfer reactions.[95,96] In the latter work, the difference between HAT and CPET mechanisms was described in terms of the extent of HAT and charge transfer character in VB configuration mixing.

In this study, we also adopt a valence-bond-based approach to examine the origins of the CPET and HAT mechanisms in the hydrogen atom exchange reactions of $(PhX)_2H^{\bullet}$, where $X = O, NH,$ and CH_2. To begin our study, we use a block-localized density functional theory (BLDFT)[30,97] to define *non-orthogonal* PT and ET diabatic (localized) configurations *first*.[29,30,80,98] Then, these electronic configurational state functions (CSFs) are used in configuration interaction to yield the adiabatic (delocalized) ground and excited states.[30,79,97] In such a multistate DFT (MSDFT), the overlap between different diabatic states is explicitly determined using non-orthogonal CSFs. In contrast, our approach differs from diabatization procedures, in which the delocalized MCSCF or CASSCF wave functions undergo orthogonal transformation to extract diabatic states.[60] A critical assumption in such procedures is that the overlap integral between diabatic states is zero since there is no way to determine it in these approaches. However, the

overlap interactions contain key information in the understanding of the mechanistic difference between CPET and HAT.

In the following, we first summarize the method used to define diabatic states for the three hydrogen exchange reactions block-localization of Kohn–Sham orbitals. Then, we construct the characteristic state functions corresponding to the CPET and HAT reaction pathways. This is followed by results and discussion on the qualitative and quantitative features of the potential energy surfaces (PES) for the CPET and HAT mechanisms. This section is concluded with a summary of the main findings of this study.

4.3 Methodology

The mechanisms of the concerted and sequential ET and PT processes can be characterized by the four VB states illustrated in Figure 4.1.[10,25] If we use, respectively, 0 and 1 to indicate the localized electronic configurations, and *a* and *b* to denote the transferring proton localized on the donor (initial) and acceptor (final) sites (Figure 4.1), each diabatic state of the corresponding Lewis configuration can be represented by a single determinant of block-localized Kohn-Sham (BLKS) orbitals in density functional theory (DFT):[29,30,98]

$$\mathrm{Ph-XH\cdots{}^{\bullet}X-Ph}; \quad \Psi_{0a}^{\mathrm{BLKS}} = \hat{\mathrm{A}}\{\Omega_{0a}^{1}(\mathrm{Ph-XH})\Omega_{0a}^{2}({}^{\bullet}\mathrm{X-Ph})\} \tag{1}$$

$$\mathrm{Ph-X^{-}\cdots{}^{+\bullet}HX-Ph}; \quad \Psi_{0b}^{\mathrm{BLKS}} = \hat{\mathrm{A}}\{\Omega_{0b}^{1}(\mathrm{Ph-X^{-}})\Omega_{0b}^{2}({}^{+\bullet}\mathrm{HX-Ph})\} \tag{2}$$

$$\mathrm{Ph-XH^{+\bullet}\cdots{}^{-}X-Ph}; \quad \Psi_{1a}^{\mathrm{BLKS}} = \hat{\mathrm{A}}\{\Omega_{1a}^{1}(\mathrm{Ph-XH^{+\bullet}})\Omega_{1a}^{2}({}^{-}\mathrm{X-Ph})\} \tag{3}$$

$$\mathrm{Ph-X^{\bullet}\cdots HX-Ph}; \quad \Psi_{1b}^{\mathrm{BLKS}} = \hat{\mathrm{A}}\{\Omega_{1b}^{1}(\mathrm{Ph-X^{\bullet}})\Omega_{1b}^{2}(\mathrm{HX-Ph})\} \tag{4}$$

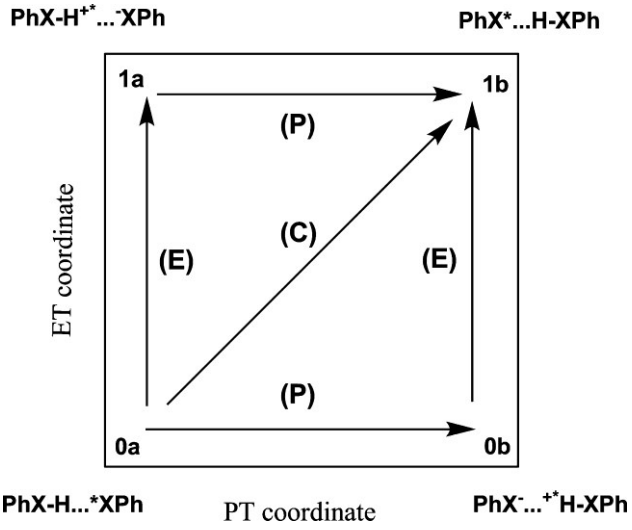

Figure 4.1 Two-dimensional More O'Ferrall-Jencks diagram depicting stepwise and concerted PCET mechanisms. Valence bond structures in each corner represent diabatic states of hydrogen self-exchange reactions in the isoelectronic series of $(C_6H_5X)_2H$, where X = O, NH, and CH_2.

In eqs 1 – 4, X = O, NH, or CH_2, Â is the antisymmetrizer, and Ω_γ^k denotes a product of the occupied BLKS orbitals for the *k*th (k = 1, 2) fragment specified in parentheses in diabatic state γ (γ = 0*a*, 0*b*, 1*a*, 1*b*). In BLDFT, the BLKS orbitals are orthogonal within each block as in standard DFT, which is computationally efficient, but orbitals between different blocks are non-orthogonal.[29,30,91,98]

The resonance (mixing) of the VB-like CSFs defined by eqs 1– 4 yields the adiabatic ground and excited states for the coupled ET and PT reaction, which are determined by configuration interaction in multistate density functional theory (MSDFT).[30,97] The VB-like wave function for the coupled proton and electron transfer reaction is written as a linear combination of the four CSFs:[29,30]

$$\Phi^{\mathrm{MSDFT}} = \sum_{\gamma=1}^{4} c_\gamma \Psi_\gamma^{\mathrm{BLKS}} \tag{5}$$

where c_γ is the coefficient for state γ. The BLKS determinants are used to yield constrained electron densities in DFT calculations to determine the energies of the diabatic states and the off-diagonal diabatic coupling elements, required for determining the rate constant.[29,30] Importantly, the function Φ^{MSDFT} itself is not used to generate the ground state density as in multiconfiguration density functional methods.[99–101] Instead, the ground and excited state energies are obtained as the lowest and higher roots of the corresponding generalized secular equation.[30] MSDFT has the advantage that both the electronically localized diabatic and the resonance delocalized adiabatic states can be determined to study energy transfer and PCET reactions.

It is useful to combine two of the diabatic configurations defined by eqs 1 – 4 (see Figure 4.1) to reduce the four-state theory into a pair of two-state models,[29,37,91,98] to describe, respectively, the CPET and HAT mechanisms.[10] In hydrogen atom transfer, by definition, the electronic configuration is adiabatic with respect to the hydrogen nuclear position (otherwise, it would involve separate ET, hence not a HAT).[10,47] Thus, the electronically localized VB configurations for a given proton (nucleus) configuration in eqs 1 – 4 must be combined to yield a lower energy state, i.e., the corresponding diabatic state for hydrogen atom transfer. Specifically, at a given localized proton position on the donor *a* (acceptor *b*) site, the effective diabatic state for the HAT reactant and product are generated from the resonance of the initial (0) and final (1) electronic configurations:

$$\Phi_R^{HAT} = c_{0a}\Psi_{0a}^{BLKS} + c_{1a}\Psi_{1a}^{BLKS} \quad (6)$$

$$\Phi_P^{HAT} = c_{0b}\Psi_{0b}^{BLKS} + c_{1b}\Psi_{1b}^{BLKS} \quad (7)$$

where c_γ are the configurational coefficients. The resonance of the HAT reactant (R) and product (P) VB diabatic states produces the adiabatic ground state potential surface for HAT, on which nuclear tunneling occurs (although the treatment of nuclear tunneling in the rate calculation is not the subject of the present study).[102–104]

In the CPET mechanism, electron transfer is separate from proton transfer by definition (otherwise, it would have been a HAT), and each PCET diabatic state (not necessarily concerted) is stabilized by the accompanying proton tunneling, thus, a proton-*coupled* electron transfer. Consequently, the effective diabatic configurations for the CPET process are combinations of the two proton configurations at a given electronic localization, in the reactant (0) and product (1) well, respectively:

$$\Phi_R^{\mathrm{CPET}} = c'_{0a}\Psi_{0a}^{\mathrm{BLKS}} + c'_{0b}\Psi_{0b}^{\mathrm{BLKS}} \tag{8}$$

$$\Phi_P^{\mathrm{CPET}} = c'_{1a}\Psi_{1a}^{\mathrm{BLKS}} + c'_{1b}\Psi_{1b}^{\mathrm{BLKS}} \tag{9}$$

where the prime over the mixing coefficients distinguishes them from those in eqs 6 and 7. Here, electron tunneling can be treated by Marcus theory for electron transfer using eqs 8 and 9 as the initial and final electron transfer diabatic states. The electronic coupling at the diabatic state crossing point is given as follows:

$$V_{\mathrm{CPET}} = \frac{|\, H_0^{\mathrm{CPET}} S_{01} - H_{01} \,|}{1 + S_{01}} \tag{10}$$

where $S_{01} = <\Phi_0^{\mathrm{CPET}} \mid \Phi_1^{\mathrm{CPET}}>$ is the overlap integral. The exchange and diagonal matrix elements, defined in terms of CSFs by $H_{01} = <\Phi_0^{\mathrm{CPET}} \mid H \mid \Phi_1^{\mathrm{CPET}}>$ and

$H_0^{CPET} = <\Phi_0^{CPET} | H | \Phi_0^{CPET}>$, are computed using block-localized density functional theory in the present study.[30,80]

The concertedness of the CPET mechanism in the $(PhX)_2H^{\bullet}$, X = O, NH, and CH_2, systems is characterized by the More O'Ferrall–Jencks diagram in the ET and PT transfer coordinates (Figure 4.1). The proton reaction coordinate is conveniently defined by the nuclear positions as follows:

$$\Delta R_p = R_{XH}^{D} - R_{HX'}^{A} \tag{11}$$

where R_{XH}^{D} and $R_{HX'}^{A}$ are, respectively, the distance of the migrating hydrogen from the donor atom X (reactant state) and from the acceptor atom X' (product state). For the electron transfer process, we use the configuration weight χ, corresponding to the initial electronic diabatic state ($\chi = 0$) and the final electronic diabatic state ($\chi = 1$) to monitor the effect of electronic mixing on the protonic configurations. Thus, for a given χ value at the protonic coordinate ΔR_p, we define the following admixture of electronic configurations

$$\Phi^a(\chi, \Delta R_p) = (1-\chi)\Psi_{0a}^{BLKS} + \chi\Psi_{1a}^{BLKS} \tag{12}$$

$$\Phi^b(\chi, \Delta R_p) = (1-\chi)\Psi_{0b}^{BLKS} + \chi\Psi_{1b}^{BLKS} \tag{13}$$

to determine the potential energy $E(\chi, \Delta R_p)$ as a function of the proton transfer (ΔR_p) and electronic mixing (χ) coordinate.[29,30] We note that the coordinate χ can be converted to the Chirgwin–Coulson VB structural weight (both values have a range of 0 to 1 and are identical for the initial and final states),[105,106] which is a more rigorous

representation of the contributions of each VB-like electronic state (eq 8 and 9); here, we have simply used χ in the representation.

4.4 Computational Details

The transition state structures and the minimum energy complexes for the hydrogen atom exchange reaction in $(PhX)_2H\bullet$, X = O, NH, and CH_2, were optimized using the hybrid density functional B3LYP[107,108] with the 6-31G(d) basis set. Similar calculations have been described in the work of Mayer et al. on the phenol and toluene systems.[12] Therefore, these structures are the same as those reported in that work (Figure 4.2). Because of strong hydrogen bonding interactions, the transition structure of

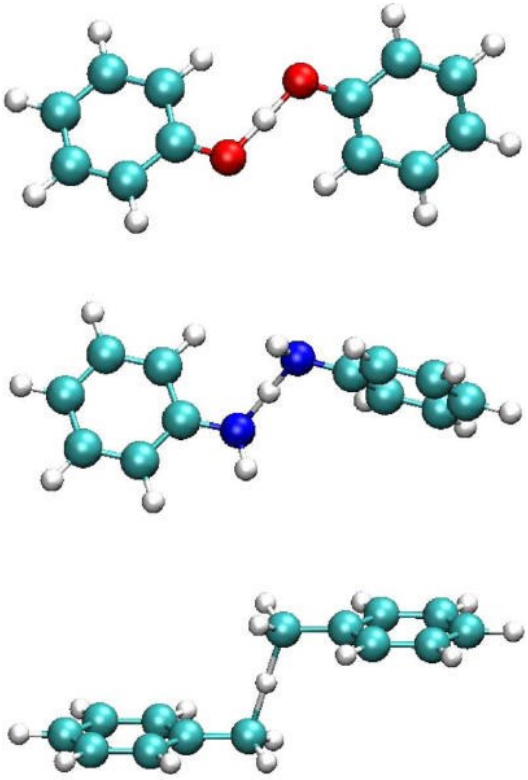

Figure 4.2 Illustration of the optimized transition structures for the hydrogen atom transfer reactions of PhX−H···•X−Ph, where X = O, NH, and CH2, using B3LYP/6-31G(d).

$(PhO)_2H^\bullet$ is close to planar with the transferring hydrogen lying in the molecular plane. For $(PhCH_2)_2H^\bullet$, on the other hand, the transferring hydrogen is nearly perpendicular to the two aromatic rings (Figure 4.2), which are parallel to one another. The transition structure for $(PhNH)_2H^\bullet$ has a geometry intermediate of the arrangements of the other two systems. The computed barriers for hydrogen atom transfer are about 9, 13, and 17 kcal/mol relative to the hydrogen bonding complexes for $(PhO)_2H^\bullet$ and $(PhNH)_2H^\bullet$ and to the separated species for $(PhCH_2)_2H^\bullet$, respectively, which are again similar to those by Mayer et al.[12] A series of BLDFT calculations, also at the B3LYP/6-31G(d) level, were performed along the proton transfer coordinate for each system by varying ΔR_p from 0.0 to 0.75 Å with other atoms fixed at the respective transition structure. The rational is that heavy atom reorganization is slower than hydrogen transfer. This yields the potential energy surfaces for the four diabatic states in each case. For a given proton coordinate, ΔR_p, the adiabatic ground and excited states were determined using these diabatic CSFs. Furthermore, two of the four diabatic CSFs are combined and optimized via configuration interaction to yield the CPET (eqs 8 and 9) and HAT (eqs 6 and 7) effective diabatic states.

Note that the use of B3LYP in the present MSDFT calculations for PCET reactions is different from standard (delocalized) DFT calculations with the B3LYP functional. It is well-known that B3LYP severely underestimates reaction barriers for hydrogen abstraction reactions,[109] partially due to the self-interaction error,[110] which is greater at the transition state since the reactant and product diabatic states are degenerate.

In MSDFT, static correlation effects are partially incorporated in the multiconfigurational approach with VB-like configurations (eqs 1 – 4).[97] Importantly, dynamic correlation effects are retained in the block-localized DFT treatment of these diabatic states.[79] Thus, the use of MSDFT with B3LYP avoids some of the self-interaction errors in that model but still maintains its excellent treatment of dynamic correlation. Borden and co-workers found that the MPW1K model performs "much better" than B3LYP on PCET reactions.[109] Inagaki et al. showed that the enhanced performance correlates with the extent of Hartree-Fock (HF) exchange included in the hybrid functional.[90] B3LYP contains 20% HF exchange, whereas 43% HF exchange is included in MPW1K; the latter was specifically optimized to better reproduce hydrogen atom transfer barriers.[111] Inagaki et al. further examined the performance of long-range corrected BLYP (LC-BLYP) and a LC plus Coulomb-attenuating method (rCAM-B3LYP). The computed barrier for $(PhO)_2H^{\bullet}$ progressively increases with increasing percentage of HF exchange, from about 9 (B3LYP) to 16 (MPW1K) and finally to 24 kcal/mol in rCAM-B3LYP calculations. For comparison, CASSCF, which was also used in the work of Hammes-Schiffer and co-workers,[13] and MRMP/CASSCF barriers are, respectively, about 40 and 12.5 kcal/mol from the hydrogen-bonded complex.[90] The MSDFT barrier is expected to be similar to that from rCAM-B3LYP calculations. Indeed, the computed value is 19.2 kcal/mol from MSDFT/B3LYP calculations. All calculations are performed using a locally modified version of the GAMESS program.[112]

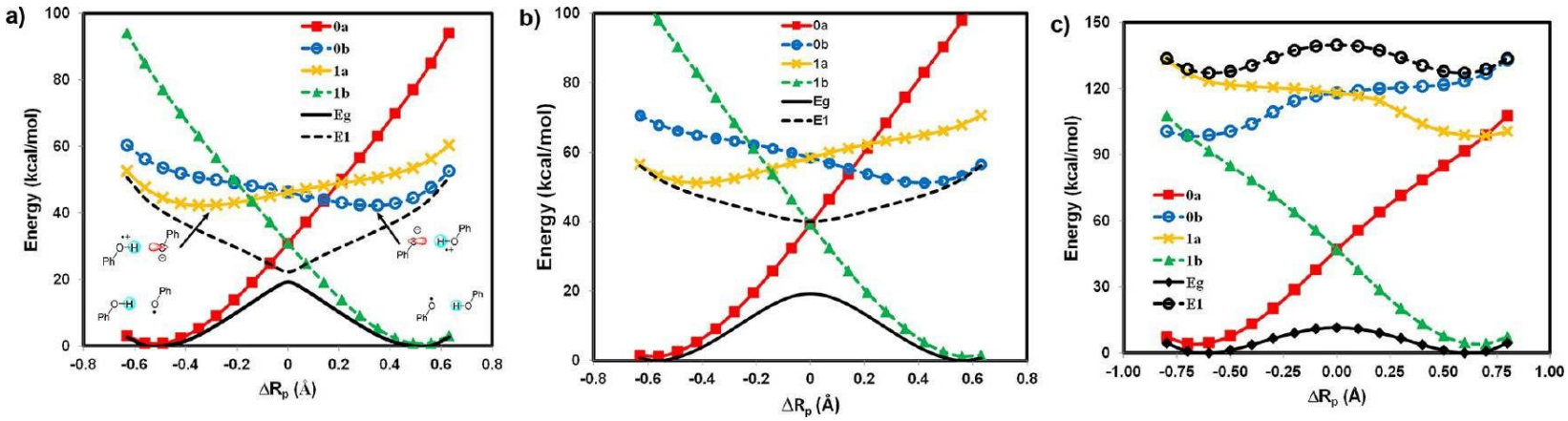

Figure 4.3 Computed potential energy profiles for the diabatic states corresponding to the four corners in a More O'Ferrall− Jencks diagram (Figure 4.1) for the hydrogen atom transfer reactions in $(PhX)_2H\bullet$, where X = O, NH, and CH_2. The proton coordinate, ΔR_p, is defined as the relative distance of the transferring hydrogen from the donor and acceptor atoms. The corresponding wave functions for the individual Lewis structures are specified by Ψ_{0a} [Ph−XH···•X−Ph] in red, Ψ_{1a} [Ph−XH+•···−X−Ph] in brown, Ψ_{0b} [Ph−X−···+•HX−Ph] in blue, and Ψ_{1b} [Ph−X•···HX−Ph] in green. In addition, the adiabatic ground state (Eg) and the first excited state (E1), which are obtained through configuration interaction using the four valence bond configurations, are given in black as solid and dashed curves, respectively. The reaction between the phenoxyl radical and phenol is shown in part a, between PhNH• and aniline in part b, and between the benzyl radical and toluene in part c. All valence bond configurations are determined using block-localized density functional theory with the B3LYP functionals and 6-31G(d) basis set.

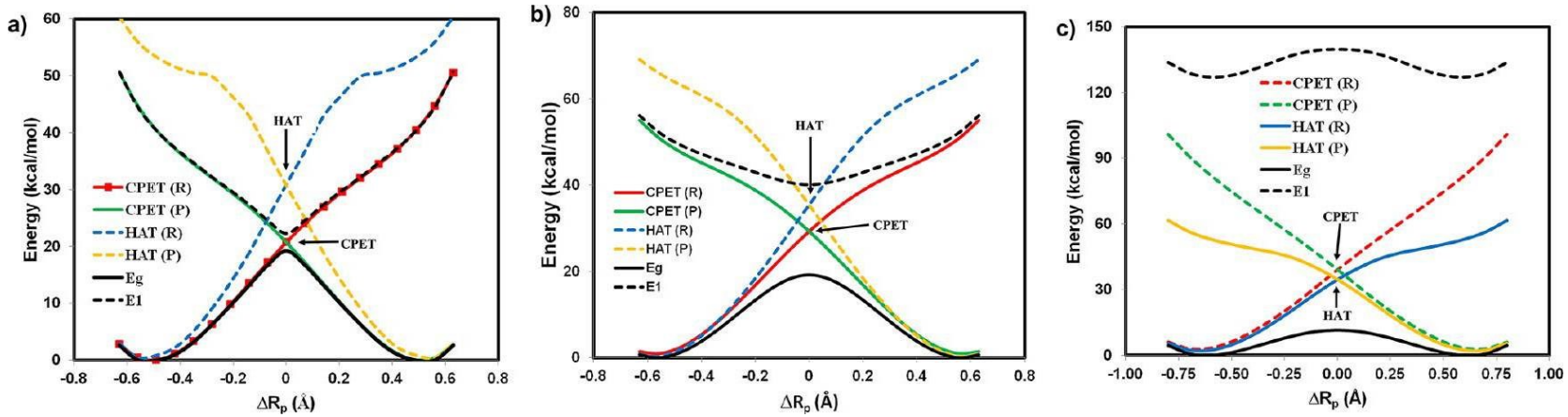

Figure 4.4 Potential energy surfaces for the effective reactant (R) and product (P) diabatic states corresponding to the hydrogen atom transfer (HAT) and to the concerted proton−electron transfer (CPET) mechanisms. For HAT, the electronic states are adiabatic to the localized proton configurations by definition. Thus, the HAT reactant state, HAT(R) in blue, is a combination of the electronically localized states in Figure 4.2 with the proton configuration on the donor site, Φ_R HAT = $c_{0a}\Psi_{0a} + c_{1a}\Psi_{1a}$, and the HAT product state, HAT (P) in brown, is given by Φ_P HAT = $c_{0b}\Psi_{0b} + c_{1b}\Psi_{1b}$. For CPET, electron transfer is nonadiabatic and is assisted by proton transfer. Hence, the CPET reactant state, CPET(R) in red, is a combination of the proton configurations at the donor electronic configuration (see Figure 1), Φ_R CPET = $c'_{0a}\Psi_{0a} + c'_{0b}\Psi_{0b}$, and the CPET product state, CPET(P) in green, is defined by Φ_P CPET = $c'_{1a}\Psi_{1a} + c'_{1b}\Psi_{1b}$. The interactions either between the HAT reactant and product diabatic states, or between the CPET reactant and product diabatic states, result in an avoided crossing, and the interaction (either HAT or CPET) that produces curves that match the adiabatic potential energy surfaces (in black, which is the same as that in Figure 4.2) for the overall reaction is classified as the reaction mechanism. This often coincides with the mechanism with a lower relative energy at the diabatic crossing points. The reaction between the phenoxy radical and phenol is illustrated in part a, between PhNH• and aniline in part b, and the hydrogen abstraction of toluene by the benzyl radical in part c.

4.5 Results and Discussion

Figure 4.3 shows the computed potential energy profiles of the four diabatic states as well as the adiabatic ground and the first excited state for the three hydrogen atom exchange reaction in $(PhX)_2H^{\bullet}$, X = O, NH, and CH_2, using BLDFT with B3LYP/6-31G(d). It is no exaggeration to say that the present calculations provided the first potential energy surfaces of these diabatic states for a PCET process from first principles using an explicit electronic structure theory (of course, these states have often been described in theoretical works and have been modeled empirically). More seriously, Figure 4.3 reveals that there is significant electronic coupling among the four diabatic states, resulting in an avoided crossing and stabilization of the adiabatic potential energy surfaces. The energies of the reactant (Ψ_{0a}^{BLKS}) and product (Ψ_{1b}^{BLKS}) diabatic states show similar behaviors with a rapid increase in energy away from the corresponding equilibrium geometries. The main difference is found in the electron transfer states, Ψ_{1a}^{BLKS} and Ψ_{0b}^{BLKS}, which exhibit greater variations among the three systems. In particular, the energy for Ψ_{1a}^{BLKS} is lower than that for Ψ_{0b}^{BLKS} at the reactant state configuration in the $(PhO)_2H^{\bullet}$ system, but the order is reversed in $(PhCH_2)_2H^{\bullet}$. This reversal is mainly determined by the difference in electron affinity of the free radical species, which are 52, 39, and 21 kcal/mol for X = O, NH, and CH2, respectively. In all cases, it is clear that a simple two-state model involving only the initial reactant and final product states, Ψ_{0a}^{BLKS} and Ψ_{1b}^{BLKS}, is not sufficient to model the present coupled

transfer of an electron and a proton because the diabatic crossing energy is even above the excited state surface in two of the three systems.

The most striking finding in Figure 4.3 is the variation of the energy gap between the adiabatic ground and excited states at the crossing point of the diabatic states (ΔR_p = 0.0 Å), changing from a value of 3.0 kcal/mol for $PhOH\cdots^{\bullet}OPh$, to 20 kcal/mol for $PhNH_2\cdots^{\bullet}NHPh$, and finally to 128 kcal/mol for $PhCH_3\cdots^{\bullet}CH_2Ph$. For comparison, the energy gap for $PhOH\cdots^{\bullet}OPh$ from a recent SA-CASSCF(11,10) (MCQDPT) calculation is 4.4 (3.8) kcal/mol,[90] the original study of Mayer et al.[12] reported a value of 3.7 kcal/mol from CASPT2(15,14), in reasonable agreement with the present result. Qualitatively, one can immediately conclude that the hydrogen migration in the phenoxyl–phenol system follows an electronically non-adiabatic path, whereas the very large avoided crossing energy at the transition state of the benzyl radical–toluene reaction ensures that the reaction takes place entirely on the adiabatic ground state. This is consistent with the conclusions on the basis of orbital symmetry[9,12] and of adiabaticity parameters from analysis of CASSCF(3,6)/6-31G results involving three active electrons.[13]

The symmetric aniline system in Figure 4.3b, $PhNH_2\cdots^{\bullet}NHPh$, has not been theoretically investigated. On the basis of the qualitative trends in Figure 4.3b, however, it is not straightforward to draw conclusions on its adiabatic or non-adiabatic character, nor the nature of orbital alignments, except that it is a concerted PCET. Thus, additional

analyses of the diabatic and adiabatic states are necessary to shed light on its mechanistic character.

Figure 4.4 depicts the energy curves of the HAT (eqs 6 and 7) and the CPET mechanism (eqs 8 and 9) diabatic states for the three hydrogen exchange reactions, along with the adiabatic ground and excited states already depicted in Figure 4.3. First, in the reaction of $PhOH\cdots^{\bullet}OPh$ (Figure 4.4a), the diabatic crossing energy for the CPET reactant and product states is lower than that of the HAT configurations by 10.2 kcal/mol. In fact, the diabatic crossing point for the HAT configurations is above the energy of the adiabatic excited state, suggesting that the coupled transfer of a proton and an electron in the phenoxyl radical–phenol system cannot be adequately described by the mixing and avoided crossing of HAT diabatic states because the resonance of the two diabatic configurations will necessarily yield two adiabatic states, one above (out-phase combination) and one below (in-phase combination) the crossing point.[91–94] Comparison of the qualitative features of the CPET diabatic states and the adiabatic potential energy surfaces in Figure 4.4a shows that the diabatic and adiabatic surfaces essentially overlap, except near the critical region where non-adiabatic coupling is promoted by an intersection of the CPET diabatic configurations.[10,20,33,91,95,96] This demonstrates that the CPET reactions of phenoxyl radical and phenol involve both ground and excited state potential energy surfaces, which can be modeled by using the CPET diabatic states.

The effective two-state diabatic and adiabatic potential surfaces for the reaction between toluene and the benzyl radical[9,12] are displayed in Figure 4.4c, which exhibits very large coupling to promote a strongly avoided crossing along the entire proton

coordinate. The energy gap is 128 kcal/mol at the crossing point, similar to that found for hydrogen transfer reactions involving only σ bonds.[14,113] In this case, the hydrogen transfer occurs entirely on the electronically adiabatic potential surface, consistent with previous conclusions.[9,12–14] Notably, the diabatic crossing energy for the HAT mechanism is lower than that of the PCET process, which loses meaning in such a fully electronically delocalized, adiabatic resonant system. Nevertheless, it indicates that the HAT diabatic states are lower energy configurations than CPET states for the hydrogen abstraction of toluene by a benzyl radical.

The trend in the diabatic and adiabatic potential energy profiles for the reaction of $PhNH_2\cdots^{\bullet}NHPh$ is intermediate of that of the phenol and toluene systems. In this case, the preference for CPET or HAT mechanisms is not straightforward simply by inspecting the "adiabaticity" or the energy gap of the potential energy surfaces. Figure 4.4b shows that the energy at the crossing point between the CPET diabatic states (eqs 8 and 9) is lower than that of the HAT states (eqs 6 and 7) by about 7 kcal/mol, suggesting that the hydrogen atom exchange in $PhNH_2\cdots^{\bullet}NHPh$ is best described as a CPET process. Clearly, unlike the case of $PhOH\cdots^{\bullet}OPh$, it is expected that there is significant competition with the overbarrier process in the HAT mechanism (see discussion below).

The electronic coupling energies, V_{CPET}, for the three hydrogen exchange reactions are 1.5, 10, and 23 kcal/mol for $(PhX)_2H^{\bullet}$ ($X = O, NH, CH_2$), respectively, which may be compared with the corresponding values of 2.0 and 40.9 kcal/mol for X = O and CH_2 determined by Skone et al. using CASSCF(3,6)/6-31G.[13] The magnitude of

electronic coupling for the aniline system in Figure 4.3b, $PhNH_2 \cdots^{\bullet} NHPh$, is on the borderline between an adiabatic and a non-adiabatic process.

4.6 Comparison to Ab Initio Valence Bond Theory

To provide further insight on the nature of valence bond orbital interactions, we have performed ab initio valence bond self-consistent field (VBSCF) calculations for the $PhOH \cdots^{\bullet} OPh$ system at the transition state.[114–116] The main purpose here is to illustrate the connection and difference between MSDFT and ab initio VB theory. The VB space for the coupled proton and electron transfer includes three orbitals and three electrons, which result in a total of eight CSFs depicted in Figure 4.5. The equivalence between the present diabatic states defined in eqs 1– 4 and can be readily established.[29] For example, the BLDFT determinant for the state in which both electron and proton are localized in the donor fragment (eq 1), Ψ_{0a}^{BLKS}, corresponds to a linear combination of VB configurations 1,4, and 5 in Figure 4.5. The product state, Ψ_{1b}^{BLKS} (eq 4), results from a combination of VB configurations 2, 6, and 7. These are the corresponding Lewis structures. In both cases, four determinants are needed to construct the VB wave function, whereas a single determinant is used in the BLDFT representation. In VBSCF, an electronic coupling of 0.01 kcal/mol (3.7 cm^{-1}) was obtained, much smaller than MSDFT and CASSCF results (the origin of this difference is not clear).

Figure 4.6 illustrates the optimized VB orbitals in the VB wave function both for HAT (Figure 4.6a) and CPET (Figure 4.6b) mechanisms. Note that for the HAT state (eqs 6 and 7), the optimized orbital on the migrating hydrogen atom is aligned along the

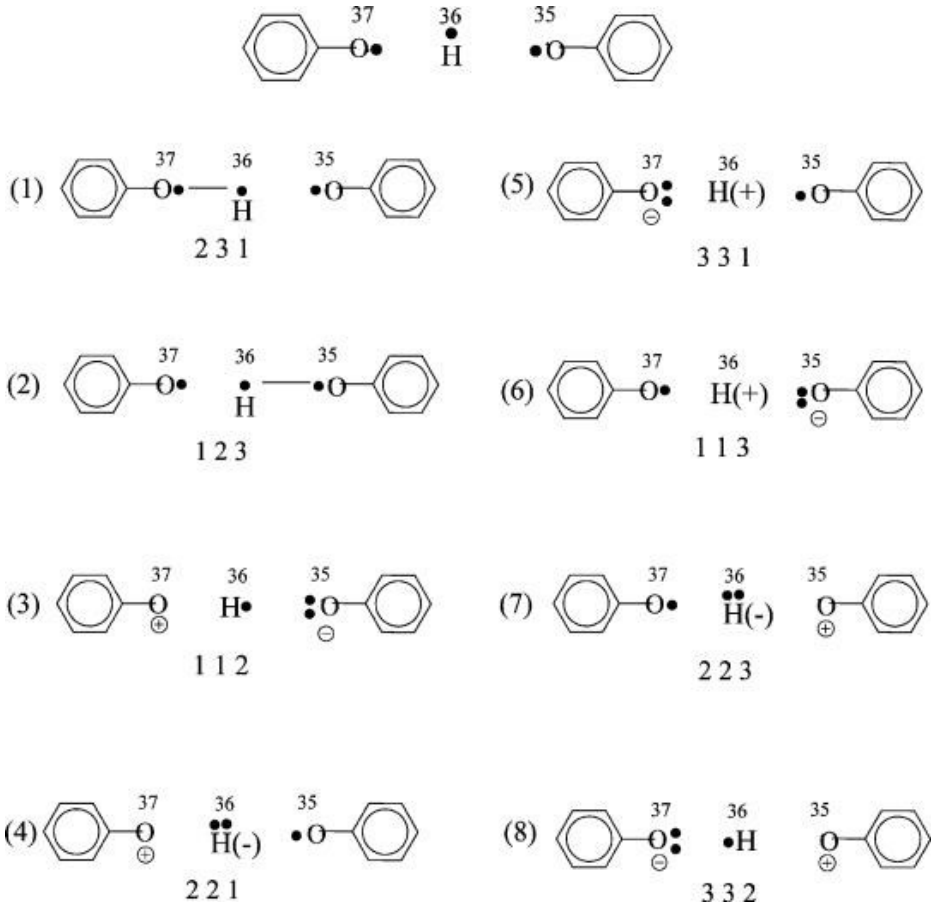

Figure 4.5 Illustration of the valence bond configuration state functions used in ab initio VBSCF calculations. The top structure illustrates the three valence bond orbitals (orbital numbers 35, 36, and 37); for convenience, they are labeled as VB orbitals 1, 2, and 3, respectively. The optimized VB orbitals are depicted in Figure 4.6. The sequence of three numbers under each VB configuration specifies the orbital occupied by an electron. The dashed (bond) line between two atoms specifies spin coupling between two electrons, which are listed first in the sequence. For example, in VB configuration (1), the sequence, 231, denotes the determinant wave function of $\alpha(2)\beta(3)\alpha(1)-\beta(2)\alpha(3)\alpha(1)$, involving VB orbitals 2, 3, and 1.

vector from the donor to the acceptor atom. This VB orbital is orthogonal to the two π-type fragment orbitals on the donor and acceptor fragmental orbitals. Thus, the mixing of these localized fragment orbitals results in extended delocalization in the CPET mechanisms. The qualitative features from VBSCF are in excellent agreement with the analyses of Mayer et al.,[12] but they were obtained for two transition structures for two

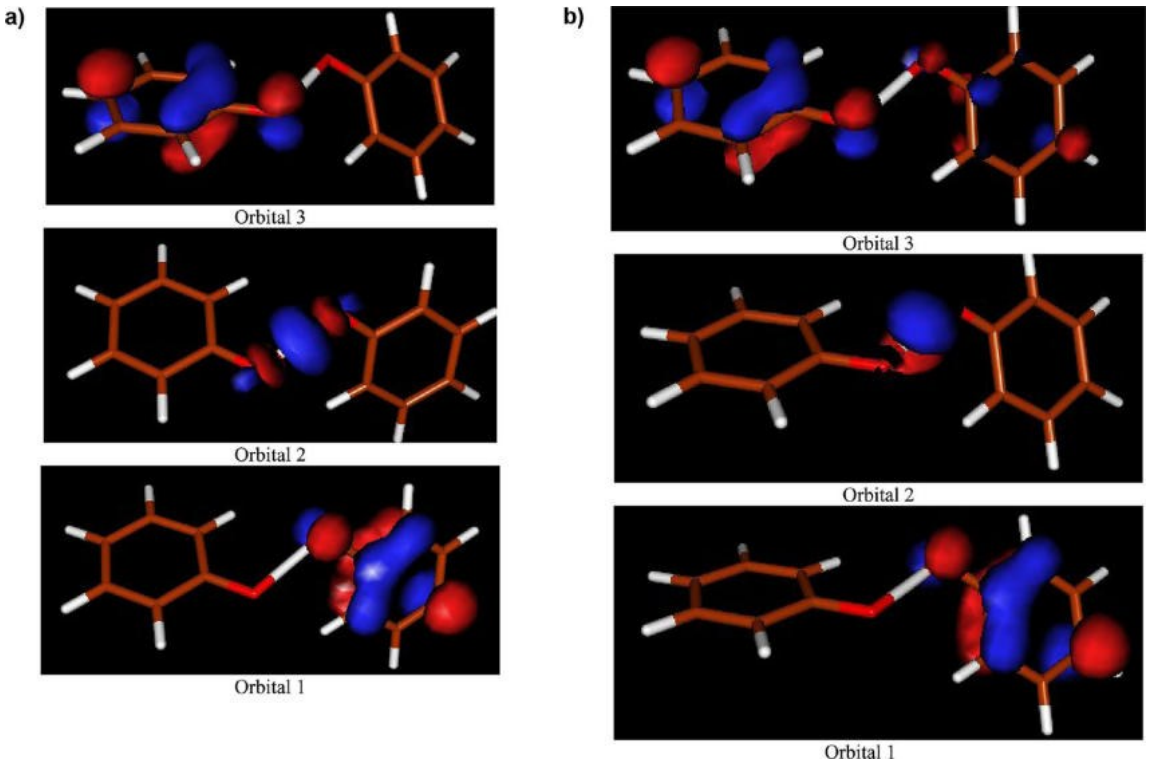

Figure 4.6 Optimized valence bond orbitals (a) for the HAT diabatic state and (b) for the PCET diabatic state at the transition state for the hydrogen exchange reaction between phenoxy radical and phenol. Although the same basis orbitals are used, the resulting VB orbitals are different for different mechanisms because of the constraint of selecting different VB configurations (Figure 4.5) to define HAT or CPET mechanisms (see text for the corresponding definition). Here, we establish that these constraints in VBSCF are equivalent to the definition in MSDFT by eqs 7−10, although the former utilizes multideterminants for each diabatic state, and the latter makes use of a computationally more efficient, single-determinant approximation. In both mechanisms, orbitals 1 and 3 are dominantly localized on the two phenoxy fragments, respectively. For the HAT mechanism (a), orbital 2 for the migrating hydrogen is aligned along the vector between the donor and acceptor oxygen atoms. For the CPET mechanism (b), the hydrogen orbital is perpendicular to that vector. Note that the local VB orbitals cannot be directly compared with the delocalized molecular orbitals from conventional MO or DFT calculations. It is also interesting to point out that one can specifically define HAT or CPET orbitals by making different combinations of the VB configurations in Figure 4.5 in VBSCF, corresponding to those defined in MSDFT by eqs 7−10. This is not possible in delocalized molecular orbital or density functional calculations.

reactions with different mechanisms. The orbital features associated with the two mechanisms are naturally produced on the same structure for the same reaction – an analysis that can be performed using a localized VB theory, but not possible using

delocalized MO or KS-DFT approaches. This is precisely the reason why VB theory can provide insights into understanding PCET reactivity. More importantly, the illustration in Figure 4.6 demonstrates that the determining factor of a HAT or CPET mechanism is not simply an orbital alignment of molecular or KS orbitals – they are important and relevant but not sufficient. The HAT and CPET reactivity is blended, involving the same VB structures, albeit to different extents, and HAT and CPET compete kinetically to contribute to the overall rate.

4.7 Comparison with Shaik's VBSCD Approach

It has brought our attention from an anonymous referee that two articles on a valence-bond view of hydrogen transfer reactions have been published at about the time this article was submitted to this journal. Those studies provided an informative perspective of HAT and CPET reactions based on the valence bond state correlation diagram (VBSCD) that was introduced by Shaik,[92,93] and has been extensively used on a broad range of chemical and biological reactions.[93,117–119] Consequently, we make a comparison of the key features between that work and the present MSDFT study.

The VBSCD theory as applied to HAT and CPET reactions is summarized in Figure 4.7, following closely the nomenclature and discussion of the original Figures in refs 95 and 96. Figure 4.7 contains two sets of VB-state curves, corresponding to the "normal HAT" process in solid curves and to a proton transfer (by mixing the two PT curves) in dashed curves.[95,96] The four low-energy structures, two on the reactant (R) side ($\Psi_{\mathrm{HAT},R}$ and $\Psi_{\mathrm{PT},R}$) and two on the product (P) side ($\Psi_{\mathrm{HAT},P}$ and $\Psi_{\mathrm{PT},P}$), are formally the same VB diabatic configurations depicted in the More O'Ferrall–Jencks

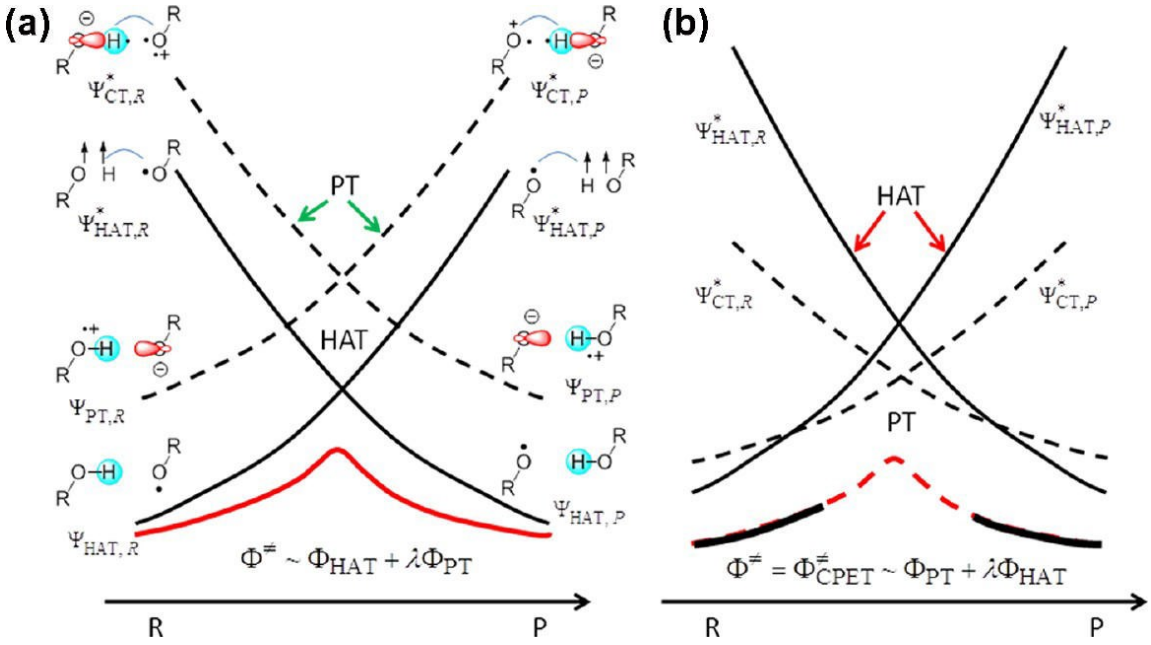

Figure 4.7 VBSCDs describing the dichotomy of HAT and PCET processes by mixing normal HAT valence bond states (solid curves) and proton transfer (PT) curves (dashed curves) along the reaction coordinate. Part a represents a case where the PT states lie higher than the HAT state. The wave function of the transition state ($\Phi^{\ddagger}$) has a dominant HAT character with a secondary PT component ($\lambda < 1$). The wave function for HAT is generated by mixing the two HAT diabatic configurations ($\Phi_{HAT} = a_R\Psi_{HAT,R} + a_P\Psi_{HAT,P}$) and that for PT by mixing the PT states ($\Phi_{PT} = b_R\Psi_{PT,R} + b_P\Psi_{PT,P}$). Part b illustrates a case where the PT curves are low-lying and descend below the HAT crossing point. The transition state is now a PCET type with predominant PT character and a secondary HAT contribution ($\lambda < 1$). This figure was redrawn to match the present discussion based on Figure 6 of ref 96.

diagram (Figure 4.1) and the diabatic curves shown in Figure 4.3. The VB energy curves presented in refs 95 and 96 were drawn qualitatively based on the energies at the extreme (R and P) points. The common connection to Figure 4.1 suggests that MSDFT in this work can be used to quantify the state energies in VBSCD.

In VBSCD, the HAT product VB configuration at the reactant geometry is called the promoted state, labeled as $\Psi^*_{HAT,R}$ (also called image state, excited state, or prepared state), of the HAT reactant, which features triplet decoupling of the O–H bond electrons

and repairing of the electron on $H^{\bullet}$ with the electron on the acceptor oxygen atom; a similar product promoted state is denoted. The relative energies of the promoted states can be related to bond dissociation energies and radical structural reorganization energies, etc.[91,95,96] The promoted states for the PT curves are called charge transfer (CT) states, so labeled in Figure 4.7 as in the original papers.[95,96] For example, the promoted state of the PT curve for the *R* state ($\Psi_{PT,R}$) is denoted by $\Psi^{*}_{CT,R}$, which is the P state of the PT curve ($\Psi_{PT,P}$) at the R geometry. In MSDFT, we simply call these VB states diabatic and adiabatic states with an aim for rate calculations using the Marcus theory approach.[37,98] Note that the PT process of the "CT" states from $\Psi_{PT,R}$ to $\Psi_{PT,P}$ (Figure 4.7) is in fact accompanied by an electron transfer in the opposite direction; thereby, the process may be called an *anti*-PCET process.

The conceptual understanding of HAT and CPET mechanisms from VBSCD analyses is depicted in Figure 4.7. Figure 4.7a presents a case where the CT states lie higher than the HAT states; thereby, "the wave function of the transition state has a dominant HAT character with a secondary PT character".[95,96] On the other hand, Figure 4.7b shows a scenario where the CT curves descend below the crossing point of the HAT curves. Consequently, the transition state is now a CPET-type with a predominant PT character and a secondary HAT contribution.[95,96] Since the ground states at the reactant and product geometries are still dominated by the HAT states, the result of VB mixing is a CPET transition state for a net HAT reaction. Therefore, according to the VBSCD theory of refs 95 and 96, the relative heights of the HAT and PT crossing points determines the transition state character.

In principle, the VB characterization of proton-coupled electron transfer is conceptually the same from VBSCD and MSDFT theories,[91–93] but there are also important differences. In MSDFT, each of the diabatic HAT state curves is electronically adiabatic, where the proton is associated with either the donor or the acceptor Lewis structures. Therefore, the HAT states are admixtures of the ET states (eqs 6 and 7, blue and yellow curves in Figure 4.4). We do not invoke the type of PT process described in refs 95 and 96 (see Figure 4.7), although such a PT reaction can be studied with MSDFT with these four basic VB states. In MSDFT, the PCET state curves (not necessarily CPET) are represented as ET diabatic configurations assisted by PT (eqs 8 and 9, red and green curves in Figure 4.4). The mixing and avoided crossing of the *two* HAT states and of the *two* PCET states, although both include the contributions from all four basic diabatic configurations in Figure 4.3, generate the adiabatic ground state for the HAT and for the CPET pathways, respectively. The adiabatic ground state surface from one of the two mechanisms that matches the adiabatic ground state obtained from all four independent states (Figure 4.3) is recognized as the mechanism with a greater contribution to the overall PCET reaction and, thus, is simply characterized as the reaction mechanism. Often, a simple, straightforward indicator is the relative energies at the crossing points of the HAT and CPET state curves, with the lower curve best representing the reaction mechanism from a VB state interaction perspective.

For the phenoxyl–phenol system, the rule of diabatic crossing (RDC) predicts that the mechanism follows predominantly a CPET process in our approach (Figure 4.4) since the energy of the CPET crossing point is lower than that of the HAT one. However, when

the MSDFT energies are used, the corresponding PT curves in VBSCD analysis are above the HAT curves (Figure 4.4). Thus it would have been a HAT according to VBSCD. For the benzyl-toluene, both methods correctly predict that the net hydrogen atom abstraction is a HAT.

Clearly, there is no strict division between HAT and CPET, and they are not kinetically distinguishable; the overall rate is a sum of the two processes, where some reactions may have a greater HAT contribution while others less. As pointed out by Shaik and co-workers, since ET states are the basis configurations for the PCET process, "unlike HAT, the PCET reaction is expected to be sensitive to solvation".[95] MSDFT provides a procedure to estimate the reaction rates both for HAT and for CPET processes,[37,98] the sum of which can be compared with experimental kinetic data.

The VBSCD and MSDFT approaches to PCET reactions have many similarities, both making use of diabatic crossing energies as a simple rule-of-thumb, RDC, criterion to understand the mechanistic character for these processes. The VB state curves from MSDFT can be considered as a VBSCD diagram.

4.8 Origin of CPET and HAT Mechanisms

The origin of the non-adiabatic CPET mechanism and the adiabatic HAT reaction are revealed in Figures 4.8 – 4.10, in which the two-dimensional More O'Ferrall-Jencks plots have been extended to three dimensions, including both the ground and excited state PES. This is significant because the extension highlights the difference between the two concerted mechanisms, both following the diagonal path in Figure 4.1. Figure 4.8a illustrates the PES for the adiabatic ground and excited states of the $PhOH\cdots^{\bullet}OPh$

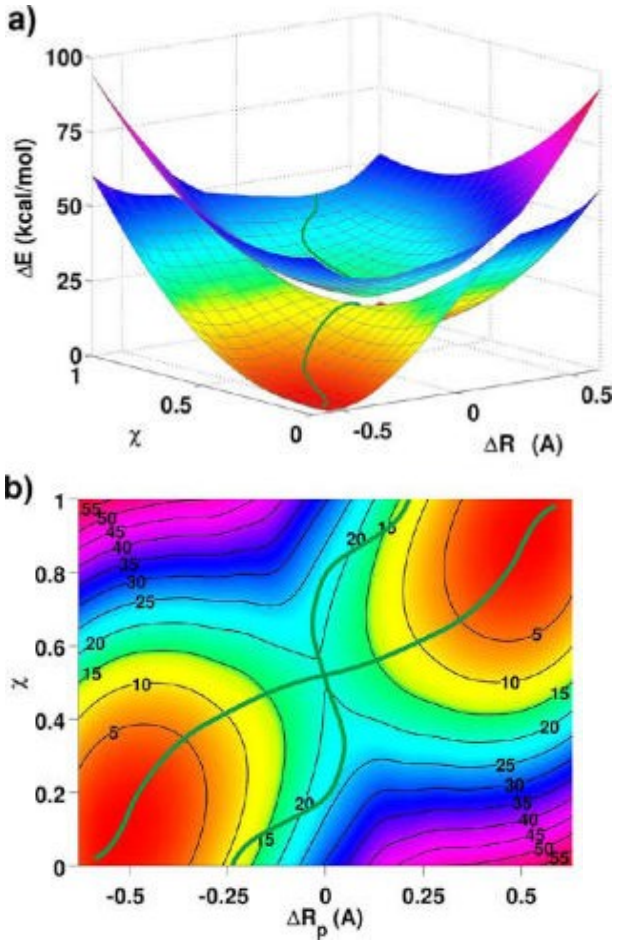

Figure 4.8 (a) Computed two-dimensional potential energy surfaces for the adiabatic ground state and the first excited state as a function of the proton transfer (ΔR_p) and the electron transfer (χ) coordinates for the proton and electron transfer between phenol and the phenoxy radical. (b) Minimum energy paths of the adiabatic ground state and the excited state overlaid on the isoenergy contours for the ground state. Multistate density functional theory is used in all calculations with the B3LYP functional along with the 6-31G(d) basis set.

reaction, and PT and ET processes are fully concerted in the ground state potential surface with a net hydrogen atom transfer. A striking finding is that the separations between the ground and excited state surfaces are close in energy along a seam in the direction nearly orthogonal to the minimum energy path on the adiabatic ground state. The topographical features of the adiabatic ground and excited state surfaces in Figure 4.8a suggest that a conical intersection seam can be located by a slight distortion in the

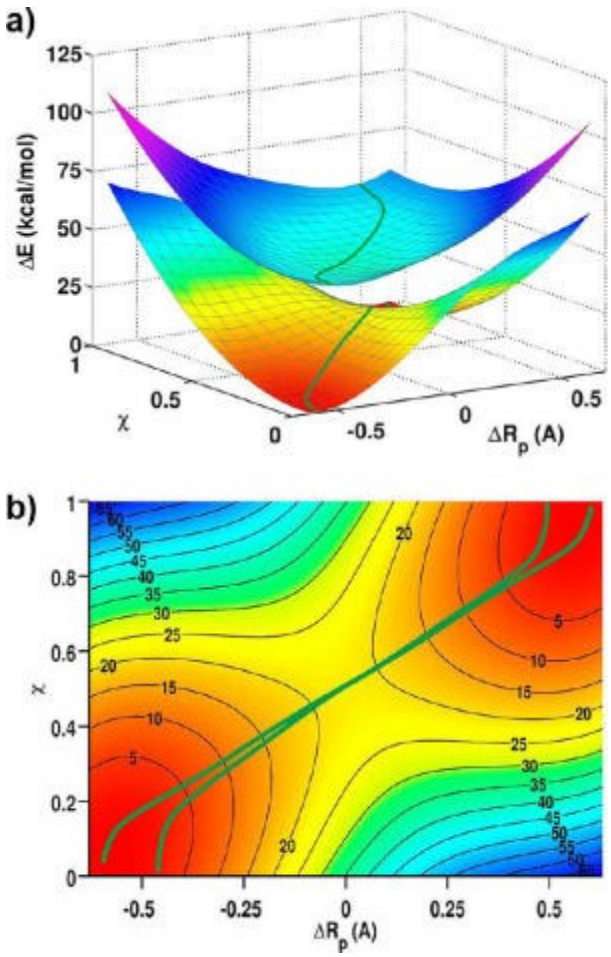

Figure 4.9 (a) Computed two-dimensional potential energy surfaces for the adiabatic ground state and the first excited state as a function of the proton transfer (ΔR_p) and the electron transfer (χ) coordinates for the proton and electron transfer between aniline and PhNH• radical. (b) Minimum energy paths of the adiabatic ground state and the excited state overlaid on the isoenergy contours for the ground state. Multistate density functional theory is used in all calculations with the B3LYP functional along with the 6-31G(d) basis set.

molecular geometry. The involvement of both the adiabatic ground and excited state PES, through a conical intersection seam, provides an important insight on the CPET mechanism as also described by Tishchenko et al.[14] Interestingly, there is significant mixing between the proton-localized diabatic states for each electronic configuration (eqs 8 and 9), but the interaction between the two electronic configurations is small. As a result, the CPET diabatic states defined in eqs 8 and 9 are more stabilized (lower in

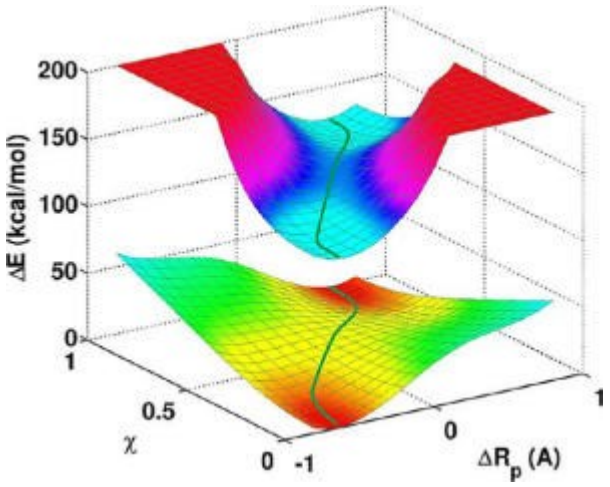

Figure 4.10 Computed two-dimensional potential energy surfaces for the adiabatic ground state and the first excited state as a function of the proton transfer (ΔR_p) and the electron transfer (χ) coordinates for the hydrogen abstraction of toluene by benzyl radical. Multistate density functional theory is used in all calculations with the B3LYP functional along with the 6-31G(d) basis set.

energy) than the HAT diabatic states (eqs 6 and 7).

We found that the minimum energy paths on the ground and the first excited state surfaces are roughly orthogonal in the critical region for the reaction in the PhOH···$^{\bullet}$OPh system (Figure 4.8b). As a result, the minimum energy path on the excited state surface and the ridge separating the reactant and product states of the ground state follow the same coordinates, resulting in a low energy conical interaction seam accessible through thermal motions. The implication is that although vibronic overlap can be an important factor in rate computation, the availability of thermally accessible conical intersections provides an alternative prediction for the rate of CPET reactions. In contrast, the hydrogen abstraction reaction between toluene and benzyl radical has significant overlay among the VB diabatic states, in which electronic configuration mixing dominates the entire process (Figure 4.10). Thus, the large electronic resonance between

the electronic diabatic states promotes a strongly avoided intersection, resulting in a large energy gap between the adiabatic ground and excited states. For the HAT reaction of $PhCH_2H\cdots^{\bullet}CH_2Ph$, the minimum energy path on the adiabatic ground surface essentially coincides with that on the excited state. In such a fully adiabatic process, separation of the electron transfer coordinate from the proton transfer coordinate loses meaning. Consequently, a *single* reaction coordinate is sufficient to represent the HAT reaction.

The topographic features of the adiabatic ground and excited state surfaces for the $PhNHH\cdots^{\bullet}NHPh$ reaction are intermediate of CPET in $PhOH\cdots^{\bullet}OPh$ and HAT in $PhCH_2H\cdots^{\bullet}CH_2Ph$. There is clear separation between the adiabatic ground and excited state surfaces along the ET and PT coordinates (Figure 4.9a), yet the energy gap is far smaller than that for the hydrogen abstraction of toluene by the benzyl radical. The minimum energy paths on the adiabatic ground and excited states are now oriented with significant overlap (Figure 4.9b). Thus, $PhNH_2$ and $^{\bullet}NHPh$ represent a reaction that is on the borderline of CPET and HAT mechanisms.

4.9 Conclusions

We have described a procedure to use constrained density functional theory through block-localization of Kohn-Sham orbitals to determine the electron- and proton-localized diabatic states associated with the coupled proton and electron transfer reactions in the isoelectronic series of $(PhX)_2H^{\bullet}$, where $X = O, NH, \text{and } CH_2$. Then, these valence bond-like diabatic states are used in configuration interaction to yield the

potential energy surfaces for the adiabatic ground and excited states. To distinguish the mechanistic difference between CPET and HAT, we formulated a pair of effective two-state VB models, respectively, by combining the proton-localized configurations at fixed electronic diabatic states, or by combining the electronic diabatic states for given proton configurations.

Using MSDFT, we found that the relative energies at the intersection of the CPET and HAT diabatic states, called the rule of diabatic crossing (RDC), can be used as an energetic criterion to classify the two reaction mechanisms. Thus, if the energy at the crossing point for the CPET diabatic states is lower than that for the HAT diabatic states, the reaction mechanism may be considered to have a greater concerted proton-electron transfer character. Conversely, if the energy at the crossing point of the HAT diabatic states is lower than that of CPET states, the HAT mechanism is a preferred process. A similar analysis has been reported by Shaik and co-workers based on valence bond state correlation diagrams, although different criteria are used. For the extreme cases, the results from VB-based approaches are consistent with proposals using electronic adiabaticity. It is emphasized that there is no strict division of HAT and CPET mechanisms for a given reaction, and they are not distinguishable based solely on phenomenological kinetic parameters. Both contribute and the overall rate is the sum of the individual processes. The diabatic states and potential energy surfaces defined for HAT and CPET processes from first principles calculations can be used to determine these rate constants.

The origin of relatively small electronic coupling in the CPET-dominated mechanism of the phenolic system is revealed in a More O'Ferrall–Jencks diagram extended to the third dimension that includes both the ground and excited potential energy surfaces. Although electron transfer and proton transfer are concerted both for CPET and HAT (thus, not distinguishable with the classical picture of a two-dimensional More O'Ferrall–Jencks plot), the mechanistic difference is distinguished by the presence of a low-energy conical intersection seam in the direction perpendicular to the minimum energy path on the adiabatic ground state. This results in minimal overlap interaction between the electronic diabatic states and weak electronic coupling. On the other hand, the minimum energy path of the adiabatic ground state for the HAT mechanism in toluene–benzyl radical system coincides with that on the excited state as a result of large electronic coupling that separates the two surfaces by more than 5 eV (~130 kcal/mol).

The topographic features for the PhNHH···$^{\bullet}$NHPh system are found between those for the CPET reaction of phenoxyl radical and phenol and for the HAT mechanism of benzyl radical and toluene. The minimum energy paths on the adiabatic ground and excited states are oriented with significant overlap. In this case, it is predicted that both HAT and CPET processes compete, and the dominating contribution may be tuned with varying solvent polarity and hydrogen bonding abilities since HAT and CPET have different ionic characters and different sensitivities to solvent effects.

Chapter 5. Nocera's Donor-Amidinium-Carboxylate-Acceptor Model Complex

5.1 Introduction

In this chapter, MSDFT is used to study a system developed by Nocera to model long-range electron transfer coupled to short-range proton transfer within a hydrogen-bonded salt-bridge interface linking the electron donor and acceptor molecules.[20] The role of the salt-bridge is twofold. First, it separates the electron donor and acceptor molecules at a sufficiently long distance to ensure weak electronic coupling. Second, the insertion of a hydrogen bonded interface directly in the electron transfer pathway effectively couples the two reactions, electron transfer and proton transfer. In this way, Nocera developed a well-defined model system that ensures an electronically non-adiabatic PCET process. Given the experimental evidence provided by Nocera's work, Cukier[32] and Hammes-Schiffer[33] applied theoretical models that reproduce the experimental driving forces and rate constants. Here, we use Nocera's model system to validate MSDFT against previous experimental and theoretical works and demonstrate the additional insight provided by this method for understanding the mechanistic details of asymmetric PCET reactions.

5.2 Background Information

To systematically study the energetic and kinetic properties of PCET Nocera developed a series of donor-salt-bridge-acceptor complexes in which the rate of electron transfer is dependent on the protonation state of the salt-bridge interface.[10,20] The complex consists of a ruthenium metal center with three bipyridine ligands, one of which is modified by a carboxylate or amidinium group that forms a salt bridge interface with the electron acceptor molecule, dinitrobenzoate (Figure 5.1). After photo-excitation, the

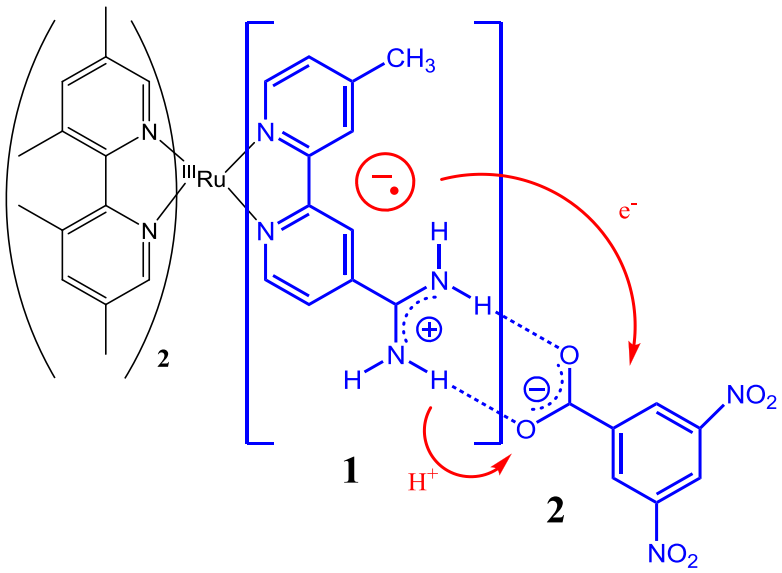

Figure 5.1 Following photoexcitation, a Ru(II) undergoes metal to ligand charge transfer (MLCT), localizing an excited electron on a bipyridine ligand linked to an electron acceptor molecule, dinitrobenzoate, through an asymmetric salt-bridge interface. ET occurs from the bipyridine ligand to dinitrobenzoate with the electron-withdrawing nitro groups driving the transfer, while PT occurs through the hydrogen-bonded amidinium-carboxylate interface.

Ru(II) center undergoes metal-to-ligand charge transfer (MLCT), localizing the excited electron on one of its bipyridine ligands.[20] Care was taken to ensure that MLCT localizes the excited electron on the salt-bridge-modified ligand by raising the energy of the first excited state of the unsubstituted bipyridine ligands. Once localized on the bipyridine ligand covalently linked to the salt-bridge interface, ET across is driven by the electron-withdrawing nitro groups on dinitrobenzoate.

The salt-bridge interface links the electron donor and acceptor molecules at a well-defined distance, controlling the degree of electronic coupling. Well-known by Marcus theory,[51] the rate of ET diminishes with increasing donor-acceptor distance. Covalently-bonded benzene rings of variable length have also been used to modulate the distance-dependence of electronic coupling, but the salt-bridge interface has the added

benefit of introducing a PT reaction coordinate between ET donor-acceptor molecules. In this way, electronically non-adiabatic ET, determined solely by the sufficiently long distance between donor/acceptor molecules, is coupled to the dynamics of PT within the salt-bridge interface. Additionally, the electronic state of the donor-acceptor pair is thought to alter the PES of PT, rendering it more or less thermodynamically favorable.

Experimental studies on the donor-amidinium-carboxylate-acceptor (DNOA) complex and the donor-carboxylate-amidinium-acceptor (DONA) complex have demonstrated the versatility of this design in probing the thermodynamic and kinetic properties governing PCET processes.[10,20] It is found that ET is significantly slower in DNOA than DONA, which is attributed to internal dipole of the salt-bridge interface with respect to the direction of ET. With the dipole opposing ET in DNOA, the driving force (ΔG^o) is reduced by 0.2 eV compared to the switched DONA interface. In addition, the DNOA salt-bridge interface requires large charge redistribution to stabilize the excited electron on dinitrobenzoate, thus leading to larger solvent polarization effects dependent on the proton position. As a result, the overall rate constant is dependent on the overlap of vibrational wavefunctions (i.e. Franck-Condon overlap), in addition to the electronic coupling. Lastly, the strength of the hydrogen-bond is suggested to indicate the degree of electronic coupling.

These well-defined model systems have been investigated using theoretical models developed by Cukier[10,27] and Hammes-Schiffer,[24,25] reviewed in Chapter 2. Cukier emphasizes that given the electronic structure of the solute, solvent polarization and differences in Franck-Condon factors determine the preferred PCET mechanism,

concerted vs. stepwise.[32] Hammes-Schiffer also discusses the thermodynamics and solvent effects, but emphasizes the role of excited adiabatic states in determining the preferred PCET mechanism.[33] From the work of Hammes-Schiffer, PCET is slightly endothermic in DNOA and exothermic in DONA with larger electronic coupling in DONA. These results align with experimental results that ET is faster in DONA than DNOA.

5.3 Methodology

Here, we use multistate density functional theory (MSDFT)[29,30] to model PCET in Nocera's DNOA model complex (Figure 5.1). Following the MSDFT approach to modeling PCET mechanisms discussed in Chapter 3, the four charge-localized diabatic states for PCET in Nocera's DNOA model system are defined as

$$D_e^- - NH^+ \cdots O^- - A_e; \quad \Psi_{0a}^{BLKS} = \hat{A}\{\Omega_{0a}^1(D_e^- - NH^+)\Omega_{0a}^2(O^- - A_e)\} \tag{1}$$

$$D_e^- - N \cdots HO - A_e; \quad \Psi_{0b}^{BLKS} = \hat{A}\{\Omega_{0b}^1(D_e^- - N)\Omega_{0b}^2(HO - A_e)\} \tag{2}$$

$$D_e - NH \cdots O - A_e^-; \quad \Psi_{1a}^{BLKS} = \hat{A}\{\Omega_{1a}^1(D_e - NH)\Omega_{1a}^2(O - A_e^-)\} \tag{3}$$

$$D_e - N \cdots HO - A_e^-; \quad \Psi_{1b}^{BLKS} = \hat{A}\{\Omega_{1b}^1(D_e - N)\Omega_{1b}^2(HO - A_e^-)\} \tag{4}$$

where D_e represents the salt-bridge substituted bipyridine ligand, A_e represents dinitrobenzoate, and the amidinium-carboxylate salt-bridge is represented by one of its $N \cdots H \cdots O$ hydrogen bonds. This is an oversimplification of the VB structure of the amidinium-carboxylate interface, but for simplicity it is represented as a single hydrogen bond with atomic charges representative of the entire salt bridge interface.

Following the work described in the previous chapter, the adiabatic ground and excited states are taken as the first and second lowest-energy roots of the four-by-four secular equation within the basis defined by the four diabatic states

$$\begin{vmatrix} H_{0a,0a}-\varepsilon_g & H_{0b,0a}-\varepsilon_g S_{0b,0a} & H_{1a,0a}-\varepsilon_g S_{1a,0a} & H_{1b,0a}-\varepsilon_g S_{1b,0a} \\ H_{0a,0b}-\varepsilon_g S_{0a,0b} & H_{0b,0b}-\varepsilon_g & H_{1a,0b}-\varepsilon_g S_{1a,0b} & H_{1b,0b}-\varepsilon_g S_{1b,0b} \\ H_{0a,1a}-\varepsilon_g S_{0a,1a} & H_{0b,1a}-\varepsilon_g S_{0b,1a} & H_{1a,1a}-\varepsilon_g & H_{1b,1a}-\varepsilon_g S_{1b,1a} \\ H_{0a,1b}-\varepsilon_g S_{0a,1b} & H_{0b,1b}-\varepsilon_g S_{0b,1b} & H_{1a,1b}-\varepsilon_g S_{1a,1b} & H_{1b,1b}-\varepsilon_g \end{vmatrix} = \mathbf{0} \qquad (5)$$

where $H_{ij} = \left\langle \Psi_i^{BLKS} \middle| \hat{H} \middle| \Psi_j^{BLKS} \right\rangle$ and $S_{ij} = \left\langle \Psi_i^{BLKS} \middle| \Psi_j^{BLKS} \right\rangle$ are the BLKS Columbic and overlap integrals and ε_g is the lowest energy root (i.e. the adiabatic ground state energy). In addition, effective CPET and HAT diabatic states are constructed as linear combinations of the electron-localized diabatic states and the proton-localized diabatic states, respectively, where each set of effective diabatic states is a two-state representation of the four-state model of PCET

$$\Phi_R^{\mathrm{CPET}} = c_{0a}\Psi_{0a}^{\mathrm{BLKS}} + c_{0b}\Psi_{0b}^{\mathrm{BLKS}} \qquad (6)$$

$$\Phi_P^{\mathrm{CPET}} = c_{1a}\Psi_{1a}^{\mathrm{BLKS}} + c_{1b}\Psi_{1b}^{\mathrm{BLKS}} \qquad (7)$$

and

$$\Phi_R^{\mathrm{HAT}} = c'_{0a}\Psi_{0a}^{\mathrm{BLKS}} + c'_{1a}\Psi_{1a}^{\mathrm{BLKS}} \qquad (8)$$

$$\Phi_P^{\mathrm{HAT}} = c'_{0b}\Psi_{0b}^{\mathrm{BLKS}} + c'_{1b}\Psi_{1b}^{\mathrm{BLKS}} \qquad (9)$$

where the prime above the configuration interaction coefficients for the HAT reactant and product states indicates these are different values than those for the CPET reactant and product states. Using the electron-localized CPET basis, electronic coupling is defined as

$$V_{CPET} = \frac{|H_R S_{R,P} - H_{R,P}|}{1 + S_{R,P}} \tag{10}$$

where $H_{ij} = \left\langle \Phi_i^{CPET} \middle| \hat{H} \middle| \Phi_j^{CPET} \right\rangle$ and $S_{ij} = \left\langle \Phi_i^{CPET} \middle| \Phi_j^{CPET} \right\rangle$ are the BLKS Columbic and overlap integrals of effective diabatic states Φ_R^{CPET} and Φ_P^{CPET}.

5.4 Computational Details

Because care was taken to ensure that photo-excitation of the Ru(II) center results in localization of the excited electron on the salt-bridge substituted bipyridine ligand, it is reasonable to neglect the Ru(III) center and remaining bipyridine ligands in our computational model of DNOA.[20] The same assumption was made and validated in previous theoretical studies and it was found that the optimized structure of the model complex is planar.[33] Here, internal dihedral coordinates are used to constrain the system to be planar. Remaining internal coordinate were optimized using B3LYP/6-31+G(d) level of theory. The PT donor-acceptor distance is 2.68 Å in the optimized structure (Figure 5.2), compared to 2.696 Å computed by Hammes-Schiffer at the RHF/6-31G(p,d) level of theory. As in the previous chapter, diabatic PESs are computed by varying the transferring proton along a linear reaction coordinate, defined here as

$$\Delta R_p = R_{\mathrm{NH}}^{\mathrm{D}} - R_{\mathrm{HO}}^{\mathrm{A}} \tag{11}$$

where R_{NH}^{D} is the donor (D)-hydrogen bond distance (NH) and R_{HO}^{A} is the hydrogen-acceptor (A) bond distance (HO). The heavy atoms are held fixed in the optimized transition state structure for each single point energy calculation along the proton transfer reaction coordinate. All MSDFT calculations using the B3LYP functional and the 6-31G(d) basis set were performed with a locally modified version of GAMESS.[11,12]

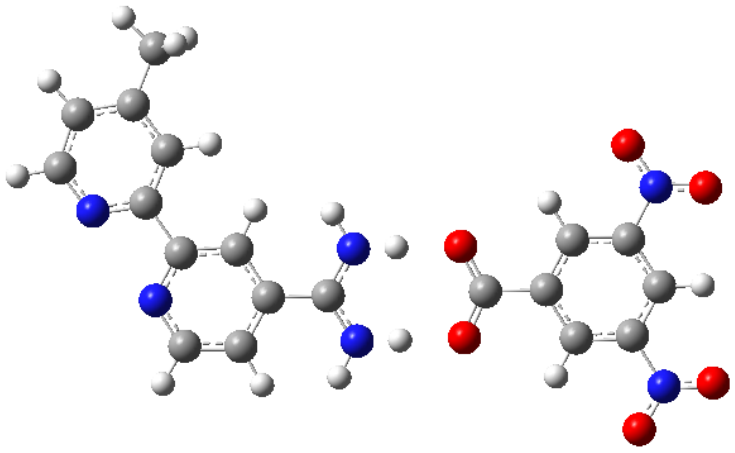

Figure 5.2 Optimized structure of the model system of Nocera's donor-amidinium-carboxylate-acceptor (DNOA) complex. Atom type are indicated by color (C – grey, N – blue, O – red, and H – white).

5.5 Results and Discussion

The one-dimensional PESs of the diabatic states 0*a*, 0*b*, 1*a*, and 1*b* are plotted against the proton transfer coordinate (ΔR_p) in Figure 5.3. Unlike the self-exchange reactions discussed in Chapter 4, where the driving force was zero, the overall reaction of DNOA is slightly endothermic. For reactant proton configurations ($\Delta R_p < 0.0$), diabatic states 0*a* and 1*a* are significantly lower in energy than states 0*b* and 1*b* due to the localization of the proton basis functions within the donor block in states 0*a* and 1*a*. On the product side of the proton transfer coordinate ($\Delta R_p > 0.0$), the opposite is true where states 0*b* and 1*b* more stable than states 0*a* and 1*a*. As expected, diabatic states 0*a* and 1*b*, which best represent the overall reaction, are localized on either side of the proton transfer coordinate. They intersect near $\Delta R_p = 0.05$ with an energy of 38 kcal/mol. The two higher-energy diabatic states, 1*a* and 0*b*, are also significantly localized within the reactant and product sides of the proton coordinate, respectively, with minima lower in

energy than the crossing point of diabatic states 0*a* and 1*b*. The significance of these low-lying diabatic states is discussed below.

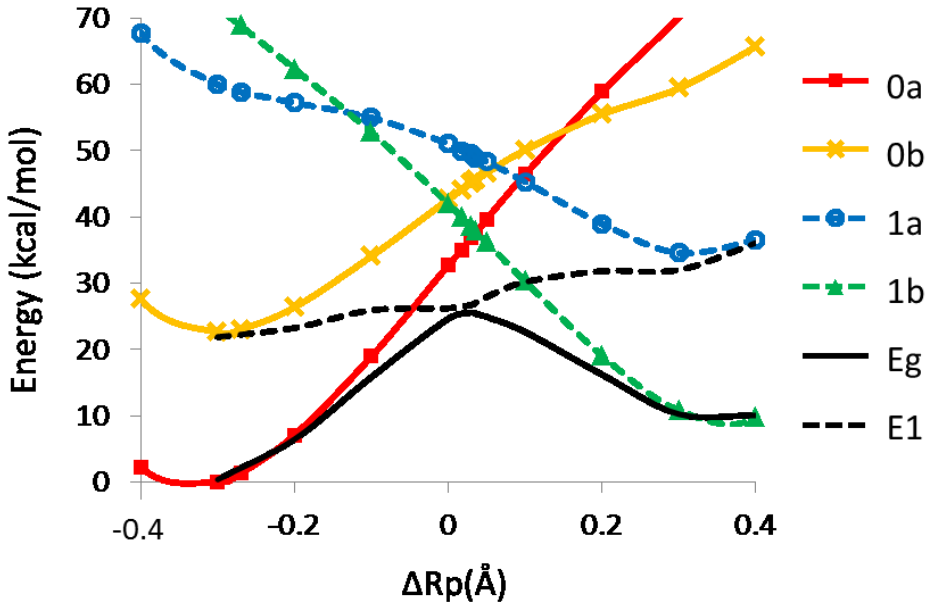

Figure 5.3 Diabatic and adiabatic state potential energy curves for DNOA.

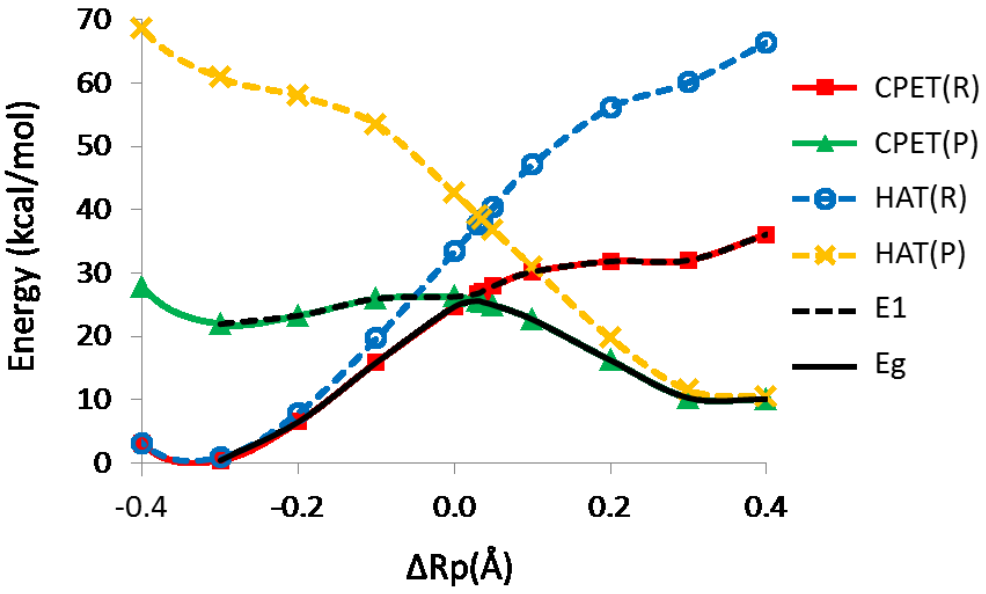

Figure 5.4 Electron-localized CPET effective diabatic states, proton-localized HAT effective diabatic states, and adiabatic state potential energy curves for DNOA.

The adiabatic ground and excited states and the electron-localized CPET effective diabatic state PESs are shown in Figure 5.4. The adiabatic PESs overlap the CPET PESs along nearly the entire proton coordinate, except for a very small range of proton positions near the diabatic state crossing point. At this proton position, the adiabatic energy gap is very small (~3.0 kcal/mol) characteristic of a conical intersection. Similar to Marcus theory of ET, the adiabatic ground and excited states are well characterized by a single electron-localized effective diabatic state, Φ_R^{CPET} or Φ_P^{CPET}, until the avoided crossing, at which point the adiabatic states abruptly switch electronic character. This implies that non-adiabatic transition through a conical intersection is a likely mechanism for this PCET reaction. These results are consistent with an electronically non-adiabatic process, as is expected given the physical separation of the electron donor and acceptor molecules.

The adiabatic PES obtained from MSDFT quantitatively reproduce gas-phase state-averaged complete active space self-consistent field (SA-CASSCF) results computed by Hammes-Schiffer.[33] This multireference wavefunction method is a good reference for validation of MSDFT for the study of PCET reactions because it accounts for static electron correlation inherent in systems with multiple electron configurations (i.e. multiple diabatic states, VB structures, configuration state functions, etc.). Shown in Figure 5.5, MSDFT reproduces the nearly 10 kcal/mol endothermicity of PCET in DNOA and its significant barrier (about 25 kcal/mol) at the adiabatic avoided crossing. Most importantly, MSDFT reproduces the extremely small adiabatic energy gap at this proton position, characteristic of an electronically non-adiabatic PCET mechanism.

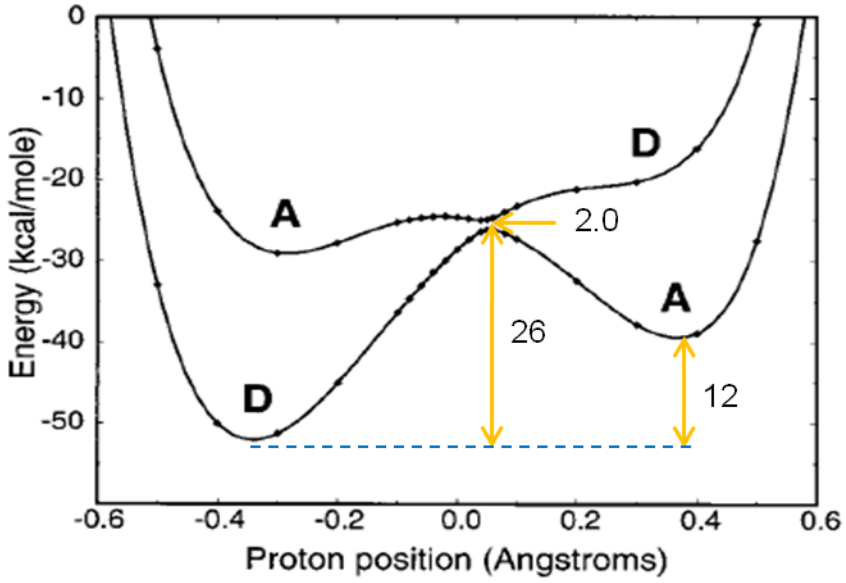

Figure 5.5 Gas phase energies of the active electronic adiabatic states as functions of the proton coordinate for DNOA. The labels D and A correspond to the active electron localized on the electron donor and acceptor, respectively. Reproduced with permission from Soudackov, A. and Hammes-Schiffer, S. *J. Am. Chem. Soc.* **1999** *121*, 10598-10607. Copywrite 1999 American Chemical Society.

Further insight of the underlying mechanistic properties of PCET in the DNOA system is gained by analysis of the diabatic states from which the adiabatic state is constructed. The low-lying diabatic states 0*b* and 1*a* contribute significantly to the adiabatic ground and excited states. Figure 5.6 gives the structural weight of each diabatic state along the proton transfer coordinate, which is a quantitative measure of the contribution a state has to the optimized adiabatic ground state. On the reactant side of the proton transfer coordinate ($\Delta R_p < 0.0$), the adiabatic ground state is well characterized by diabatic state 0*a* with increasing contribution from state 0*b*, until the diabatic state crossing point (i.e. adiabatic avoided crossing), at which point the contributions from these states drop to zero and are replaced by diabatic states 1*a* and 1*b*. Initially after the

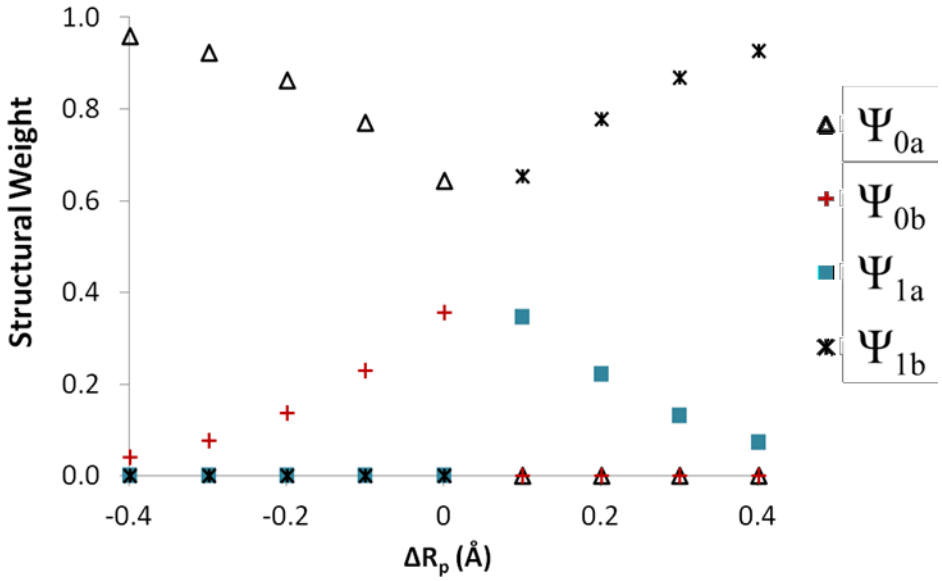

Figure 5.6 Structural weight of each diabatic state as a function of the proton transfer coordinate for DNOA.

avoided crossing, the adiabatic ground state has significant contribution from both states 1*a* and 1*b*, but as the reaction progresses along the proton transfer coordinate, diabatic state 1*b* becomes more dominant with less contribution from 1*a*. Ultimately, the adiabatic ground state is characterized by diabatic state 1*b* when the proton is in its product configuration.

A three-dimensional More O'Ferrall-Jencks plot illustrates the coupling between electron and proton transfer within the two-dimensional ET and PT tunneling space. Figure 5.7 shows both the ground and excited adiabatic PESs in three-dimensions. In addition, Figure 5.8 displays the ground state PES with the minimum energy path (MEP) shown for the ground state in blue and the excited state in red. These MEPs are in fact the

same adiabatic ground and excited state PESs shown in Figures 5.3 and 5.4 along the one-dimensional proton transfer coordinate. The difference being that the three-

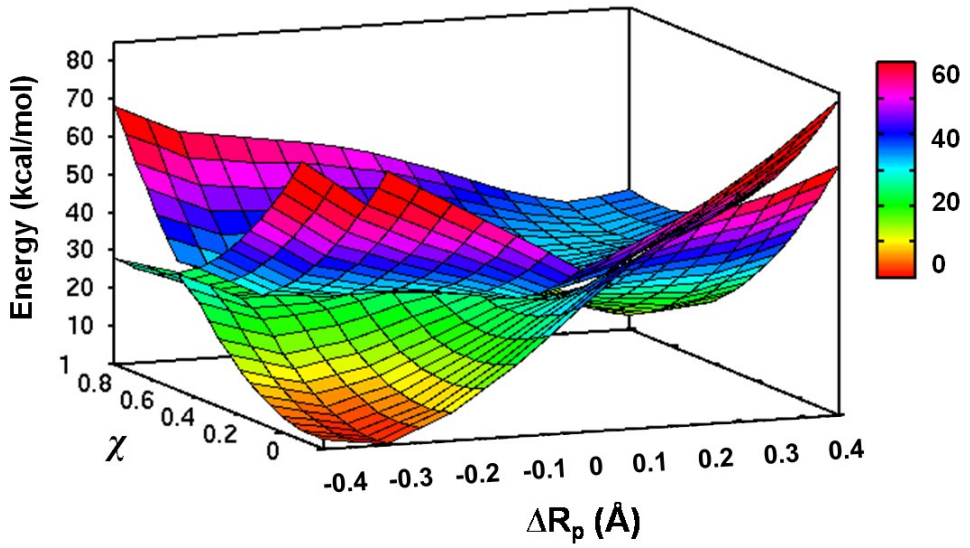

Figure 5.7 Three-dimensional More O'Ferrall-Jencks diagram of DNOA.

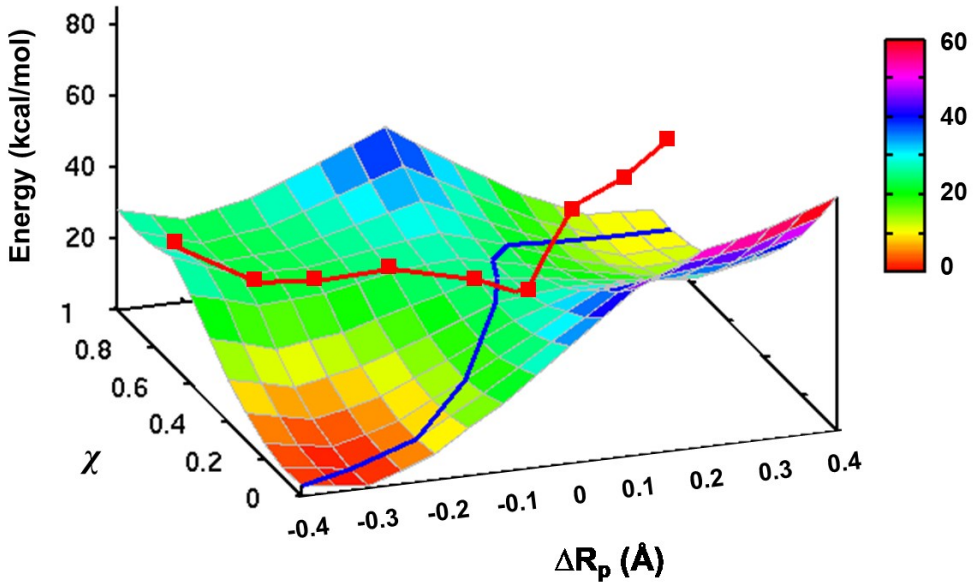

Figure 5.8 Three-dimensional adiabatic ground potential energy surface, adiabatic ground state MEP (solid blue line) and adiabatic excited MEP (red squares).

dimensional diagrams explicitly show the dependence of the adiabatic energy on both the ET and PT coordinates. A third representation of this data is shown in Figure 5.9, which

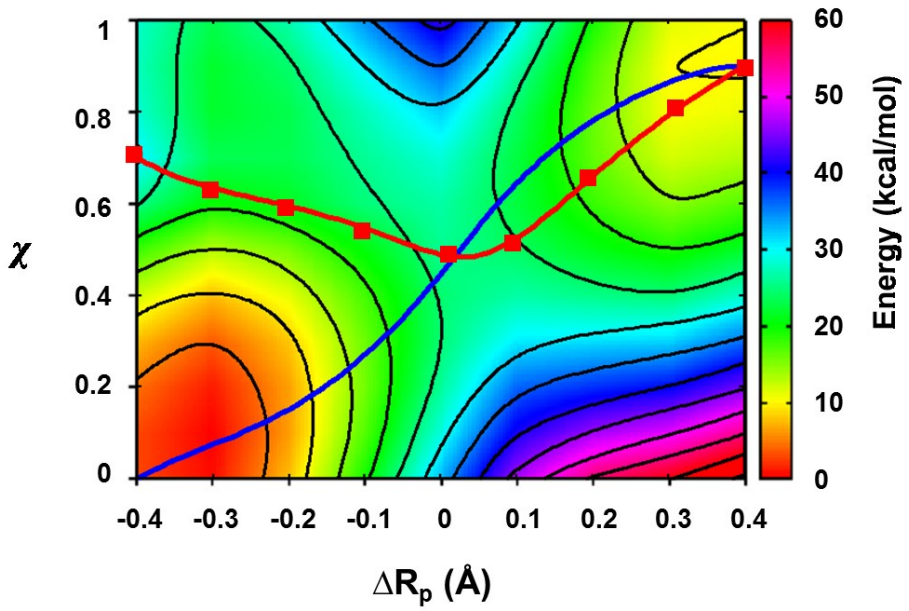

Figure 5.9 X-Y plane of three-dimensional More O'Ferrall-Jencks diagram for the adiabatic ground state of DNOA. Energy indicated by color gradient and black contour lines every 5 kcal/mol. Ground state MEP (blue solid line) and excited MEP (red squares) are also shown.

is the X-Y plane of the three-dimensional graph shown in Figure 5.7 with black contour lines marking every 5 kcal/mol, along with the same color gradient and MEPs shown in Figure 5.7. In Figure 5.8, it can be seen that the excited state MEP follows a ridge along the ground state PES from ΔR_p = -0.4 to -0.1 while the ground state MEP follows a diagonal pathway with a slightly stronger dependence on the PT coordinate. Near the avoided crossing (ΔR_p = 0.05), the ground state MEP passes smoothly over a ridge separating PT reactant and product states, during which it gains a stronger dependence on the ET coordinate. This only lasts for a small range of PT coordinates, however, and soon the ground state MEP reorients to follow a diagonal pathway to the final product state.

Meanwhile, the excited state MEP approaches the avoided crossing orthogonal to the ground state MEP, but at $\Delta R_p = 0.05$ it has an abrupt change in direction and follows a diagonal pathway to the product state, mirroring that of the ground state MEP. Analysis of the three-dimensional More O'Ferrall Jencks diagrams indicates a predominantly one-dimensional tunneling along the PT coordinate, remaining in the reactant electronic state, followed by an abrupt change in electronic character at the avoided crossing. At that point, the system becomes more strongly coupled between ET and PT and relaxes to the product state through a diagonal pathway within the two-dimensional tunneling space.

Considering the three-dimensional More O'Ferrall-Jencks diagrams of the self-exchange reactions discussed in the Chapter 4, it is clear that DNOA proceeds along a different mechanistic pathway than any of the previously discussed reactions. The phenol/phenoxyl radical is most similar to DNOA in that the ground and excited state MEPs are orthogonal near the avoided crossing. However, the ground state MEP of the phenol/phenoxyl radical has a stronger dependence on the ET coordinate and the excited state MEP follows a ridge parallel to the ET coordinate and ground state MEP. In contrast, DNOA demonstrates an electronically non-adiabatic, concerted PCET mechanism that is more strongly dependent on the position of the proton. This could explain the strong dependence of the experimental rate constant of Nocera's model system on the orientation of the salt-bridge interface. It is reasonable to assume that even before photo-excitation, the switched DONA interface already consists of a protonated electron acceptor molecule, thus the reaction is purely an ET mechanism and is not dependent on PT. It has been eluded to that this is the case and our results here support

this conclusion based on the strong dependence of the ground state MEP along the PT coordinate. In other words, this mechanism is akin to the "zig-zag" approach described by Cukier in that ET is dependent on the nuclei rearranging to the transition state for PT, at which point ET easily occurs and the system relaxes into the final product configuration.[10]

5.6 Conclusions

In this chapter, we demonstrated the accuracy of MSDFT in computing adiabatic ground and excited state PESs for an electronically non-adiabatic, concerted PCET mechanism in DNOA, a model system developed by Nocera in which the electron donor-acceptor pair is physically separated by an amidinium-carboxylate salt-bridge interface. Specifically, this expands the validation of MSDFT from our previous work on symmetric self-exchange reactions to an asymmetric system involving physically separated electron and proton donor-acceptor sites. Our results reproduce the thermodynamics of the adiabatic state as computed by high-level electronic structure theory calculations and demonstrates the inherent coupling of ET and PT in the DNOA complex. Furthermore, our analysis explicitly accounts for the low-lying excited adiabatic state based on the low-energy diabatic states 0*b* and 1*a* and their significant contribution to describing the adiabatic PES. Analysis of the three-dimensional More O'Ferrall-Jencks diagram of concerted PCET in the DNOA system presents a unique mechanism for electronically non-adiabatic PCET, different than that of the self-exchange reaction between phenol and phenoxyl radical discussed in the previous chapter.

Chapter 6. Hydrogen Atom Abstraction of Ascorbate by TEMPO Radical

Chapter 6.1 Introduction

Ascorbic acid (Vitamin C) plays a critical role in biology as a strong reducing agent and contributes to the "scavenging" of free radicals in the human body. It is generally accepted that ascorbate, the deprotonated form of ascorbic acid most prevalent at physiological pH, provides reducing equivalents, in the form of an electron, to monooxygenases within transport vesicles through a vesicle membrane protein cytochrome b_{561} (Figure 6.1).[3,120–123] It has been shown that ascorbate hydrogen bonds to a histidine residue in the active site of cytochrome b_{561}. The proposed mechanism consists of a proton-coupled electron transfer (PCET) in which ascorbate donates an electron to the iron center of cytochrome b_{561}, reducing it from Fe(III) to Fe(II), and provides a proton to the histidine residue (Figure 6.2).[3,124]

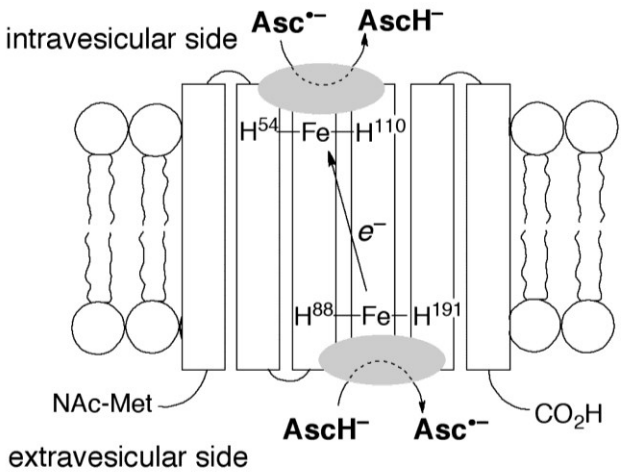

Figure 6.1 Proposed structural model for bovine cytochrome b_{561}, modified from Ref. 124, showing the ascorbate/ascorbyl radical conversions on both sides of the membrane. Fe = ion-heme and H = histidine. Reprinted with permission from Warren, J. J. and Mayer, J. M. *J. Am. Chem. Soc.* **2010**, *132*, 7784-7793. Copywrite 2010 American Chemical Society.

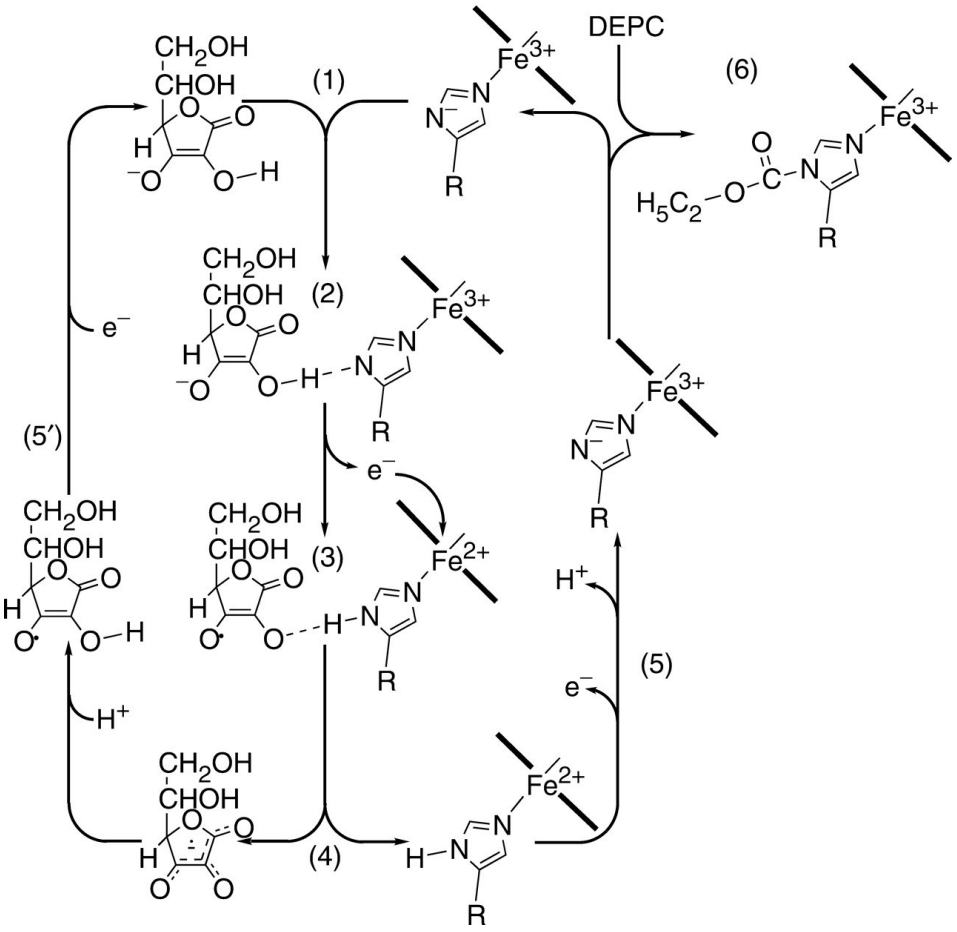

Figure 6.2 Postulated histidine cycle mechanism for the concerted PCET reaction from ascorbate to the cytosolic haeme b centre of cytochrome b_{561}. This scheme is based on the original model of Njus et al. with modifications by Nakanishi et al. Reprinted with permission from Nakanishi, N.; Takeuchi, F.; Tsubaki, M. *J. Biochem.* **2007**, *142*, 553-560. Copywrite 2007 Oxford University Press.

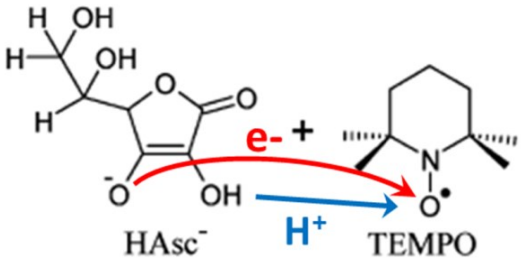

Figure 6.3 Electron and proton transfer for the hydrogen atom abstraction of ascorbic acid ($Hasc^-$) by TEMPO radical (2,2,6,6-tetramethyl-piperidin-1-oxyl).

Experimentally, the kinetic and thermodynamic properties of the oxidation of ascorbate have been studied using the 2,2,6,6-tetramethylpiperidine-1-oxyl (TEMPO) radical as the oxidizing agent and proton acceptor (Figure 6.3).[34,35,125] Interestingly, the hydrogen atom abstraction of ascorbate by the TEMPO radical does not follow the general trends in solvent kinetic effects (KSE) of phenol type substrates, as described by Ingold.[9] It has been proposed that the hydrogen bond donating and/or accepting ability of a solvent explains the unusual KSE of ascorbate.[34,35] Here, we summarize the experimental findings and the theoretical interpretations of experimental data for the ascorbate/TEMPO radical hydrogen atom abstraction, describe our investigation of this reaction using MSDFT, draw parallels of previous findings with our analysis, and highlight the additional insights provided by MSDFT.

6.2 Background Information

6.2.1 Experimental Thermodynamics

Because of its essential role in biology as a reducing agent, the redox chemistry of ascorbic acid has been extensively studied. Experimental pK_a values and redox potentials provide relative free energies of sequential electron and proton loss (Figure 6.4).[48] At physiological pH, ascorbic acid is most prevalent in its deprotonated anionic form, ascorbate ($AscH^-$). Typically, ascorbate is thought of only in terms of its reducing ability, that is the loss of a single electron, but oxidation of ascorbate forms a high-energy neutral radical species that easily gives up a proton to form the stable ascorbyl radical ($Asc^{\bullet-}$). In fact, the "scavenging ability" of ascorbate is generally attributed to the resonance stabilization of this anionic radical species. Alternatively, ascorbate may be deprotonated

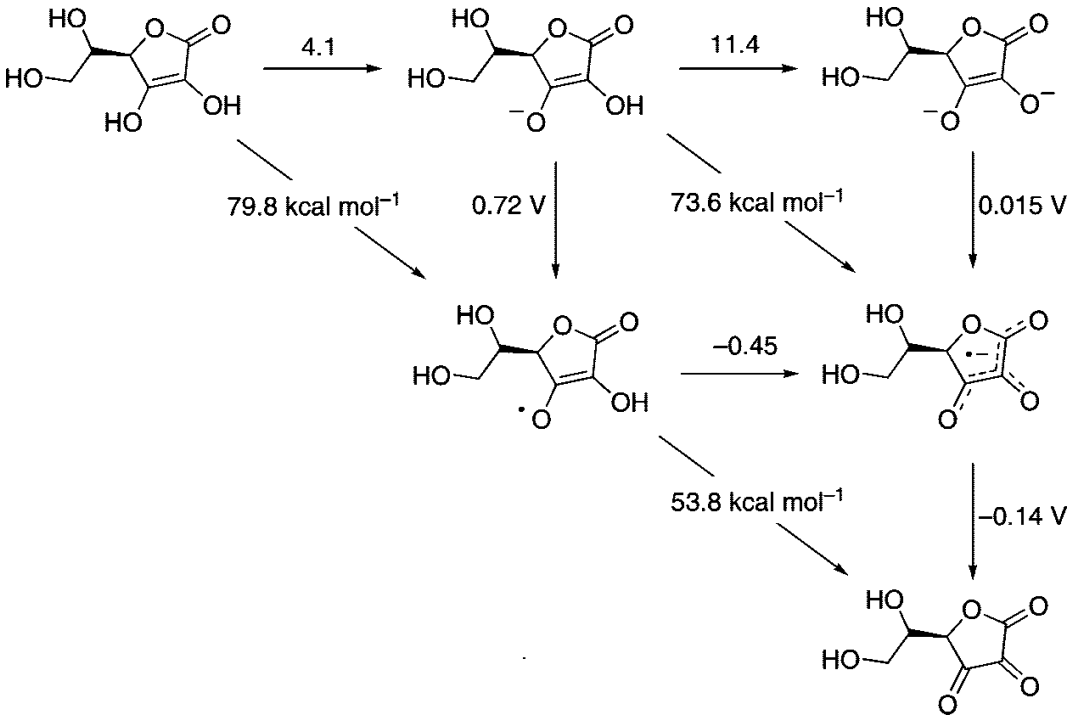

Figure 6.4 Thermodynamic "square scheme" for ascorbic acid. Horizontal arrows indicate proton loss and give the corresponding pK_a. Vertical arrows give the one-electron reduction potential. Diagonal arrows indicate relative bond free energies for the corresponding one-electron/one-proton loss of a formal hydrogen atom transfer. Reprinted with permission from Warren, J. J.; Tronic, T. A.; Mayer, J. M. *Chem. Rev.* **2010***, 110*, 6961-7001. Copywrite 2010 by American Chemical Society.

to form a di-anion (Asc^{2-}) and then oxidized, but with a pK_a of 11.4 the initial PT step is thermodynamically unfavorable at physiological pH and the subsequent ET is not favorable enough to compensate. Thus, the oxidation of ascorbate to the ascorbyl radical is thought to be a concerted PCET process.

6.2.2 Proposed Mechanism

Based on the work of Mayer,[12] Hammes-Schiffer,[13] Truhlar,[14] and the validation studies discussed in Chapter 4, it is reasonable to expect the hydrogen atom abstraction of ascorbate to be electronically non-adiabatic, similar to the self-exchange reaction of phenol/phenoxyl radical. Both systems involve proton transfer between hydrogen-bonded

oxygen atoms and provide stabilization of charge and unpaired spin density through conjugated systems. Previous computational work indicates that delocalization of the lone electron on the phenoxyl radical occurs across the conjugated benzene ring.[12] This stabilizes a transition state between phenoxyl and phenol such that an electron is transferred between *p*-type orbitals perpendicular to the benzene ring molecular plane. This is in contrast to the self-exchange reaction of methanol/methoxyl radical, which proceeds through a typical HAT transition state where the electron is transferred between the same set of orbitals as the transferring proton, along the proton transfer coordinate.[12] Despite the fact that electron transfer occurs between two hydrogen bonded oxygen atoms, the methanol/methoxyl radical self-exchange reaction is deemed electronically adiabatic. Thus, it is concluded that stabilization of the orthogonal PCET transition state originates from the delocalization of charge and unpaired spin density across the conjugated benzene ring of phenol/phenoxyl radical system.

Comparing this analysis to the ascorbate/TEMPO radical system, it is expected that an electron is transferred from a *p*-type orbital of ascorbate perpendicular to the molecular plane due to its ability to stabilize charge and unpaired spin through its conjugated molecular ring.[126] However, the TEMPO radical does not offer the same degree of delocalization. Resonance between the singly-occupied *p*-orbital of the TEMPO oxygen atom and the doubly-occupied lone pair *p* orbital on nitrogen offers some delocalization of the unpaired spin across the oxygen-nitrogen bond, but not to the extent of a conjugated benzene ring of phenol.

Here, we present our MSDFT analysis of the ascorbate/TEMPO radical hydrogen atom abstraction in efforts to classify the concerted PCET mechanism. Analysis of the system's block-localized Kohn-Sham orbitals and corresponding atomic charges and unpaired spin density will connect this reaction to previous computational work and provide insight into the physical characteristics governing the concerted PCET mechanism. To our knowledge, computational analysis of the diabatic states, electronic non-adiabaticity, and electronic structure of the hydrogen atom abstraction of ascorbate by the TEMPO radical has yet to be reported prior to publication of this thesis.

6.3 Methodology

Following the method described in Chapter 3, MSDFT is used to model the four charge-localized diabatic states involved in hydrogen atom abstraction of ascorbate by the TEMPO radical. Figure 6.5 depicts a two-dimensional More O'Ferrall-Jencks

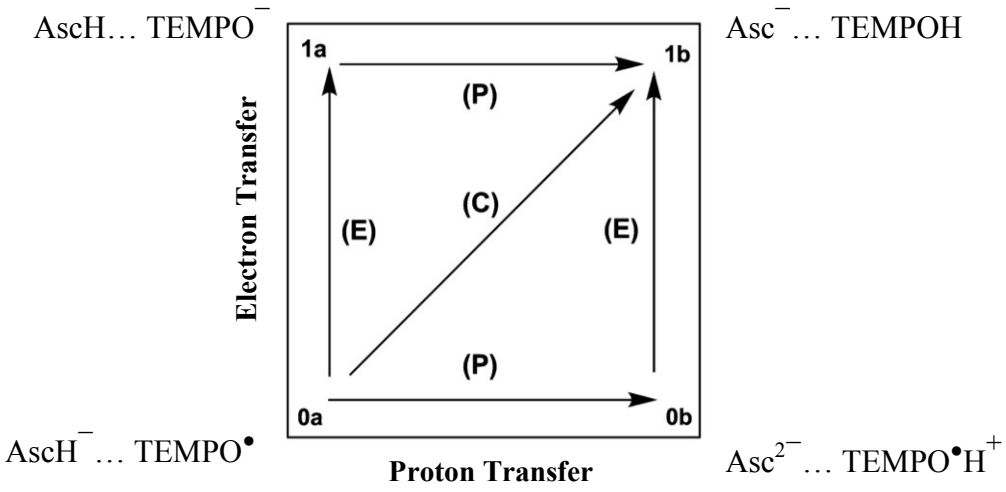

Figure 6.5 More O'Ferrall - Jencks diagram for PCET, where 0 and 1 (*a* and *b*) indicate localization of the electron (proton) on donor and acceptor sites, respectively, of ascorbate and the TEMPO radical.

diagram representing the two-dimensional tunneling space of electron transfer (ET) and proton transfer (PT). Valence bond (VB) structures represent the four diabatic states in the four corners of the diagram. Here, *0* and *1* indicate localization of the transferring electron on the ET donor and acceptor sites, respectively, while *a* and *b* indicate localization of the proton on the PT donor and acceptor sites. Based on these VB structures, block-localized Kohn-Sham (BLKS) functions are defined as

$$\mathrm{D_e^- - OH}\ \cdots^{\bullet}\mathrm{O - A_e};\ \ \Psi_{0a}^{\mathrm{BLKS}} = \hat{\mathrm{A}}\{\Omega_{0a}^{1}(\mathrm{D_e^- - OH})\Omega_{0a}^{2}(^{\bullet}\mathrm{O - A_e})\} \tag{1}$$

$$\mathrm{D_e^- - O^-}\cdots^{+}\mathrm{H^{\bullet}O - A_e};\ \Psi_{0b}^{\mathrm{BLKS}} = \hat{\mathrm{A}}\{\Omega_{0b}^{1}(\mathrm{D_e^- - O^-})\Omega_{0b}^{2}(^{+}\mathrm{H^{\bullet}O - A_e})\} \tag{2}$$

$$\mathrm{D_e^{\bullet} - OH}\cdots^{-}\mathrm{O - A_e};\quad \Psi_{1a}^{\mathrm{BLKS}} = \hat{\mathrm{A}}\{\Omega_{1a}^{1}(\mathrm{D_e^{\bullet} - OH})\Omega_{1a}^{2}(^{-}\mathrm{O - A_e})\} \tag{3}$$

$$\mathrm{D_e^{\bullet} - O^-}\cdots\mathrm{HO - A_e};\quad \Psi_{1b}^{\mathrm{BLKS}} = \hat{\mathrm{A}}\{\Omega_{1b}^{1}(\mathrm{D_e^{\bullet} - O^-})\Omega_{1b}^{2}(\mathrm{HO - A_e})\} \tag{4}$$

where D_e and A_e represent the ascorbate and TEMPO molecules, respectively, and the proton donor and acceptor oxygen atoms are written explicitly. A key benefit of this method is that the delocalization of electron density within the ascorbate molecule is explicitly modeled by the orthogonality constraint enforced on all KS orbitals within a given block. Figure 6.6 depicts the block-localization of Kohn-Sham orbitals within the ascorbate/TEMPO radical model system. BLKS orbitals within the donor block (i.e. ascorbate) are optimized to be orthogonal to one-another, giving rise to delocalization across the ascorbate molecule. Meanwhile BLKS orbitals between the donor and acceptor (i.e. TEMPO) blocks are non-orthogonal, which retains the charge-localized nature of the diabatic states. The latter are represented here by the VB structures depicted in Figure 6.5 and eqs 1 – 4.

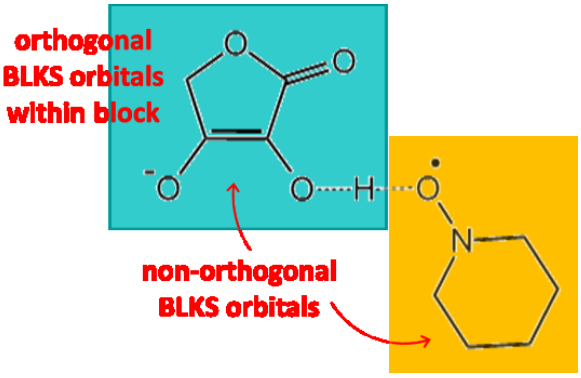

Figure 6.6 Schematic drawing of MSDFT donor (green) and acceptor (yellow) blocks for the model system of ascorbate/TEMPO radical in diabatic state 0*a* where the transferring electron and proton are both assigned to the donor block.

Furthermore, the full range of PCET mechanisms, from stepwise ET/PT and PT/ET to concerted PCET and within the entire continuum of concerted mechanisms, is characterized by the degree of coupling among these BLKS functions. As mentioned above, the thermodynamics of the stepwise mechanism, indicated in Figure 6.5 along the sides of the diagram, are highly unfavorable for ascorbate/TEMPO, thus are not expected to play a significant role in this PCET mechanism. The expected pathway is within the interior of the More O'Ferrall Jencks diagram, that is, a concerted PCET mechanism. As demonstrated by validation studies in Chapter 4, the MSDFT method accurately models the degree of electronic adiabaticity that distinguishes concerted PCET mechanisms and provides insight into the origin of the electronic coupling.

6.4 Computational Details

Previous computational studies justify the use of a truncated model for ascorbate where the dihydroxyethyl tail is replaced by a hydrogen atom, namely, α-hydroxytetronic

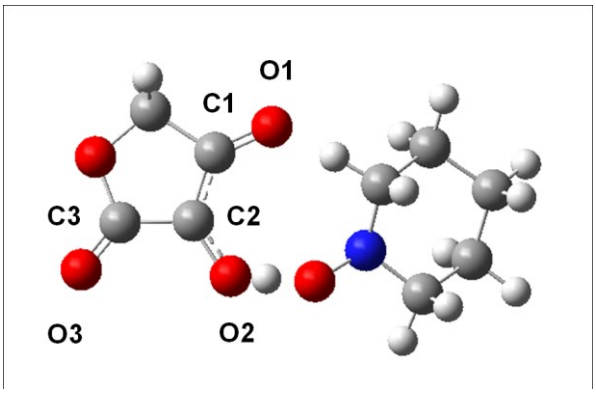

Figure 6.7 Gas phase optimized structure for the model system of ascorbate and the TEMPO radical, using M062X/6-31+G(d). Atom numbering indicated for ascorbate molecule.

acid. Comparison to experimental data confirms that α-hydroxytetronic acid retains important physical characteristics of ascorbate, including bond distances and isotropic hyperfine couplings.[126,127] The latter are directly proportional to α-β spin density, which is especially critical for modeling ascorbate as its radical scavenging ability is generally attributed to its ability to delocalize unpaired spin density, thus stabilizing the ascorbyl radical.[128] Gas phase computations on the full ascorbate structure indicate an internal hydrogen bond is formed between the dihydroxthyl tail of ascorbate and O3 (see Figure 6.7 for atom numbering). However, molecular dynamics simulations showed that the internal hydrogen bond is likely to dissociate quickly upon solvation and does not significantly affect the geometry of the ascorbate ring.[127]

Using α-hydroxytetronic acid as a model of ascorbate, the transition state structure of the hydrogen-bonded ascorbate/TEMPO complex was optimized in the gas phase using M06-2X/6-31+G(d) as implemented in Gaussian 09 (Figure 6.7). Frequency calculations at the same level of theory revealed a single imaginary frequency corresponding to the stretching mode along the linear proton transfer coordinate between

O2 of ascorbate and the oxygen of TEMPO. Bond distances, Mullikan population charges, and spin densities are in agreement with previous computational studies of ascorbate.[126]

A locally modified GAMESS[112,129] code was used to carry out MSDFT calculations at the PBE0/6-31G(d) level of theory. The transition state geometry was held fixed and the transferring hydrogen was moved linearly along the proton transfer reaction coordinate, defined as the difference in the distance between the transferring hydrogen and the donor (D) oxygen and that of the acceptor (A) oxygen: $\Delta R_p = R_p(D) - R_p(A)$. This follows from the fact that proton and electron transfers are significantly faster than heavy atom motions as in the Marcus theory of electron transfer.

6.5 Results and Discussion

6.5.1 MSDFT Potential Energy Surfaces

Based on the optimized transition state structure, MSDFT was used to plot one-dimensional potential energy surfaces (PES) of the four diabatic states (eqs 1 – 4), assuming a linear proton transfer coordinate between oxygen atoms (Figure 6.8). Similar to the asymmetric DNOA system, the overall reaction has a non-zero driving force, but in this case is exothermic. As before, diabatic states 0*a* and 1*b* are localized within the reactant and product sides of the PT coordinate, respectively. These diabatic states cross at $\Delta R_p = -0.09$ with an energy about 20 kcal/mol above the reactant state (diabatic state 0a at $\Delta R_p = -0.30$). Surprisingly, the two higher-energy diabatic states 0*b* and 1*a* do not cross along the PT coordinate. Diabatic state 0*b* remains highest in energy throughout the proton transfer coordinate, even within the product region ($\Delta R_p > 0.0$) where the proton is

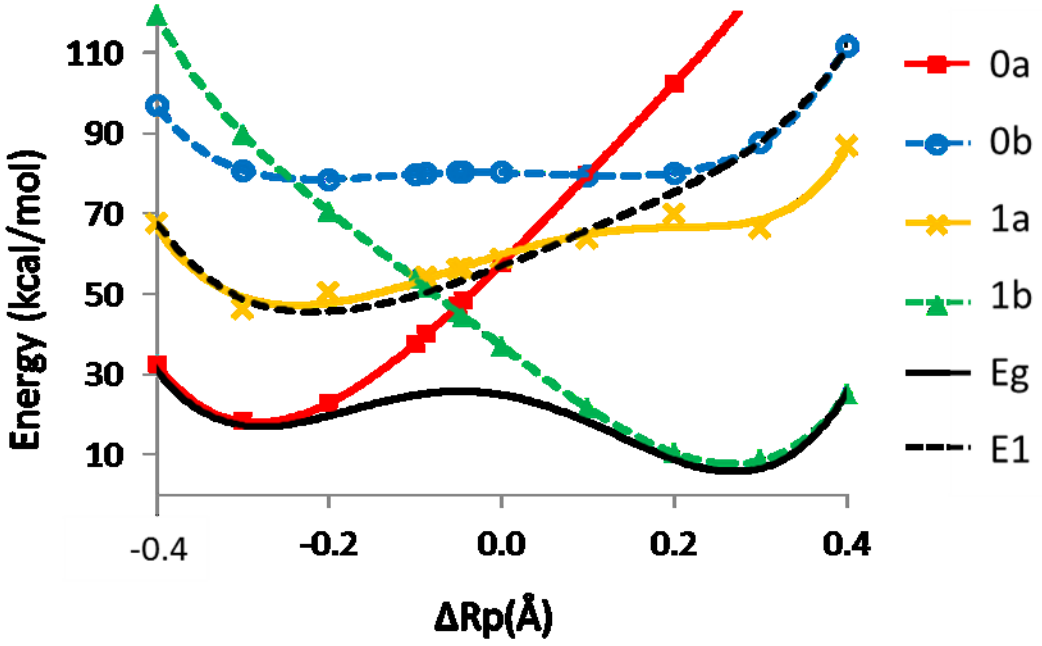

Figure 6.8 Diabatic and adiabatic state potential energy curves for the model system of ascorbate/TEMPO radical.

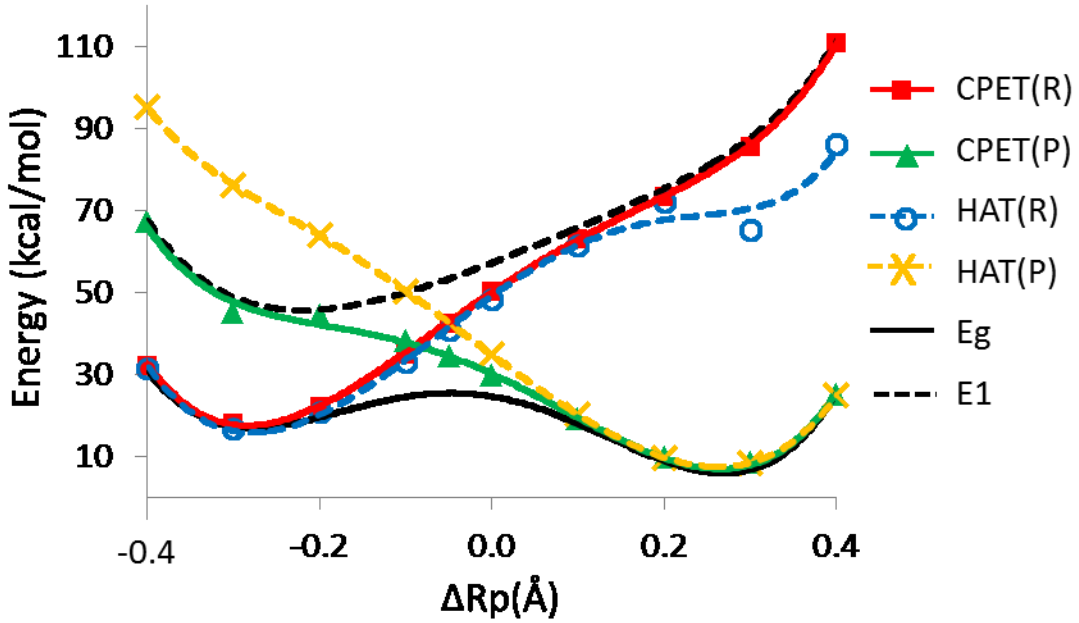

Figure 6.9 Effective diabatic and the adiabatic state potential energy curves for the model system of ascorbate/TEMPO radical.

physically near the TEMPO oxygen atom in the acceptor block. On the other hand, diabatic state 1*a* behaves as expected with a lower energy on the reactant side of the PT reaction coordinate ($\Delta R_p < 0.0$).

Coupling of all four diabatic states, 0*a*, 0*b*, 1*a*, and 1*b* through configuration interaction, provides the adiabatic ground and excited state PES (Figure 6.8). Unlike the adiabatic states of the isoelectronic hydrogen-exchange reactions discussed in Chapter 4 and the DNOA complex discussed in Chapter 5, the excited state of ascorbate/TEMPO radical is localized on the reactant side of the proton transfer coordinate. The origin of this asymmetry can be attributed to the high-energy of diabatic state 0*b*. The ground state adiabatic maximum occurs near $\Delta R_p = -0.05$ with a reaction barrier of 9.5 kcal/mol and an excited-ground state energy gap of 26 kcal/mol.

6.5.2 MSDFT Classification of Ascorbate/TEMPO Radical PCET Mechanism

As mentioned above, it is reasonable to predict ascorbate/TEMPO will behave similarly to the self-exchange reaction of phenol/phenoxyl, which is an electronically non-adiabatic concerted PCET mechanism. Here, we investigate the nature of this reaction in an effort to classify it within the regime of concerted PCET mechanisms.

First we consider the two-state representation of electron-localized CPET reactant and product states, defined as

$$\Phi_R^{CPET} = c_{0a}\Psi_{0a}^{BLKS} + c_{0b}\Psi_{0b}^{BLKS} \quad (8)$$

$$\Phi_P^{CPET} = c_{1a}\Psi_{1a}^{BLKS} + c_{1b}\Psi_{1b}^{BLKS} \quad (9)$$

where c_γ ($\gamma = 0a$, $0b$, $1a$, and $1b$) is a configuration interaction coefficient optimized for each effective diabatic state Φ_R^{CPET} and Φ_P^{CPET}. As shown in Figure 6.9, coupling of these

effective diabatic states reproduces the adiabatic PES. The same cannot be said of the proton-localized HAT states. Specifically, the HAT product state is higher in energy than the adiabatic excited state in the reactant region of the PT reaction coordinate, thus, coupling of the reactant and product HAT states will give a PES higher in energy than the adiabatic excited state within this region. In addition the crossing point of the CPET states is lower in energy than that of HAT. Based on this diagnostic test, MSDFT analysis identifies the hydrogen atom abstraction of ascorbate by the TEMPO radical as an electronically non-adiabatic process.

However, the relatively large adiabatic energy gap indicates a mechanism different from that of the phenol/phenoxyl radical self-exchange reaction. Similar trends were found for the MSDFT-computed electronic coupling constant, defined as

$$V_{R,P} = \frac{\left| H_{R,P}^{CPET} - \varepsilon_g S_{R,P}^{CPET} \right|}{1 + S_{R,P}^{CPET}} \tag{10}$$

where ε_g is the adiabatic ground state energy, $H_{R,P}^{CPET} = \left\langle \Phi_R^{CPET} \middle| H \middle| \Phi_P^{CPET} \right\rangle$ is the off-diagonal Hamiltonian matrix element and $S_{R,P}^{CPET} = \left\langle \Phi_R^{CPET} \middle| \Phi_P^{CPET} \right\rangle$ is the overlap matrix element in the two-state basis of the reactant and product electron-localized effective diabatic states, Φ_R^{CPET} and Φ_P^{CPET}. Table 6.1 summarizes the electronic coupling, adiabatic energy gap (ΔE_{adia}), and mechanistic classification (if any) for PCET reactions discussed in this work. Based on this data, the ascorbate/TEMPO radical hydrogen atom abstraction is best classified as a concerted PCET mechanism with intermediate electronic adiabaticity between that of the phenol/phenoxyl radical and the toluene/benzyl radical self-exchange reactions, similar to the aniline/aniline radical system.

Tabel 6.1 Electronic coupling constants, adiabatic energy gap, and classification of PCET mechanism.

	V_{el} (kcal/mol)			
	MSDFT PBE0 6-31G(d)	**CASSCF** (3,6) 6-31G	ΔE_{adia} (kcal/mol)	**Mechanism**
Benzyl/Tolune	23	41	128	HAT
Aniline radical/Aniline	10	n/a	20	Intermediate
Phenoxy/Phenol	1.5	2.0	3.0	CPET
Ascorbate/TEMPO$^{\bullet}$	11	n/a	26	CPET
$Ru^{III}(tmbyp)_3$/Dinitrobenzoate	0.0	0.5	1.2	CPET

The three-dimensional More O'Ferrall-Jencks diagram indicates a ridge along the ground state PES separating the PT reactant and product states (Figure 6.10). It does not, however, indicate a conical intersection seam due to the relatively large adiabatic energy gap along the ground state PES ridge. The ground state minimum energy path smoothly traverses the ridge from reactants to products, while the excited state minimum energy path is relatively collinear with the ground state path (Figure 6.11). In particular, the ground and excited pathways are only slightly orthogonal at the transition state proton position.

Lastly, we consider the structural weights of the four diabatic states as a measure of their respective contributions to the overall adiabatic ground state (Figure 6.12). As expected, the high-energy diabatic state 0*b* contributes very little along the entire PT reaction coordinate. The reaction is dominated by diabatic state 0*a* before the adiabatic maximum (ΔR_p = -0.05) and smoothly transitions to the 1*b* diabatic state. Despite the

relatively low energy of diabatic state 1*a* before the adiabatic maximum, it contributes relatively little to the adiabatic ground state.

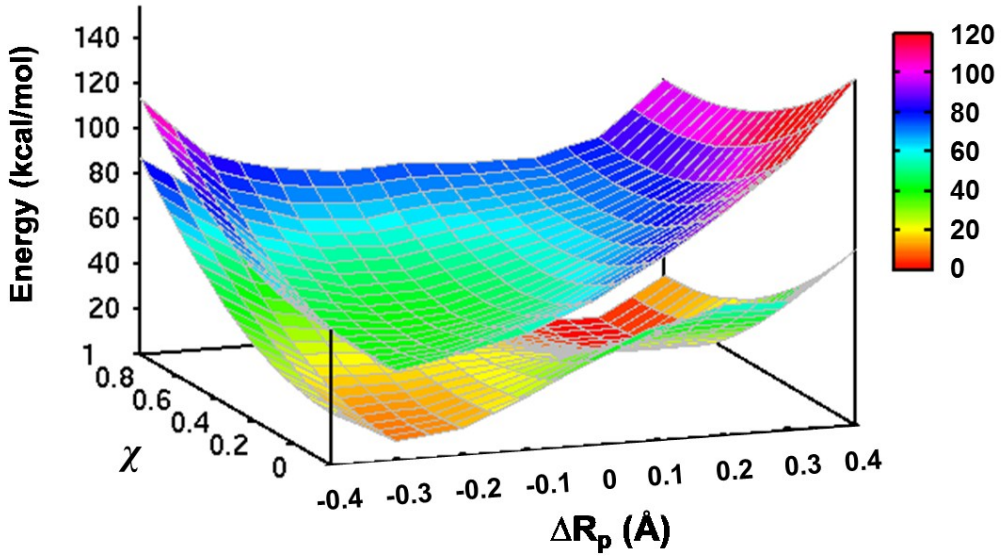

Figure 6.10 Three-dimensional More O'Ferrall-Jencks diagram for ascorbate/TEMPO radical model system.

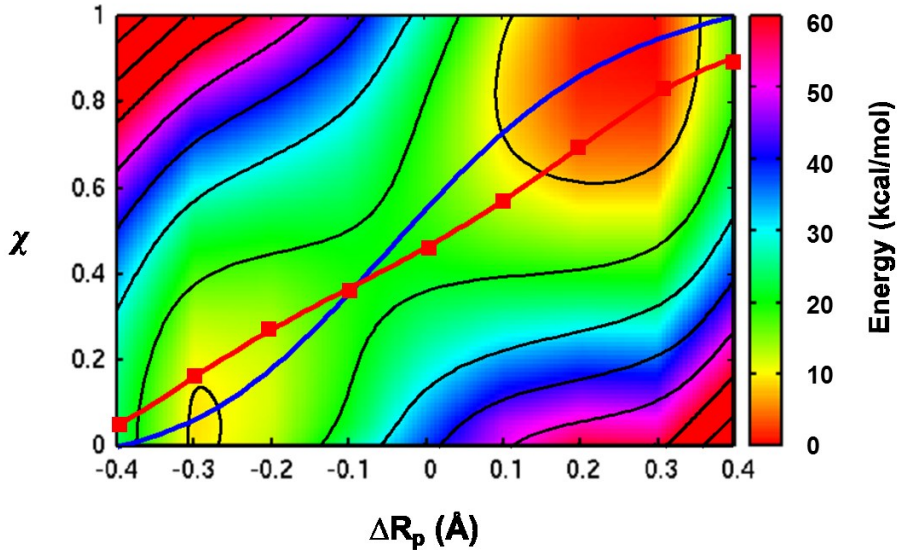

Figure 6.11 X-Y plane of three-dimensional More O'Ferrall-Jencks diagram for the adiabatic ground state of ascorbate/TEMPO radical model system. Energy indicated by color gradient and black contour lines every 10 kcal/mol. Ground state MEP (blue solid line) and excited MEP (red squres) are also shown.

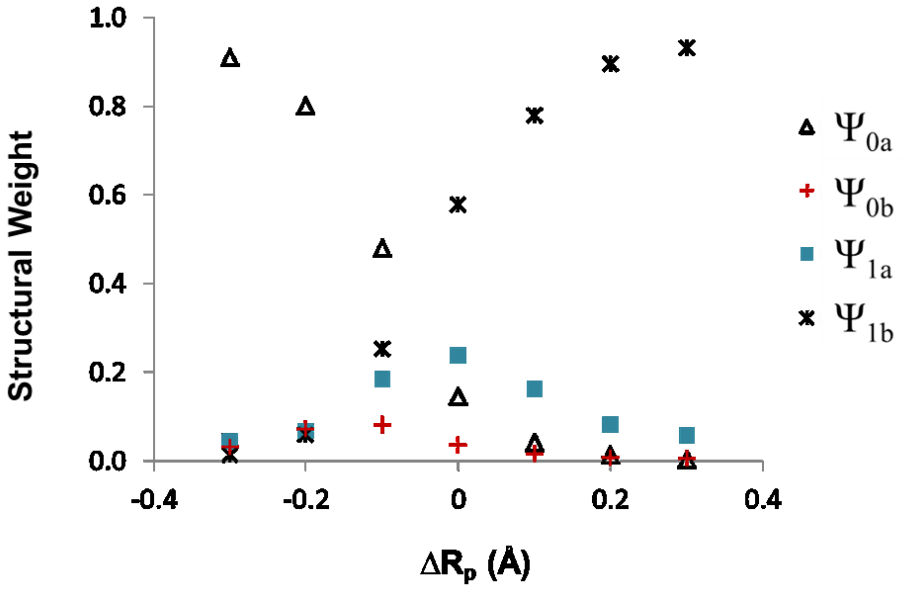

Figure 6.12 Structural weight of each diabatic state as a function of the proton transfer coordinate for the ascorbate/TEMPO radical model system.

6.5.3 Physical Properties of Ascorbate/TEMPO Hydrogen Atom Abstraction

Given the results above supporting a CPET mechanism with relatively large electronic adiabaticity, further analysis was carried out to elucidate the physical properties that govern this reaction. Specifically, the MSDFT optimized BLKS orbitals and atomic charges of each diabatic state were studied. For comparison, Gaussian09 was used to compute these same properties using traditional, delocalized DFT formalism.

It has been well-documented in this work that diabatic state 0*b* is energetically unfavorable throughout the proton transfer coordinate, giving rise to an unusually large separation between adiabatic ground and excited states on the product side of the PT coordinate. Based on its VB structure (D_e^- -O^-…$^{+\bullet}$HO-A_e), this state has the largest degree of charge separation of the four diabatic states. It is proposed that this unfavorable

Tabel 6.2 Löwdin atomic charges for the ascorbate/TEMPO radical model complex.

Atom	Diabatic State	Reactant	Diabatic Cross.	Adia. TS	Product	max$\Delta^{(a)}$
O2	0*a*	- 0.54	- 0.58	- 0.59	- 0.73	0.19
	0*b*	- 0.73	- 0.77	- 0.77	- 0.76	0.04
	1*a*	- 0.42	- 0.46	- 0.46	- 0.48	0.06
	1*b*	- 0.56	- 0.54	- 0.54	- 0.46	0.10
H	0*a*	+ 0.45	+ 0.53	+ 0.54	+ 0.63	0.18
	0*b*	+ 0.64	+ 0.67	+ 0.66	+ 0.51	0.16
	1*a*	+ 0.50	+ 0.60	+ 0.62	+ 0.64	0.14
	1*b*	+ 0.63	+ 0.61	+ 0.60	+ 0.46	0.14
O_{TEMPO}	0*a*	- 0.37	- 0.43	- 0.44	- 0.52	0.15
	0*b*	- 0.40	- 0.44	- 0.44	- 0.39	0.05
	1*a*	- 0.72	- 0.76	- 0.76	- 0.69	0.07
	1*b*	- 0.70	- 0.72	- 0.61	- 0.51	0.21
N	0*a*	- 0.10	- 0.06	- 0.05	+ 0.04	0.14
	0*b*	- 0.07	0.00	0.00	+ 0.07	0.14
	1*a*	- 0.30	- 0.30	- 0.30	- 0.29	0.01
	1*b*	- 0.30	- 0.29	- 0.29	- 0.29	0.01

(a) maxΔ indicates the largest change in magnitude of the atomic charge for a given diabatic state along the PT coordinate.

electronic structure is the origin of the high energy of state 0*b*, even when the proton position is physically near the acceptor site (i.e. positive ΔR_p values). Table 6.2 lists Löwdin atomic charges for each diabatic state at the reactant (ΔR_p = - 0.3), diabatic crossing point (ΔR_p = - 0.09), adiabatic transition state (TS) (ΔR_p = - 0.05), and product (ΔR_p = 0.3) proton position of the ascorbate/TEMPO complex.

Overall, the magnitude of an atomic charge for a given diabatic state varies by 0.2 a.u. or fewer along the proton transfer coordinate. Compared to analysis done by Hammes-Schiffer on the phenol/phenoxyl radical and toluene/benzyl radical,[13] there is relatively small charge redistribution along the proton transfer coordinate, consistent with an electronically adiabatic HAT process similar to the toluene/benzyl radical system. However, the *change* and *magnitude* of the proton being transferred (+0.45 to +0.67), the ascorbate O2 oxygen (-0.42 to -0.77), and the TEMPO oxygen (-0.37 to -0.76) atomic charges indicate significant charge separation along the proton transfer coordinate. This is more consistent with an electronically non-adiabatic process as in the reaction between phenol and phenoxyl radical. Furthermore, the largest change occurs between the adiabatic maximum and the product proton positions, supporting the conclusion that charge separation is the underlying physical property determining the unfavorable electronic configuration of state 0*b*.

The charges in Table 6.2 are computed using the BLKS determinants (i.e. diabatic states 0*a*, 0*b*, 1*a*, 1*b*). To ensure that the atomic charges were not an artifact of the block-localization of the electron density, we also obtained the Löwdin charges using traditional, delocalized KS determinants. While the proton and ascorbate O2 charges are consistent with those computed using BLKS determinants (+0.57 and -0.67, respectively), the TEMPO radical oxygen has almost half the magnitude of negative charge (-0.23) when computed using delocalized DFT. Although we do not have a good explanation for the 0.2 difference in the magnitude of the TEMPO radical oxygen at the transition state, the hydrogen and ascorbate O2 charges are of similar magnitude of the

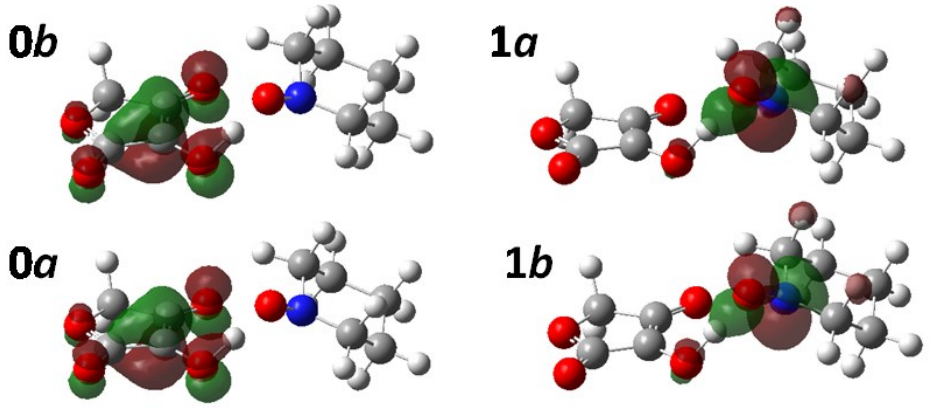

Figure 6.13 Singly-occupied molecular orbitals (SOMO) at the transition state structure of the CPET reaction between the ascorbate model compound and TEMPO radical. (isovalue = 0.002)

transferring proton and carboxylate oxygen acceptor site in Nocera's DNOA complex, which vary depending on the diabatic state from +0.35 to +0.53 and from -0.43 to -0.50, respectively. The smaller negative charge on the carboxylate oxygen is consistent with the more delocalized electron density across the carboxylate moiety compared to the O-N bond of TEMPO. Given the relatively small change along the proton transfer coordinate, but the large magnitude of charge, the ascorbate/TEMPO radical system experiences little charge redistribution, but maintains significant charge separation.

Analysis of the BLKS orbitals indicates that the singly occupied molecular orbitals (SOMO) of states 0*a* and 0*b* are π orbitals with anti-bonding character between the oxygen atoms and C=C double bonds. They are localized on ascorbic acid and perpendicular to its molecular plane. On the other hand, the SOMO of states 1*a* and 1*b* are π orbitals localized on TEMPO perpendicular to the oxygen-nitrogen bond (Figure 6.13). Although arguments based on orbital symmetry break down for asymmetric

reactions,[14] the BLKS orbitals suggest that electron transfer between ascorbate and the TEMPO radical involve orthogonal π-type orbitals consistent with the CPET mechanism.

6.6 Conclusions

Application of the MSDFT method to the hydrogen atom abstraction of ascorbate by the TEMPO radical suggests a concerted PCET mechanism with intermediate electronic adiabaticity. Several properties have been presented supporting this classification. The simple diagnostic test based on the effective diabatic PES computed from MSDFT indicate an electronically non-adiabatic CPET mechanism, while the adiabatic PES computed from these diabatic states displays relatively large adiabatic energy gap. This is reflected in the MSDFT electronic coupling constant, which is of similar magnitude as the aniline/aniline radical self-exchange reaction. The three-dimensional More O'Ferrall-Jencks diagram displays only one ridge and no conical intersection seam, although the ground state and excited state minimum energy pathways are slightly orthogonal to one another near the transition state. The ground state minimum energy pathway and the structural weights of each diabatic state suggest a smooth transition from reactant to product states with slight contribution from excited state 1*a*. Lastly, both the Löwdin atomic charges and SOMO computed using BLKS orbitals are consistent with an electronically non-adiabatic CPET mechanism.

Chapter 7. Kinetic Isotope Effects of Hydrogen Atom Abstraction of Ascorbate by TEMPO Radical

7.1 Introduction

One experimental observable that offers direct insight into concerted proton-coupled electron transfer (PCET) mechanisms is the kinetic isotope effect (KIE) and its solvent and temperature dependence.[9,23,56,130] The larger mass of a deuterium-substituted system than its hydrogen counterpart can have profound effects on the observed rate of proton transfer (or hydrogen atom or hydride transfer). The ratio of the hydrogen to deuterium rate constants indicates the degree to which nuclear quantum effects, including tunneling, contribute to the rate-limiting step of the mechanism. A number of methods have been used to model KIEs in complex systems such as reactions in solution and in enzymes, and it is of particularly interest to understand nuclear quantum effects in proton-coupled electron transfer reactions. Given our current understanding of PCET mechanisms highlighted in Chapter 2, the "amount" of tunneling that is observed could be potentially important in distinguishing electronically adiabatic hydrogen atom transfer (HAT) mechanisms (i.e. over the barrier reaction with small tunneling contributions) from electronically non-adiabatic concerted proton-electron transfer (CPET) mechanisms (i.e. significant tunneling through the potential energy barrier). In this chapter, we aim to interpret experimental KIEs of the formally hydrogen atom abstraction of ascorbate by the TEMPO radical (2,2,6,6-tetramethyl-piperidin-1-oxyl), which has previously demonstrated unusual kinetic solvent effects (KSE).

7.2 Background Information

7.2.1 Kinetic Solvent Effects of Phenols

Ingold and co-workers have extensively studied hydrogen atom abstraction reactions of phenols and have identified specific substrates and solvents that display predictable KSE.[9,49,63,131,132] Phenol reactions displaying "normal" KSE exhibit smaller observed rates in hydrogen-bond accepting solvents, presumably due to hydrogen bonding between the transferring proton and a solvent molecule.[9] As discussed in Chapter 2, Ingold presented a phenomenological rate constant expression to account for the effects of solvent-substrate hydrogen bonding in hydrogen atom abstraction reactions. Reactions that do not follow the "normal" trend are explained in terms of a competing side reaction, namely sequential proton-loss electron transfer (SPLET). Within the context of PCET mechanisms, this corresponds to a stepwise PT/ET mechanism that competes with the concerted PCET mechanism(s). The rate constant expression reflects the competition between these mechanisms as a sum of separate rate constants. This model has proven useful in explaining the unusually large rate constants observed for hydrogen atom abstraction of phenols by free radicals in alcoholic solvents and for phenols with low pK_a values in non-hydroxylic, polar solvents.[9,49,63]

7.2.2 Previous Studies of Ascorbate/TEMPO Radical Reaction

Mayer and co-workers reported KSE of the hydrogen atom abstraction of ascorbate by the TEMPO radical that do not follow the trend of decreased rate in stronger hydrogen bond *accepting* solvents.[34] Based on thermodynamic arguments,[48] Mayer ruled out the possibility of a stepwise mechanism to play a role in the ascorbate/TEMPO

radical reaction in favor of a concerted proton-coupled electron transfer process, and thus it does not follow the formalism of Ingold's SPLET mechanism. In Chapter 6, we have shown that the ascorbate hydrogen abstraction by the TEMPO radical is best described by a CPET mechanism in the gas phase, in accord with Mayer's conclusion. In the following, we restrict our discussion to concerted PCET mechanisms.

Analysis of the ascorbate/TEMPO radical reactions in a variety of solvents lead Mayer and co-workers to identify the importance of local solvation effects to explain the unusually large changes in the observed rate and equilibrium constants.[34] After ruling out bulk solvent effects, such as a change in dielectric constant or ionic strength, the local solvation of ascorbate is suggested to be primarily responsible for the changes in driving force of the ascorbate/TEMPO radical reaction. Comparison of the Abraham et al.[61] empirical solvent parameters with respect to changes in the observed rate and equilibrium constants leads Mayer and co-workers to propose an alternative model (as opposed to Ingold's proposal) of ascorbate/solvent interactions. Rather than the ability of ascorbate to form a hydrogen bond with a solvent hydrogen bond acceptor molecule, which is implied in Ingold's explanation of unusual phenol KSE,[9] the hydrogen bond *donating* ability of a solvent is identified as the important factor. Supported by density functional theory (DFT)[126] and molecular dynamics studies of ascorbate,[127] it is proposed that a solvent molecule forms a hydrogen bond with the deprotonated O3 oxygen of ascorbate and, in turn, increases the bond dissociation free energy of the O2-H bond. It is argued that this secondary effect reduces the observed rate constant and equilibrium constant compared to that of a non-hydrogen bond donating solvent.

The kinetics of hydrogen atom abstraction of ascorbate by the TEMPO radical have also been studied by Sajenko et al. in which temperature dependent KIE are reported for pure water and water/1,4-dioxane solvent mixtures.[35] In pure water, the KIE is 24.2 at room temperature, which is well above the semiclassical limit, suggesting that tunneling is involved in this reaction. The addition of dioxane was found to increase the observed KIE proportional to the dioxane mole fraction of the aqueous mixture. This suggests that reduced solvent polarity tends to enhance nuclear tunneling.

To put these results into context of Mayer's work, the relative effects of a non-polar, non-hydrogen bond donating solvent must be compared to the effects of water. In the studies reported by Mayer, small quantities of various solvents are added to acetonitrile, but it was found to have little effects on the rate and equilibrium constants of the ascorbate/TEMPO radical reaction. When small amounts of water are added, however, there is significant decrease both in rate and equilibrium constants, indicating that water inhibits hydrogen atom transfer. In contrast, when similar mole fractions of dimethoxyethane (DME) are added to acetonitrile, negligible effects were found on rate and equilibrium. Thus, it is reasonable to assume that a nonpolar, non-hydrogen bond donating solvent like 1,4-dioxane would have little effect on the reactivity of the ascorbate towards hydrogen atom abstraction by the TEMPO radical.

Taking into account these observations, the solvent effects on KIE reported by Sjenko et al. can be attributed to reduced water solvent effects, possibly due to disruption of the local hydrogen bonding network surrounding the ascorbate molecule by the dioxane additive. This analysis is consistent with the argument that local solvation is

important in the mechanism of hydrogen atom abstraction of ascorbate by the TEMPO radical. However, it remains unclear as to how this occurs. In this chapter, we investigate the temperature dependence of the KIEs of the ascorbate/TEMPO radical reaction in efforts to elucidate the underlying mechanistic factors contributing to the unusual kinetic solvent effects observed for this reaction.

7.3 Methodology

7.3.1 Non-adiabatic Rate Theory of PCET Mechanisms

Following the work of Cukier,[26] Hammes-Schiffer,[24,53,54,133] and others,[31,87,134] the rate expression for PCET may be expressed as a two-dimensional extension of the one-dimensional Marcus theory of electron transfer, in which electron transfer and proton transfer coordinates are explicitly treated. In the limit of electronically non-adiabatic electron transfer, PCET is best described as a set of paraboloid-shaped free energy surfaces, representing electron-localized reactant and product diabatic states.[24,25] Using the notation of multistate density functional theory (MSDFT) discussed in Chapter 3, electronic diabatic states in CPET are given by

$$\Phi_R^{CPET} = c_{0a}\Psi_{0a} + c_{0b}\Psi_{0b} \quad (1)$$

$$\Phi_P^{CPET} = c_{1a}\Psi_{1a} + c_{1b}\Psi_{1b} \quad (2)$$

where Ψ_γ is the wavefunction of diabatic state γ and c_γ is the configuration interaction coefficient of that state ($\gamma = 0a, 0b, 1a, 1b$). The coupling of protonic states a and b within each electronic state ascribes to a set of two vibrational wavefunctions localized within each electronic state potential well. Thus, the coupling of a PCET reaction is dependent on both the electronic and the protonic state and is termed vibronic coupling

($V_{\mu v}$), where μ and v indicate the proton vibrational wavefunction within electronic states Φ_R^{CPET} and Φ_P^{CPET}, respectively. This coupling is analogous to the one-dimensional ET coupling (V_{RP}) in Marcus theory[51] and the PCET rate constant is given as

$$k = \frac{1}{\hbar}\sum_{\mu}^{\{R\}} P_{\mu}^{R} \sum_{v}^{\{P\}} \left|V_{\mu v}\right|^2 \sqrt{\frac{\pi}{\lambda_{\mu v} k_B T}} \exp\left(\frac{-(\Delta G^{\circ}{}_{\mu v} + \lambda_{\mu v})^2}{4\lambda_{\mu v} k_B T}\right) \tag{2}$$

where P_{μ}^{R} is the Boltzman population of proton vibrational wavefunction level μ localized within the potential well of the reactant electronic state Φ_R^{CPET}, $V_{\mu v}$ is the vibronic coupling of states Φ_R^{CPET} and Φ_P^{CPET} for a given set of vibrational levels μ and v, and $\lambda_{\mu v}$ and $\Delta G^0{}_{\mu v}$ are analogous to Marcus theory's reorganization energy and driving force, respectively, with an additional dependence on the proton vibrational levels μ and v.[25] In the electronically non-adiabatic limit, $V_{\mu v}$ may be approximated by $V_{el}\left\langle \varphi_{\mu}^{R} \middle| \varphi_{v}^{P} \right\rangle = V_{el} S_{\mu v}$, where V_{el} is electronic coupling of states Φ_R^{CPET} and Φ_P^{CPET} and $S_{\mu v}$ is the Franck-Condon overlap of proton vibrational wavefunctions $\left|\varphi_{\mu}^{R}\right\rangle$ and $\left|\varphi_{v}^{P}\right\rangle$.[26,54]

Based on Hammes-Schiffer's expression of electronically non-adiabatic PCET rate, Mayer and co-workers have derived approximate expressions for the hydrogen/deuterium KIE.[87] As in Marcus theory,[51,135] the reorganization energy may be separated into inner and outer contributions, where only the inner sphere reorganization depends on the vibrational state. The outer sphere reorganization effects are assumed to be significantly larger than inner sphere effects; thus, the pre-exponential term $\sqrt{\pi / \lambda_{\mu v} k_B T}$ is of similar magnitude for both isotopes and does not contribute to the KIE. Because the electronic potentials are the same for both isotopes, V_{el} is independent

of vibrational states μ and v and does not contribute to the KIE. Lastly, extensive experimental data,[46,66] suggest $\Delta G^{\circ}_{\mu v} < \lambda_{\mu v}$. This is a key observation that justifies the simplification of the KIE by removing the quadratic dependence of the free energy barrier ($\Delta G^{\ddagger}_{\mu v}$) on $\Delta G^{\circ}_{\mu v}$ and $\lambda_{\mu v}$, leading to a linear free energy relationship

$$\Delta G^{\ddagger}_{\mu v} \approx \frac{\Delta G^{\circ}_{\mu v}}{2} + \frac{\lambda_{\mu v}}{4}. \tag{3}$$

Given these assumptions, the KIE is defined as

$$\text{KIE} \approx \frac{\zeta_H}{\zeta_D}; \quad \zeta_i = \sum_{\mu}^{\{R\}} P_{\mu}^{R} \sum_{v}^{\{P\}} S_{\mu v}^{2} \exp\left(\frac{-\Delta G^{\circ}_{\mu v}}{2k_B T}\right) \exp\left(\frac{-\lambda_{\mu v}}{4k_B T}\right) \tag{4}$$

where i = H, D and ζ_i is a double sum over bound vibrational states, μ and v. In addition, Mayer and co-workers[87] used a weight ($W_{\mu v}$) to quantify the fractional amount each $\mu \rightarrow v$ transition contributes to the overall rate:

$$W_{\mu v} = \frac{P_{\mu}^{R} S_{\mu v}^{2} \exp(-\Delta G^{\circ}_{\mu v} / 2k_B T)}{\sum_{\mu}^{\{R\}} P_{\mu}^{R} \sum_{v}^{\{P\}} S_{\mu v}^{2} \exp(-\Delta G^{\circ}_{\mu v} / 2k_B T)}. \tag{5}$$

7.3.2 Variational Transition State Theory – An Adiabatic Rate Theory

Assuming that a given reaction is well-characterized by a one-dimensional reaction coordinate separable from all other degrees of freedom of a reaction complex, a section of the adiabatic potential energy surface may be identified as the transition state barrier separating reactant from product states (Figure 7.1). If all states within this barrier, i.e. transition states, are assumed to originate from the reactant states and proceed in a forward direction to form product states, then the rate of reaction is the rate at which

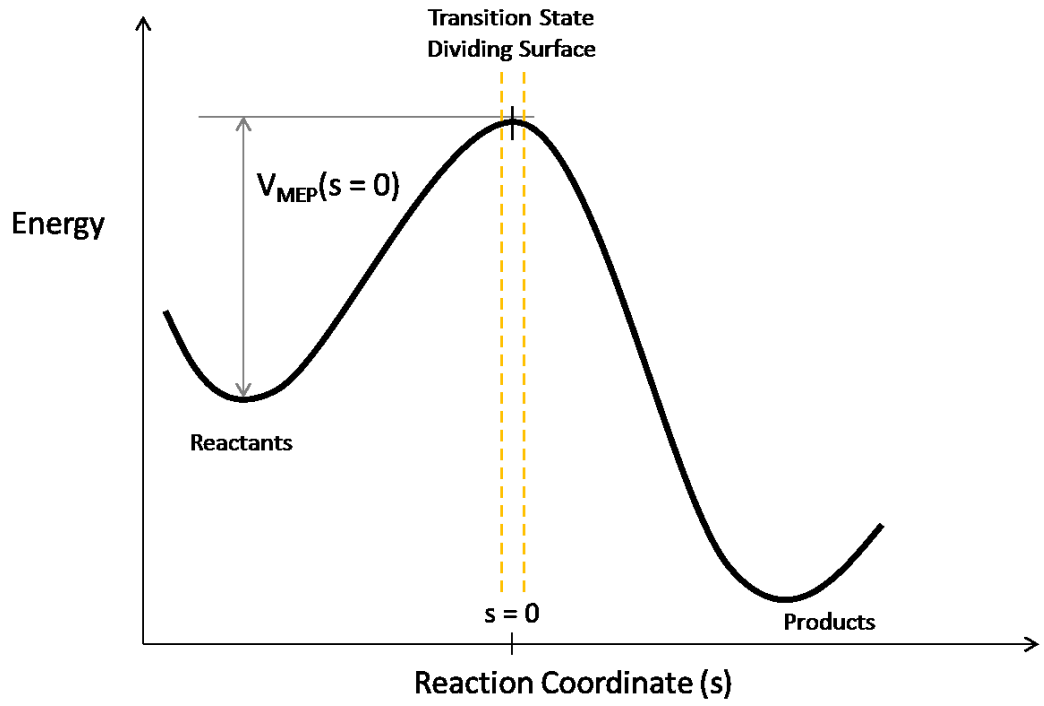

Figure 7.1 Schematic of transition state theory (TST) dividing surface along one-dimensional minimum energy path (MEP) of adiabatic potential energy surface.

transition states cross the barrier. If we assume that all transition states are in quasi-thermal equilibrium with the reactant states, then this rate may be expressed in terms of statistical mechanical partition functions and the relative energy barrier between transition states and reactant states. Known as transition state theory (TST),[36] this rate constant is defined as

$$k^{TST} = \frac{k_B T}{h} \frac{Q^{TS}(s,T)}{\Phi^R(T)} \exp[-V_{MEP}(s=0)/k_B T] \qquad (6)$$

where $k_B T/h$ is known as the frequency factor (k_B is the Boltzman constant, T is temperature, and h is the Planck constant), $Q^{TS}(s,T)$ and $\Phi^R(T)$ are the transition state and reactant partition functions, respectively, and V_{MEP} is the energy of the classical potential energy function at the transition state barrier ($s = 0$). This provides the classical rate

prediction based on a given potential energy function, V_{MEP}, and in fact gives the upper limit to the actual rate. Because real chemical systems may re-cross the transition state barrier several times and may never convert to the product state, a more accurate rate constant may be computed by minimizing the classical rate constant expression with respect to the one-dimensional reaction coordinate (s).

$$k^{CVT} = \min[k^{TST}(T,s)] = k^{TST}(T,s^*)\,. \tag{7}$$

This approach is termed canonical variational transition state theory, or simply CVT,[36] and has proven useful in a variety of chemical systems. The key benefit of using CVT of traditional TST is that both entropic and enthalpic properties are taken into account when choosing the transition state barrier. As a result, the CVT barrier may be before, after, or equivalent to the classical V_{MEP} barrier defined as $s = 0$. In addition, some reactions may even be barrierless in TST, but with a significant entropy barrier in CVT.

Additional improvements are made by including nuclear quantum effects such as tunneling through the classical barrier, zero-point energy effects, non-classical reflection, and non-separability of the reaction coordinate.[36,103] These effects are introduced in the rate expression as a pre-exponential transmission coefficient ($\kappa^{CVT/\gamma}$)

$$k^{CVT/\gamma} = \kappa^{CVT/\gamma} k^{CVT} \tag{8}$$

where γ indicates the level of theory used to compute the quantum mechanical correction. This correction may be computed using ab initio quantum mechanical electronic structure theory and by semi-classical approaches, such as small curvature tunneling (SCT) or large curvature tunneling (LCT).[36,103] Briefly, SCT assumes little deviation from the classical ground state MEP and occurs by vibrationally adiabatic tunneling through a

contracted classical barrier. Contraction of the barrier results in a shorter tunneling distance and increased tunneling probability. On the other hand, LCT is a non-adiabatic correction that assumes tunneling occurs along the linear pathway that connects reactant and product states by the shortest distance. In addition to varying the semi-classical treatment of tunneling, the microcanonical optimized multidimensional tunneling (μOMT) approach may be used in which a transition state barrier is optimized for each total energy of the system.[36]

7.4 Computational Details

The input quantities necessary to compute the non-adiabatic rate theory KIE (eq 4) are determined by solving the one-dimensional time-independent Shrödinger equation $\hat{H}\left|\varphi_\mu^i\right\rangle = E_\mu^i\left|\varphi_\mu^i\right\rangle$, where $\hat{H} = -(\hbar^2/2m)(\partial^2/\partial x^2) + V_i(x)$ and $\left|\varphi_\mu^i\right\rangle$ is the vibrational wavefunction of a bound state μ in the potential energy well of electronic state $i = R$ or P. Here, the potential $V_i(x)$ is defined as Φ_R^{CPET} or Φ_P^{CPET} for $i = R$ or P, respectively. Thus, the one-dimensional reaction coordinate (x) is the linear proton transfer coordinate (ΔR_p) defined in Chapter 6. Using the BEx1D program,[136] each vibrational wavefunction is approximated as a linear combination of 500+ harmonic oscillator functions and the resulting eigenvalue problem is solved for each electronic state. The thermodynamic terms, $\Delta G^\circ_{\mu\nu}$ and $\lambda_{\mu\nu}$, are computed directly from the resulting eigenvalues and the Franck-Condon term is computed as the overlap of corresponding eigenfunctions. By changing the value of m in the Hamiltonian expression, these input values are computed for both the hydrogen (H) and deuterium (D) isotopes.

The adiabatic CVT rate constants are computed using the POLYRATE[137] and GAUSSRATE[138] programs interfaced with Gaussian 09.[139] Starting from the gas-phase optimized transition state structure of the ascorbate/TEMPO radical model system (Chapter 6), the intrinsic reaction coordinate (IRC) method implemented in Gaussian 09[139] was used to compute the minimum energy path along the classical ground state potential energy surface, connecting both the reactant and product states to the transition state. Solvent effects were incorporated by optimizing the transition state structure and IRC using a polarizable continuum model (PCM), as implemented in Gaussian 09.

7.5 Results and Discussion

7.5.1 Temperature-Dependent Kinetic Isotope Effects from Non-adiabatic Rate Theory

The computed eigenvalues of the one-dimensional time-independent Schrodinger equation (i.e. vibrational energy levels) are shown in Figure 7.2 relative to the zero point energy of each potential, Φ_R^{CPET} and Φ_P^{CPET}. The significant anharmonic character of the product potential results in smaller energy gaps between vibrational energy levels compared to those of the reactant potential. In addition, the nearly double-well character of the product potential significantly lowers the inner reorganization energy, defined as the energy of the product state calculated at the equilibrium distance of the reactant state ($\Delta R_p = -0.3$) with respect to the zero point energy of the product state. Isotopic effects further reduce the energy level splitting within each potential, to a greater extent within the product potential well.

The Boltzmann population distribution, thermodynamic terms, and Franck-Condon overlap values are summarized in Table 7.1 for the three largest-weighted $\mu \rightarrow \nu$ transitions of each isotope at $T = 298$ K. Notice the significant contribution of the $0 \rightarrow 1$ transition to the D rate constant, whereas the H rate constant is overwhelmingly dominated by the $0 \rightarrow 0$ transition. The vibrational overlap increases by approximately one order of magnitude for *both* isotopes when going from $0 \rightarrow 0$ to $0 \rightarrow 1$ transitions, so this is not the determining factor. The relative energy of the reactant and product vibrational levels of the $0 \rightarrow 0$ transition is approximately equal for H and D, but the $0 \rightarrow 1$ transition is 2.9 kcal/mol exothermic for D, compared to the nearly isoenergetic $0 \rightarrow 1$ transition of H. Thus, the exothermicity of the $0 \rightarrow 1$ transition accounts for its significant contribution to the D rate constant. As the temperature is increased, the $0 \rightarrow 1$

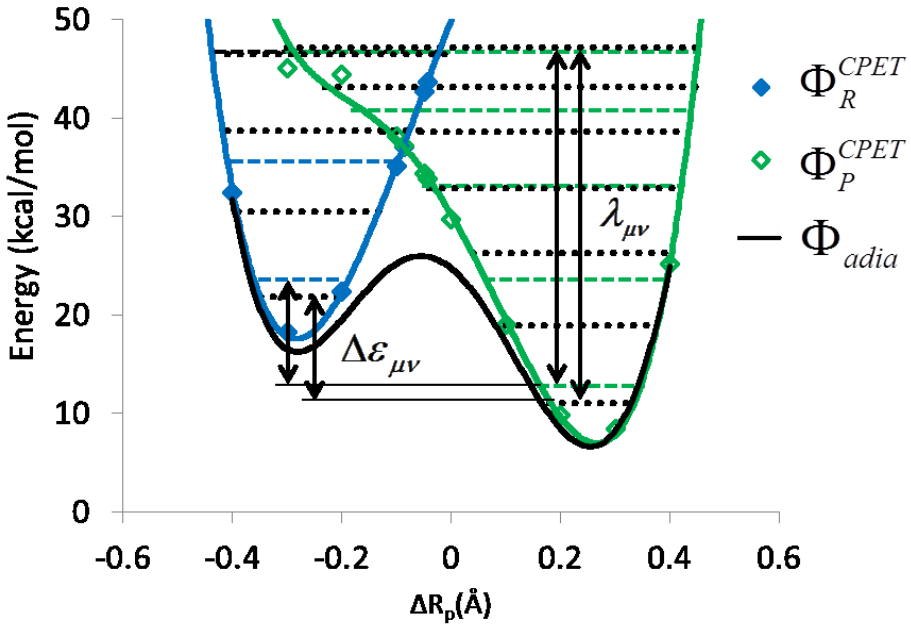

Figure 7.2 Ascorbate/TEMPO radical electron-localized Φ_R^{CPET} and Φ_P^{CPET} potential energy functions and the adiabatic ground state Φ_{adia} (same as Figure 4b), and vibrational energy levels for hydrogen (dashed lines) and deuterium (dotted lines).

Table 7.1. Thermodynamic and vibrational overlap terms for the ascorbate/TEMPO radical model system, including the Boltzmann population and relative weight of the three largest contributing transitions at $T = 298$ K.

	Transition (μ,ν)	P_μ^R	$\Delta\varepsilon_{\mu\nu}$ (kcal/mol)	$\lambda_{in}(\mu,\nu)$ (kcal/mol)	$S_{\mu\nu}$	$W_{\mu\nu}$
H	(0,0)	0.999999998	-10.9	33.9	$1.94\text{x}10^{-3}$	99.2%
	(0,1)	0.999999998	-0.1	23.1	$1.53\text{x}10^{-2}$	0.7%
	(1,0)	0.000000002	-22.8	33.9	$9.89\text{x}10^{-3}$	0.1%
D	(0,0)	0.999999518	-10.7	36.1	$5.92\text{x}10^{-5}$	74.2%
	(0,1)	0.999999518	-2.9	28.2	$8.36\text{x}10^{-4}$	18.8%
	(1,0)	0.000000482	-19.4	36.1	$5.43\text{x}10^{-4}$	4.3%

transition has a larger contribution. For example at $T = 317.4$ K, $W_{01} = 24.5\%$ for D and 1.2% for H.

Using the KIE expression derived by Mayer and co-workers (eq 4), we obtain KIE values of similar magnitude as experiment (Figure 7.3). For example, at T = 298 K the KIE computed using MSDFT and non-adiabatic rate theory is 32.9, compared to experimental values of 31.1 and 24.2 for the 1:1 v/v water-dioxane mixed solvent and pure water, respectively. This is in very good agreement, especially given that no empirical parameters are used to calculate the KIE. In addition, we obtain the correct trend of increasing KIE with decreasing temperature (Figure 7.3). Although the temperature-dependence is over-estimated by our approach, these results indicate that the temperature-dependent KIE of the hydrogen atom abstraction of ascorbate by the TEMPO radical is well characterized by non-adiabatic rate theory using MSDFT-computed potential energy functions.

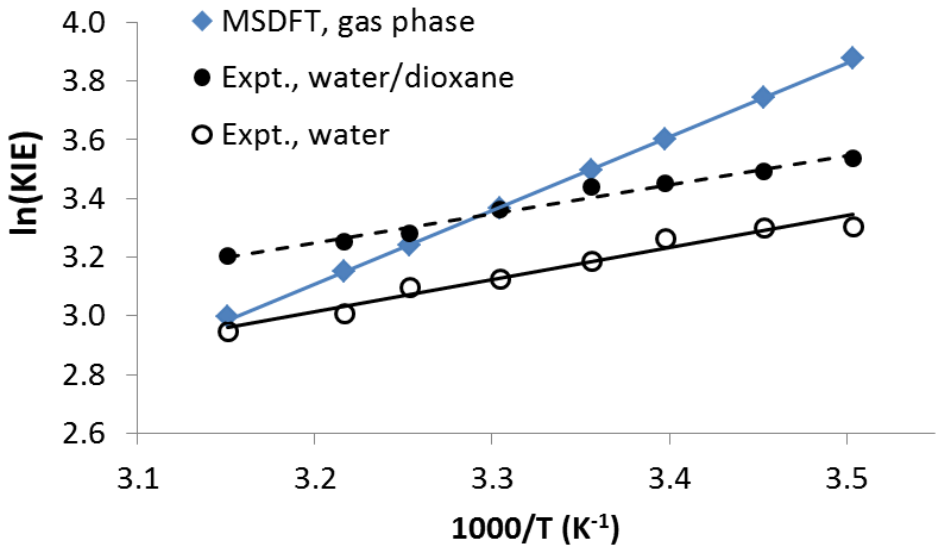

Figure 7.3 Temperature dependence of kinetic isotope effect from experiment (open and closed black circles) and MSDFT (blue diamonds).

7.5.2 Kinetic Solvent Effects from Canonical Variational Transition State Theory

First, we compare the position along the reaction coordinate and the energy with respect to the reactant state for the classical barrier (V_{MEP}), the vibrationally adiabatic barrier (V_{adia}), and the CVT optimized barrier ($V_{CVT}(s^*)$), given in Table 7.2. By definition, the V_{MEP} barrier occurs at $s = 0$ and, in this case, is 11.5 kcal/mol higher in energy than the reactant state, including zero point energy effects for both the reactant and transition states. The V_{adia} barrier, used to compute the SCT correction, is located before the V_{MEP} barrier at s = -0.0973 Å and is 1.0 kcal/mol higher in energy, consistent with contraction of the classical barrier to give larger SCT transmission probability. The optimized CVT barrier occurs after V_{MEP} and is 1.1 kcal/mol lower in energy. The same is true for potential energy barriers computed using PCM to include water solvent effects (Table 7.2). In general, an aqueous environment increases the barrier by 2 – 4 kcal/mol.

Table 7.2 Potential energy barriers and corresponding reaction coordinate values (s) computed for the ascorbate/TEMPO radical model system at $T = 298$ K.

		max V_{MEP} (s = 0)		max V_{adia} (s ≠ 0)		V_{CVT} (s = s*)	
		Classical	w/ ZPE	s	w/ ZPE	s*	w/ ZPE
Gas Phase	H	14.82	11.51	-0.0973	12.48	+0.0397	10.56
	D	14.82	12.46	-0.0729	12.86	+0.0528	11.66
Water	H	18.14	14.50	-0.0442	14.73	-0.0095	14.59
	D	18.14	15.45	-0.0370	15.62	-0.0069	15.51

In the POLYRATE and GAUSSRATE programs, the order of the barriers along the reaction coordinate determines how the transmission coefficient is computed. In general, the CVT transmission coefficient for the adiabatic ground state is defined as the ratio of the thermally averaged quantum mechanical transmission probability (P^{γ}, γ = SCT, LCT, μOMT) and the thermally averaged classical transmission probability (P^{C})

$$\kappa^{CVT/\gamma} = \frac{\int_0^{\infty} P^{\gamma}(E)\ e^{-E/k_B T} dE}{\int_0^{\infty} P^{C}(E)\ e^{-E/k_B T} dE} \tag{9}$$

where the classical probability is characterized by a step function equal to zero for all energies below the CVT optimized barrier and equal to one for all energies above the CVT barrier.[36] Thus, the CVT transmission coefficient may be expressed as

$$\kappa^{CVT/\gamma} = \frac{\int_0^{\infty} P^{\gamma}(E)\ e^{-E/k_B T} dE}{\int_{V_{CVT}(s^*)}^{\infty} e^{-E/k_B T} dE}. \tag{10}$$

In POLYRATE/GAUSSRATE, this value is separated into two factors,

$$\kappa^{CVT/\gamma} = \kappa^{CVT/CAG}\kappa^{\gamma} = \frac{\int_{\max V_{adia}(s)}^{\infty} e^{-E/k_BT}\,dE}{\int_{V_{CVT}(s^*)}^{\infty} e^{-E/k_BT}\,dE} * \frac{\int_0^{\infty} P^{\gamma}(E)\; e^{-E/k_BT}\,dE}{\int_{\max V_{adia}(s)}^{\infty} e^{-E/k_BT}\,dE} \qquad (11)$$

where the first considers the contribution from energies between the CVT optimized barrier and the vibrationally adiabatic maximum and the second considers the remaining energies between the vibrationally adiabatic maximum and infinity.[36] For cases in which max V_{adia} (s) is after $V_{CVT}(s^*)$, significant classical recrossing may occur due to the additional barrier encountered between $V_{CVT}(s^*)$ and the max V_{adia} barrier. Thus, the transmission coefficient is given by eq 11. However, if max $V_{adia}(s)$ is before $V_{CVT}(s^*)$, then the system already has sufficient energy to overcome $V_{CVT}(s^*)$ and $\kappa^{CVT/CAG} = 1$. In this case, the transmission coefficient is defined as

$$\kappa^{CVT/\gamma} = \kappa^{\gamma} = \frac{\int_0^{\infty} P^{\gamma}(E)\; e^{-E/k_BT}\,dE}{\int_{\max V_{adia}(s)}^{\infty} e^{-E/k_BT}\,dE}. \qquad (12)$$

For the ascorbate/TEMPO radical, max $V_{adia}(s)$ is before $V_{CVT}(s^*)$ along the reaction coordinate for both gas phase and water solvent (Table 7.2). Thus, the curvature corrected CVT transmission coefficients reported here are defined by eq 12.

Gas phase CVT rate constants (k^{CVT}) are 2580 s^{-1} and 200.1 s^{-1} for hydrogen and deuterium substituted systems, respectively. These values give a CVT KIE of 12.9 (Table 7.3). Using a polarizable continuum model as implemented in Gaussian 09,[139] aqueous CVT rate constants were computed as 158.0 s^{-1} and 29.28 s^{-1} for hydrogen and deuterium substituted systems, respectively, to give a CVT KIE of 5.39 (Table 7.4). Although the

Table 7.3 Gas phase CVT transmission coefficients, rate constants, and KIE of the ascorbate/TEMPO radical model system at $T = 298$ K.

Gas Phase	γ	$\kappa^{CVT/\gamma}$	$k^{CVT/\gamma}$ (s^{-1})	KIE
Hydrogen	CVT	–	2.580×10^{3}	–
	SCT	21.82	5.630×10^{4}	–
	LCT	112.6	2.906×10^{5}	–
	μOMT	112.7	2.906×10^{5}	–
Deuterium	CVT	–	2.001×10^{2}	**12.9**
	SCT	15.29	3.060×10^{3}	**18.4**
	LCT	54.15	1.084×10^{4}	**26.8**
	μOMT	54.91	1.099×10^{4}	**26.5**

Table 7.4 Water CVT transmission coefficients, rate constants, and KIE of the ascorbate/TEMPO radical model system at $T = 298$ K.

Water	γ	$\kappa^{CVT/\gamma}$	$k^{CVT/\gamma}$ (s^{-1})	KIE
Hydrogen	CVT	–	1.580×10^{2}	–
	SCT	4.072×10^{3}	6.431×10^{4}	–
	LCT	1.808×10^{4}	2.856×10^{6}	–
	μOMT	1.809×10^{4}	2.857×10^{6}	–
Deuterium	CVT	–	2.928×10^{1}	**5.39**
	SCT	6.574×10^{3}	1.925×10^{4}	**3.34**
	LCT	1.086×10^{3}	3.180×10^{4}	**89.8**
	μOMT	1.351×10^{3}	3.954×10^{4}	**72.2**

classical CVT rate constants reproduce the experimental trend of smaller KIE in pure water, the magnitude of the KIE is well below experimental values for both gas phase and water computations (Table 7.5). To incorporate the quantum mechanical nature of this

Table 7.5 Experimental rate constants and KIE of the ascorbate/TEMPO radical reaction in pure water and 1:1 water/1,4-dioxane v/v mixed solvents at T = 298 K.

Experiment	Solvent	k ($M^{-1}s^{-1}$)	KIE
Hydrogen	Pure Water	2.20	-
	1:1 Water/Dioxane	5.50	-
Deuterium	Pure Water	0.091	**24.2**
	1:1 Water/Dioxane	0.177	**31.1**

reaction, semi-classical transmission coefficients ($\kappa^{CVT/\gamma}$) for γ = SCT, LCT, and μOMT, were computed in both the gas phase and aqueous environment (Table 7.3 and 7.4). The SCT correction gives a reasonable KIE in the gas phase (18.4) and reproduces the experimental trend in water, but the aqueous SCT KIE is much smaller than experiment. In fact, both the uncorrected CVT and semi-classically corrected SCT rate constants give a KIE within the semi-classical limit, suggesting that tunneling does not contribute to the overall mechanism, which is clearly in contradiction to experimental results.

On the other hand, the LCT and μOMT corrections, which are semi-classical approximations to non-adiabatic tunneling effects, provide gas phase KIE values that agree well with experimental values in water/dioxane mixture solution. Unfortunately, these semi-classical corrections grossly overestimate the magnitude of the aqueous KIE (89.8 and 72.2, respectively), resulting in not only quantitative disagreement with experiment, but the incorrect trend in solvent effects. Taken together, these results suggest that non-adiabatic tunneling significantly contributes to the mechanism of the hydrogen atom abstraction of ascorbate by the TEMPO radical, demonstrated by the quantitatively accurate LCT and μOMT gas phase KIE values. However, the bulk effects

of an aqueous environment captured by PCM do not account for the solvent dependence of the KIE. Thus, it is suggested that explicit solvation models are necessary to accurately model this reaction.

7.6 Conclusions

Based on non-adiabatic rate theory, the MSDFT potential energy surfaces of the two-state CPET diabatic state model presented in Chapter 6 were used to compute vibrational overlap and thermodynamic terms necessary to compute the KIE of the hydrogen atom abstraction of ascorbate by the TEMPO radical. It is emphasized that these input values were determined solely by the character of the MSDFT potentials. The accuracy of this approach is demonstrated by the good quantitative agreement between the MSDFT computed KIE values and experimental results. Further analysis suggests that the relative energies of the reactant and product vibrational states were found to be the origin of the relatively large experimental KIE.

The qualitative trend of the KIE temperature dependence was reproduced using the non-adiabatic rate theory KIE expression (eq 4). In addition, the LCT and μOMT tunneling approximations are necessary to give a reasonable KIE magnitude when using the adiabatic rate theory of CVT. This suggests that the mechanism of the hydrogen atom abstraction of ascorbate by the TEMPO radical involves significant non-adiabatic character, in agreement with the CPET vs. HAT diagnostic test described in the previous chapter. However, using the LCT and μOMT corrections for a PCM-solvated system overestimates the CVT computed KIE. It seems that explicit solvation models are necessary to capture the local solvent effects of an aqueous environment. This

observation is in line with the analysis of Mayer and co-workers that local solvent effects are responsible for the unusual solvent effects observed for this reaction.

Furthermore, our current MSDFT model is a static picture of the system, neglecting solvent polarization effects, dynamic fluctuations, and coupled motions along the reaction coordinate. The shortcomings of this model are illustrated in the overestimation of the temperature dependence of the KIE. As noted by Hammes-Schiffer,[56] incorrect temperature dependence is a manifestation of the neglect or poor treatment of the dynamical frequencies of the donor-acceptor distance. We propose that implementation of the MSDFT method in a combined quantum mechanical/molecular mechanical (QM/MM) approach will accurately capture both the solvent effects and the dynamics of the donor-acceptor distance. Thus, for future applications, especially for protein systems, molecular dynamics simulations will be employed to incorporate effects of local dynamical fluctuations and explicit solvation.

Chapter 8. The Quantum Coherent Mechanism for Singlet Fission: Experiment and Theory

8.1 Introduction

For enzymatic reactions, fluctuations in the protein environment can have significant effects on the mechanism of PCET and other charge-transfer processes. To include these protein reorganization effects, MSDFT has been implemented in a combined quantum mechanical/molecular mechanical (QM/MM) approach.[21,37,140] To demonstrate its applicability, MSDFT QM/MM single point energy calculations are used to elucidate a quantum coherent mechanism for singlet fission in thin film pentacene monolayers.[39]

8.2 Background Information

Since its discovery in 1965,[4] singlet fission, that is, the conversion of a singlet exciton into two triplet excitons in molecular materials, has remained a fascinating but exotic photophysical phenomenon.[5] Recently, renewed interest in singlet fission[6] has been driven mainly by the potential application of this process in boosting the power conversion efficiency of solar cells.[7,8] Singlet fission has been reported for a number of molecular systems. Particularly noteworthy are crystalline solids or aggregates of tetracene,[9,10] pentacene,[11,12] 1,3-diphenylisobenzofuran,[13] and carotenoids[14] where high singlet fission yields have been reported. The predominant mechanism used to describe singlet fission comes from Merrifield's theory[15,16] for the reverse process of triplet-triplet annihilation and can be written as

$$S_1 \underset{k_2}{\overset{k_{-2}}{\rightleftharpoons}} {}^1(TT) \underset{k_1}{\overset{k_{-1}}{\rightleftharpoons}} T_1 + T_1 \qquad (1)$$

where a photo-excited singlet (S_1) evolves into two triplets on adjacent chromophores known as a correlated triplet pair, ^{1}(TT), or a multiexciton state (ME), which further separates into two individual triplets (T_1). The intermediate ^{1}(TT) state, proposed first as a non-radiative decay mechanism in crystalline tetracene,[17] is a coherent superposition of the nine triplet pair states.[15,18] Coherent oscillations between different spin states of ^{1}(TT) have been observed on the nanosecond time scale in fluorescence from tetracene.[19] Unlike long-time spin dynamics, much less is known about how ME is formed from S_1, which is determined by the electronic Hamiltonian and happening on the shorter time scale of femtoseconds to picoseconds. Earlier treatments[5,6] assumed an incoherent rate constant (k_{-2}) for the $S_1 \rightarrow$ ME transition. Zimmerman and co-workers attributed conical intersections as responsible for the ultrafast transition from S_1 to ME in pentacene.[20,21] Greyson et al.[22] and Teichen and Eaves[23] studied the $S_1 \rightarrow$ ME transition via intermediate charge transfer (CT) states.

Despite the progress described above, the lack of experimental observation of ME has been a major obstacle to establishing the singlet fission mechanism.[6] Previous time resolved studies of singlet fission have relied on transient absorption and time-resolved fluorescence spectroscopies. There is now a consensus that singlet fission occurs on the ultrafast time scale of 70100 fs in crystalline pentacene.[11,12] In crystalline tetracene, the reported singlet fission times vary broadly, from less than 300 fs to about 1 ns,[6] although recent measurements seem to converge to the time scales of 50-80 ps based on population

decay of S_1.[10] There has been no experimental observation of ME until recently when Zhu and co-workers[24,25] applied time-resolved two-photon photoemission spectroscopy (TR-2PPE) to tackle the problem, as detailed below.

8.3 Experimental Evidence for the Multiexciton State and a Quantum Coherent Mechanism

In TR-2PPE, a pump laser pulse creates excitonic state(s); after a controlled time-delay, the probe pulse ionizes the excitonic states and the photoelectrons are detected. For ME, photoionization destroys the correlated triplet pair by ionizing one triplet, leaving behind another triplet and a hole. As a result, ME shows up in a TR-2PPE spectrum with an electron kinetic energy similar to that from an individual T_1, not S_1.

Figure 8.1a and b shows pseudocolor plots of TR-2PPE spectra for tetracene (a) and pentacene (b) thin films.[24,25] There is a high-energy feature assigned to S_1 and a lower one to T_1. While the formation of S_1 upon photoexcitation and T_1 at longer times are expected, what is most surprising is the observation of a state at nearly the same energy and intensity as T_1 but which rises concurrently with S_1. We assign this T_1-like state at early times to the ME state. The concurrent rise of the S_1 and ME populations cannot be explained by conventional models in which the S_1 converts incoherently to ME, but can be explained by the scheme illustrated below:

$$\left[S_1 \Leftrightarrow ME\right] \rightleftarrows ME' \rightleftarrows T_1 + T_1 \qquad (2)$$

Here, the S_1 state is optically excited and the dark ME state is populated through electronic coupling to S_1, forming a quantum superposition state $\left[S_1 \Leftrightarrow ME\right]$ on the ultrafast time scale (with a time constant inversely proportional to the coupling strength).

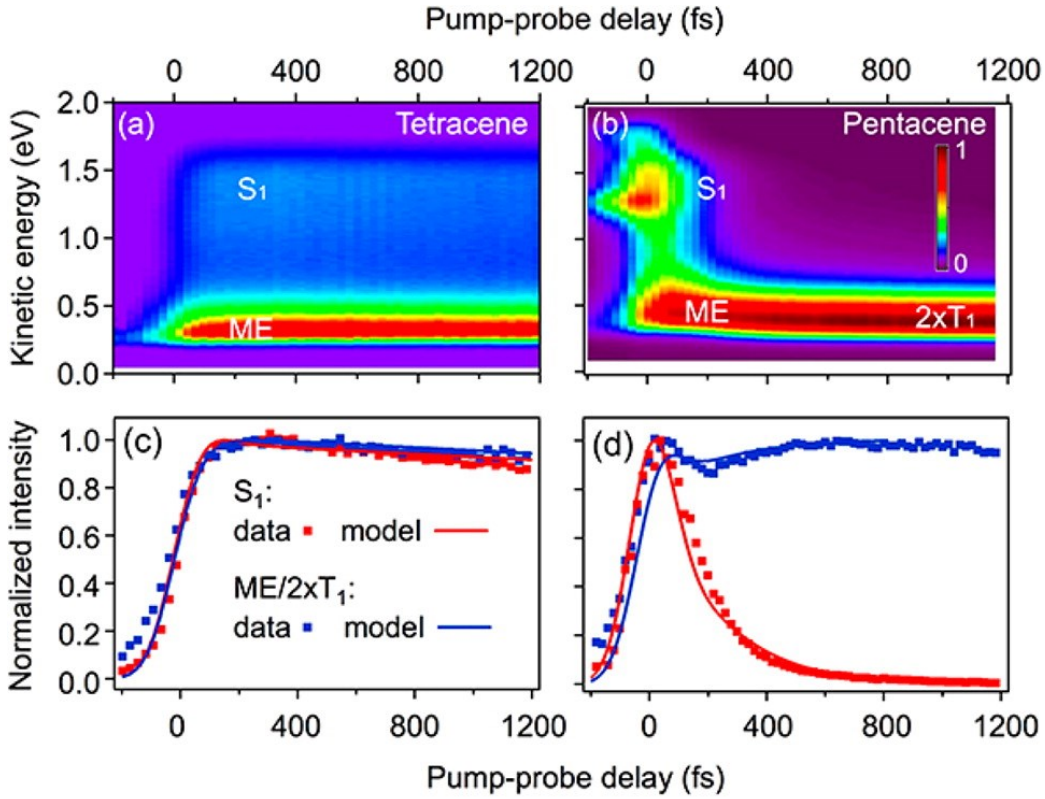

Figure 8.1 Pseudocolor plots of TR-2PPE spectra of tetracene (a) and pentacene (b) thin films, excited at $h\nu_1$ = 2.32 and 2.15 eV, respectively. The excitonic states are probed with an ionization photon of $h\nu_2$ = 4.65 eV. The energetic positions of the S_1, ME, and 2 × T_1 are indicated. The lower panels show the normalized 2PPE intensities of the S_1 (red dots) and the ME/2 × T_1 (blue dots) states for tetracene (c) and pentacene (d), respectively. The solid curves are simulations from the three-state model.

Once the ME loses electronic coupling to S_1, we call the resulting multiexciton state ME', which may be initially on a pair of neighboring molecules and may diffuse apart and also loses spin coherence, evolving eventually into two independent triplets. We define the fission rate as the rate at which the multiexciton state loses electronic coupling to S_1.[25] Note that $[S_1 \Leftrightarrow ME]$ can be said to possess "state coherence", not "process coherence" resulting, for example, from the excitation of multiple bright states within the bandwidth of a short laser pulse.[26]

The TR-2PPE results show a clear difference between pentacene and tetracene. In pentacene, the $[S_1 \Leftrightarrow ME]$ state is short-lived (τ_{SF} = 100 ± 20 fs), and this can be attributed to relaxation processes that destroy the quantum coherence on an ultrafast time scale. The energetic relaxation is characterized by a total decrease of 0.11 eV in electron energy from the multiexciton state, seen in Figure 8.1b, as predicted by quantum chemistry calculations.[20] In tetracene, the $[S_1 \Leftrightarrow ME]$ superposition state is much longer-lived (τ_{SF} = 7 ps), Figure 8.1c,[25] and this time scale has also been verified in analysis of one versus two electron transfer from the superposition state.[27] There is no measurable energetic relaxation as the ME state evolves into ME'/2T_1 (Figure 8.1a). The definition of singlet fission time based on the lifetime of $[S_1 \Leftrightarrow ME]$ is different than traditional definitions based on the S_1 population decay time of ~60-80 ps.[10,25]

To model the excitation and the subsequent evolution of the superposition state, we start with a phenomenological three-state model, where the Hamiltonian of the system can be written as

$$\hat{H}_{ME} = \begin{pmatrix} E_{S0} & -\mu E(t) & 0 \\ -\mu E(t) & E_{S1} & -W \\ 0 & -W & E_{ME} \end{pmatrix} \quad (3)$$

where E_{S0}, E_{S1}, E_{ME} are the energies of the S_0 (ground state), S_1, and ME state, respectively. The S_1 state is populated from S_0 by the laser field $\mu E(t)$ in the dipole approximation and converts coherently to the dark ME state through the electronic coupling W. We obtain the time evolution of the states by a density matrix approach using the Liouville-von Neumann equation,[28]

$$i\hbar\frac{\partial\hat{\rho}}{\partial t}=\left[\hat{H}_{ME},\hat{\rho}\right]-i\hbar\hat{D} \tag{4}$$

where the diagonal ρ_{ii} element represents the population of state i; the off-diagonal ρ_{ij} represents the coherence between states i and j; and $D_{ij}=\Gamma_{ij}\left(\rho_{ij}-\rho_{ij}^{0}\right)$ characterizes the interaction with the environment. The diagonal elements of Γ_{ij} are population relaxation rates while the off-diagonal elements are coherence dephasing rates.[24] ρ_{ij}^{0} is the steady-state density matrix, for which we assume all off-diagonal terms are zero. To account for the experimental observation, we find that W must be of the order of 100 meV, as shown by solid curves in Figure 8.1c and d for W = 200 and 330 meV, respectively, along with normalized experimental data. The experimental observation and phenomenological simulation in Figure 8.1 suggest strong electronic coupling between S_1 and ME. This raises a number of interesting questions: (1) Is there a theoretical basis for the large coupling constant between S_1 and ME? (2) Is the microscopic origin of this coupling direct or involving charge-transfer intermediates?[22] (3) How does delocalization in the crystalline solid affect singlet-multiexciton coupling? (4) What is the role of coupling to the thermal bath in singlet fission dynamics? In the following, we present our initial theoretical effects in addressing the above questions.[29–31]

8.4 Multistate Density Functional Theory: Indirect Coupling between S_1 and ME via CT States

We start by answering the first two questions, that is, the magnitude and the direct or indirect nature of S_1-ME coupling. It is difficult if not impossible to determine the intermolecular electronic coupling directly using conventional wave functional theory or

density functional theory (DFT) because molecular or Kohn-Sham orbitals are delocalized over the entire system. Here, we employ multistate density functional theory (MSDFT),[32] in which the exciton and CT wave functions of each monomer are localized within the molecular fragment, to quantify the energies of S_1, ME, and CT states and the electronic coupling matrix elements.[29] In a crystalline solid, S_1 is delocalized due to dipole-dipole interactions, forming a Frenkel exciton band, while CT excitons are delocalized due to both electronic and dipole-dipole interactions.

Our calculations employed a tetracene monolayer based on the crystal structure in the a-b plane for a tetracene thinfilm,[33] Figure 8.2, consisting of 56 (7 x 8) monomers with a subset (gold color) treated quantum mechanically. In MSDFT,[32] each monomer is treated by DFT with Kohn-Sham orbitals strictly localized within the monomer space, that is, block-localized Kohn-Sham (BLKS) orbitals expanded over basis functions

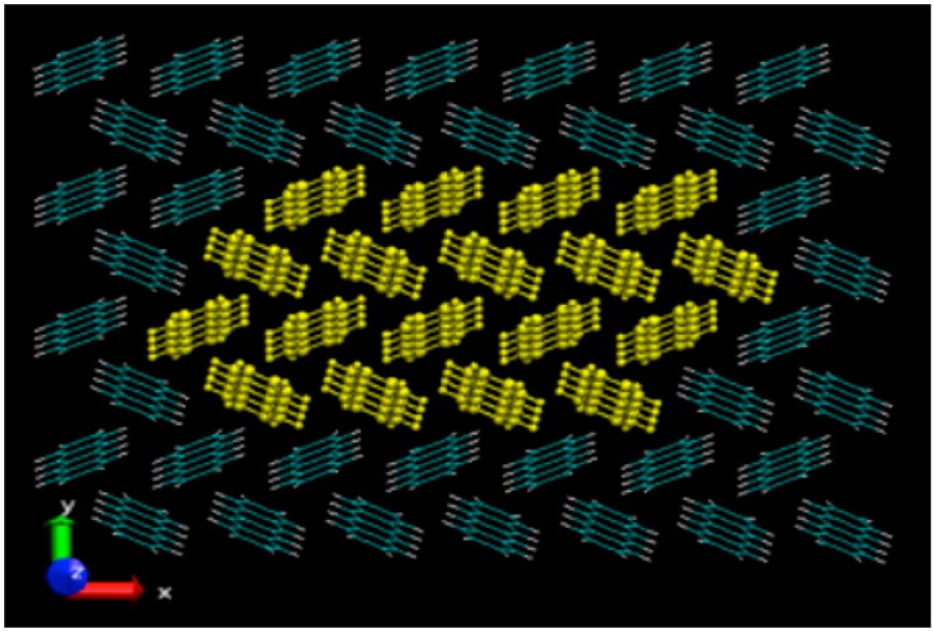

Figure 8.2 Structure of the tetracene monolayer containing 56 molecules, with the gold color region treated quantum mechanically.

located on the monomer atoms only. The monolayer wave function is approximated by a Hartree product of the determinant wave functions of individual monomers. Consequently, Coulomb and mutual polarization interactions among all monomers are explicitly included. To account for the exchange interaction between two molecules that form each ME or CT state, the interacting monomers are grouped into a single fragment, described by a Slater determinant that is constructed from the monomeric BLKS orbitals. Thus, the Kohn-Sham functions for the S_1 state localized on monomer u, the triplet pair with an overall singlet spin (ME), and the CT state involving monomers *u* and *v*, are given:[29]

$$\Phi_{uv}(ME) = \hat{A}\{\Omega_u(T_1^{\uparrow\uparrow})\Omega_v(T_1^{\downarrow\downarrow})\}\prod_{k\neq u,v}^{N}\Psi_k(S_0) \tag{5}$$

$$\Phi_{uv}(CT) = \hat{A}\{\Omega_u(D^{\bullet+})\Omega_v(A^{\bullet-})\}\prod_{k\neq u,v}^{N}\Psi_k(S_0) \tag{6}$$

$$\Phi_{uv}(S_1) = \hat{A}\{\Omega_u(S_1)\Omega_v(S_0)\}\prod_{k\neq u,v}^{N}\Psi_k(S_0) \tag{7}$$

where N is the total number of tetracene molecules in the system, $\hat{A}$ is the antisymmetrizer, and Ω_u denotes the product of occupied BLKS orbitals on monomer *u*. In eq 5, $\Psi_k(S_0)$ is a Slater determinant of monomer *k* in the ground state, and $\hat{A}\{\Omega_u(X)\ \Omega_v(Y)\}$ specifies a superfragment consisting of two coupled monomers u and v, in which the corresponding localized electronic configurations are specified in parentheses with X = S_0, S_1, T_1, $D^{\bullet+}$, and $A^{\bullet-}$; the last two represent molecular donor and acceptor, respectively, in the CT state. The arrows in T_1 and T_1 are used to emphasize that Sz of the coupled triplet configurations is zero. For the coupled monomer pair in $\hat{A}\{\Omega_u(X)\ \Omega_v(Y)\}$,

both Coulomb and exchange interactions are explicitly treated by DFT with BLKS orbitals, whereas only the Coulomb potential from the rest of the system is included.[29]

We performed all calculations in DFT with the PBE0 functional and the 6-31G(d) basis set,[34,35] using a modified version of GAMESS,[36] as detailed elsewhere[29] and summarized in the Supporting Information. The intermolecular electronic coupling constants, directly expressed in $\langle \Phi_{uv}(S_1)|\hat{H}|\Phi_{uv}(ME)\rangle$ or mediated through CT, $\langle \Phi_{uv}(S_1)|\hat{H}|\Phi_{uv}(CT)\rangle$ and $\langle \Phi_{uv}(CT)|\hat{H}|\Phi_{uv}(ME)\rangle$, were determined by MSDFT.[26,29] The direct coupling between S_1 and ME and between two ME states by the two-electron part of the Hamiltonian is rather weak, in the range of 0.5-3 meV for the nearest tetracene neighbors. For comparison, a value of ~5meV was obtained for a pentacene dimer by a restricted active space and two spin flip method (RAS(4,4)-2SF).[141] Note that the strong S_1-S_1 electronic coupling (3 to 65 meV) is responsible for the formation of a Frenkel exciton band and, along with the significant S_1-CT coupling, for the Davydov splitting in tetracene.[142] The most significant finding is that electronic coupling constants between S_1 and CT states or between ME and CT states (50-140 meV) are 1-2 orders of magnitude larger than those between S_1 and ME. Thus, the large S_1-ME coupling suggested in Figure 8.1 is most likely not due to direct coupling, but a result of indirect coupling via the CT intermediate states.

Since publication of this *Accounts of Chemical Research* article, MSDFT electronic coupling constants have been computed for a thin-film pentacene monolayer. Following the same approach described above for tetracene, electronic coupling constants for a series of pentacene dimers were computed using PBE0/6-31G(d). Similar trends

were found for pentacene as reported for tetracene. S_1-ME and ME-ME coupling is very weak (0.0 – 1.0 meV), while the S_1 state displays moderate delocalization with S_1-S_1 coupling of 1.0 – 12 meV. The most significant finding is pentacene, as in tetracene, involves high-energy CT intermediate states in coupling S_1 and ME states, where S_1-CT and CT-ME coupling constants were found to be 30 – 80 meV.

8.5 Density Matrix Dynamics: Role of Delocalization and the Thermal Bath

We now demonstrate using density matrix theory that the calculated coupling matrix elements from section 8.4 can indeed account for salient features in experimental observations. In particular, we address the roles of delocalization and coupling to the thermal bath (i.e., questions 3 and 4 at the end of section 8.3 by calculating the time evolution of the S_1, CT, and ME populations for a crystalline tetracene lattice in a thermal bath at both phenomenological and microscopic levels.

We start with solving eq 4 using experimental energy detuning values of E_{ME} - E_{S1} = 0.17 eV, E_{CT} - E_{S1} = 0.3 eV,[25,27] and calculated matrix elements for tetracene clusters of various sizes. As an example, the Hamiltonian for a five-molecule cluster is shown schematically in Figure 8.3. This Hamiltonian, which is not spin-adapted, includes a total of 10 S_1 states, 16 ME states, and 32 CT states. Here, we included only nearest neighbors except monomers 3 and 5 (Figure 8.3a). Given the large size of the system, we first adopt a phenomenological description of relaxation and dephasing rates. Since we focus on the initial excitation of the superposition state, in particular, the fast rise in ME population, we set all population decay rates (Γ_{ii}) to zero and set all dephasing rates (Γ_{ij}) to 50 meV/p, which is typical for electronic dephasing rates in molecules; we will return to these issues

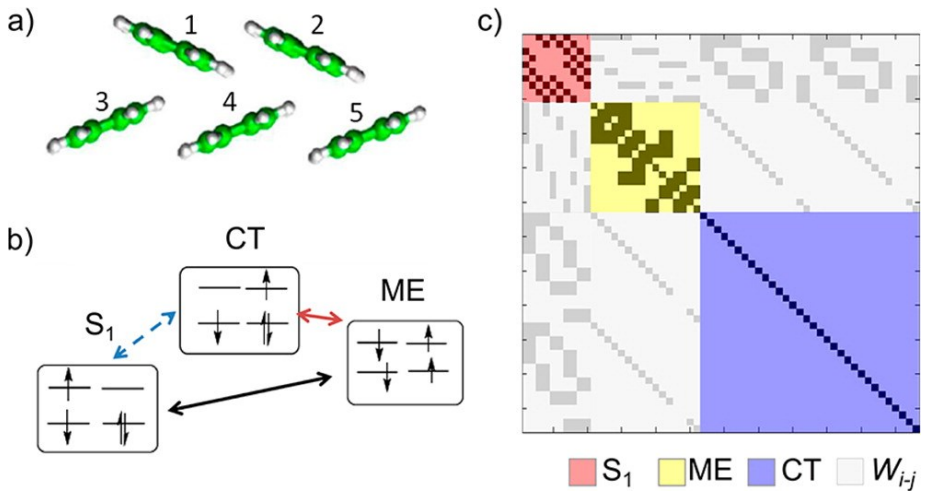

Figure 8.3 (a) Schematic illustration of a five molecule cluster used in density matrix modeling; (b) coupling of S1 with ME directly (black arrow) or via CT exciton intermediates (blue and red arrows); (c) graphical illustration of the Hamiltonian containing three diagonal blocks: S_1 (pink, 10 states), ME (yellow, 16 states), and CT (violet, 32 states). The nonzero elements are shown as dark spots. The gray regions show coupling constants between different types of states, with nonzero coupling constants in dark gray.

below when we present preliminary results of a microscopic Redfield theory calculation that includes both population decay and coherence dephasing. At t = 0, we assume the singlet population is distributed uniformly over the molecules in the cluster, with the sum of amplitudes equaling one, since S_1 is known to delocalize over approximately 10 molecules in crystalline tetracene.[143] We evolve the density matrix $\rho(t)$ using eq 4. Figure 8.4a-c shows S_1, CT, and ME populations for cluster sizes of 2, 5, and 10 tetracene molecules, respectively, embedded electrostatically in the monolayer environment depicted in Figure 8.2. For all sizes, S_1 converts to CT and ME within the first 200 fs, after which the dephasing inhibits any further population transfer. The rise times for the CT and ME populations for a dimer are slightly longer than those of larger tetracene clusters. As the cluster size increases, the S_1 state on each molecule can couple to

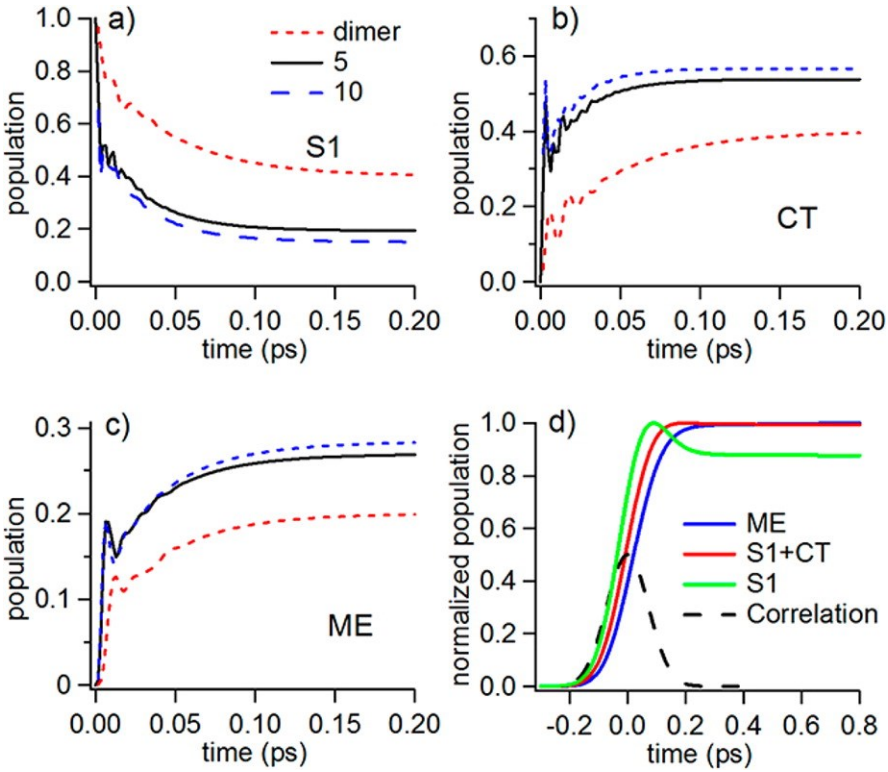

Figure 8.4 Populations of the S_1 (a), CT (b), and ME (c) states as a function of time after photoexcitation obtained from density matrix calculation of crystalline tetracene. We show the results for three cluster sizes (red, black, and blue for 2, 5, and 10 tetracene molecules). Panel (d) shows the S_1 + CT and ME population for the 5 tetracene cluster, convoluted with a Gaussian function with a FWHM of 170 fs to represent the experimental cross-correlation.

multiple CT and ME states, proportional to the number of nearest neighbors; this increases the number of channels for the conversion from S_1 to CT and ME, and hence the conversion rate. A similar density-of-states argument has been proposed for multiexciton generation in semiconductor quantum dots.[37]

The S_1, S_1 + CT, and ME populations from the simulation (for a cluster of five) are convoluted with the experimental two-pulse cross-correlation and shown in Figure 8.4d. The S_1 + CT and ME populations rise up with a time-lag of only ~20 fs, and the two populations maintain a constant ratio after excitation, in qualitative agreement with

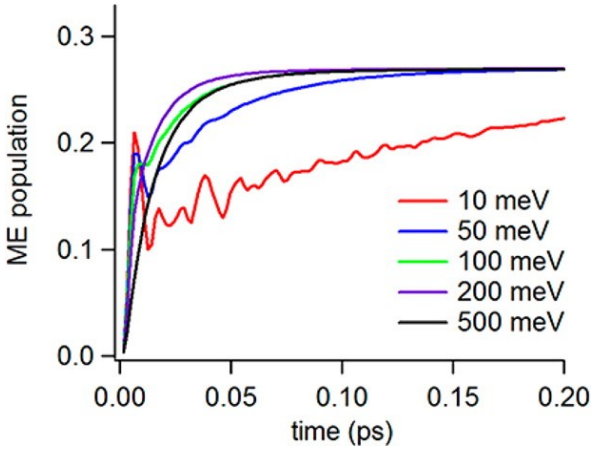

Figure 8.5 Calculated time-dependent population of the ME state for a cluster size of five tetracene molecules in the crystalline lattice at the indicated dephasing rates (10 – 500 meV).

experimental observation in Figure 8.1. As a control, we have also run simulation with the initial excitation on CT and find nearly identical results as those in Figure 8.4d.

Figure 8.5 shows the rise of the ME population calculated with different electronic dephasing rates Γ_{ij}. The nearly instantaneous rise time of ME depends solely on the value of the electronic couplings W_{ij} whereas the longer time dynamics are determined by the dephasing rate. For a smaller $\hbar\Gamma_{ij}$ (10 meV), we see a weaker damping of the coherent oscillation. In the case of tetracene, singlet fission is an endothermic process with both E_{ME} and E_{CT} higher than E_{S1}; as the population of CT and ME states increases, the total energy of the electronic subsystem changes. In eq 4, this energy change is accomplished through coupling to the environment via the dephasing term Γ_{ij}. For small Γ_{ij}, the rise time of ME population is limited by the slow energy exchange between the system and the environment. For larger Γ_{ij}, the dephasing process becomes approximately resonant with the electronic transitions and the rise time is determined only by the electronic coupling constants.

We now consider the microscopic origins of the dephasing rates and rigorously derive the density matrix dynamics in eq 4 using techniques from quantum relaxation theory. Specifically, the density matrix ρ should be understood as the reduced density matrix obtained by averaging over microscopic environmental degrees of freedom. This statistical reduction is the physical origin for the phenomenological dephasing and relaxation processes. In this approach, one begins with an extended Hamiltonian,

$$\hat{H} = \hat{H}_{ME} + \hat{H}_{B} + \hat{H}_{ME-B} \tag{8}$$

which comprises the electronic, the environmental bath, and the interaction between the two. Under the assumption of bilinear coupling to a bath of phonons,[30] the effects of the environment can be completely characterized by the so-called spectral density,

$$J_i(\omega) = \frac{\pi}{2}\sum_k \frac{C_{k,i}^{\ 2}}{\omega_k}\delta(\omega - \omega_k) \tag{9}$$

where $c_{k,i}$ quantifies the coupling between energy level i and the phononmode with frequency ω_k. For conjugated organic chromophores, like tetracene and pentacene, the spectral density is peaked at the well-known vibronic progression frequency of ~1450 cm ± 1.34 The quantitative structure of $J(\omega)$ can be determined by a combination of classical molecular dynamics and quantum chemistry calculations,[38] which can be used to parametrize common functional forms of the spectral density. By performing a dynamical perturbation theory to second order in the electron-phonon interaction, and employing the secular and Markov approximations, one arrives at the well-known Redfield theory equation of motion,[39,40]

$$i\hbar\frac{\partial\hat{\rho}}{\partial t} = \left[\hat{H}_{ME}, \hat{\rho}\right] - i\hbar\hat{R}\hat{\rho} \tag{10}$$

The Redfield tensor is a four-index quantity, $\hat{R}_{ijkl}$, describing population relaxation and coherence dephasing induced by the environment at temperature *T*, and can be shown to produce a Boltzmann-distributed steady-state reduced density matrix,

$$\hat{\rho}(t \to \infty) = \hat{\rho}_0 = Z_{ME}^{-1} \exp(-\hat{H}_{ME} / k_B T) \tag{11}$$

While the Redfield theory equation of motion takes the same general form as eq 4, the rates composing the Redfield tensor $\hat{R}$ have explicit microscopic expressions depending on both the system and bath degrees of freedom. These expressions, in addition to being unbiased and more general than phenomenological constants, can also provide valuable physical insight. For example the population relaxation elements, in the electronic eigenstate basis that diagonalizes $\hat{H}_{ME}$, are given by the expressions

$$R_{\alpha\alpha\beta\beta} = C_{\alpha\beta} J(\omega_{\alpha\beta}) n_{BE}(\omega_{\alpha\beta}) \tag{12}$$

$$R_{\beta\beta\alpha\alpha} = C_{\alpha\beta} J(\omega_{\alpha\beta}) [n_{BE}(\omega_{\alpha\beta}) + 1] \tag{13}$$

where $\omega_{\alpha\beta} = (E_\alpha - E_\beta)/\hbar$ is assumed positive, $C_{\alpha\beta}$ is a constant determined by the diagonalizing transformation, and $n_{BE}(\omega) = [\exp(\hbar\omega / k_B T) - 1]^{-1}$ is the Bose-Einstein distribution. Equation 10 demonstrates that the population transfer rate between two states is proportional to the density of phonon modes at their energy difference and the probability that those modes are thermally occupied. Physically, the electronic subsystem is thermalized by the absorption and emission of phonons. The use of constant, uniform dephasing rates in the previous section is somewhat akin to an infinite temperature assumption, and thus the population dynamics overestimate the effects of entropy. Although such an analysis sheds light on the important role entropy can play when

transitioning from molecular dimers to bulk materials, ultimately the finite-temperature formalism presented above should be preferred as it correctly interpolates between the energetically and entropically dominated regimes, guaranteeing a steady-state Boltzmann distribution. When such finite temperature rates are used, we have shown in pentacene that a CT-mediated superexchange mechanism becomes a viable singlet fission pathway.[31] In this regime, the electronic excitation quantum mechanically tunnels through virtual CT states in passing from S_1 to ME. Our superexchange result is robust even in the presence of very high CT state energies.

To demonstrate this formalism, we consider a simple three-state model Hamiltonian comprising the S_1, CT, and ME states for a pentacene dimer. We neglect the direct S_1 to ME coupling and choose the remaining coupling values $W_{S1\text{-}CT} = W_{CT\text{-}ME} = 50$ meV, in accord with the calculations presented in section 8.4. The energy detuning values are chosen to be representative of a pentacene dimer, $E_{S1}\text{-}E_{TT} = 200$ meVand $E_{CT}\text{-}E_{TT} = 300$ meV.[20,21,30,41] In Figure 8.6, we show the population dynamics of the three states as calculated by the Redfield master equation, for an initially excited S_1 state. Overall, we see that highly efficient fission occurs in 100 fs and the negligible CT population in panels (a) and (b) is characteristic of a superexchange mechanism proceeding through virtual CT states.[30,31] As explained above, the relaxation rates are largely determined by the spectral density, which we take to be of the ohmic form, $J(\omega) = 2\lambda\Omega\omega/(\omega^2+\Omega^2)$, with reorganization energy $\lambda = 100$ meV and characteristic bath frequency $\hbar\Omega = 180$ meV (1450 cm ± 1). In Figure 8.6d, we plot the spectral density along with the three electronic eigenvalue energy differences, showing the strong overlap, which means that there are

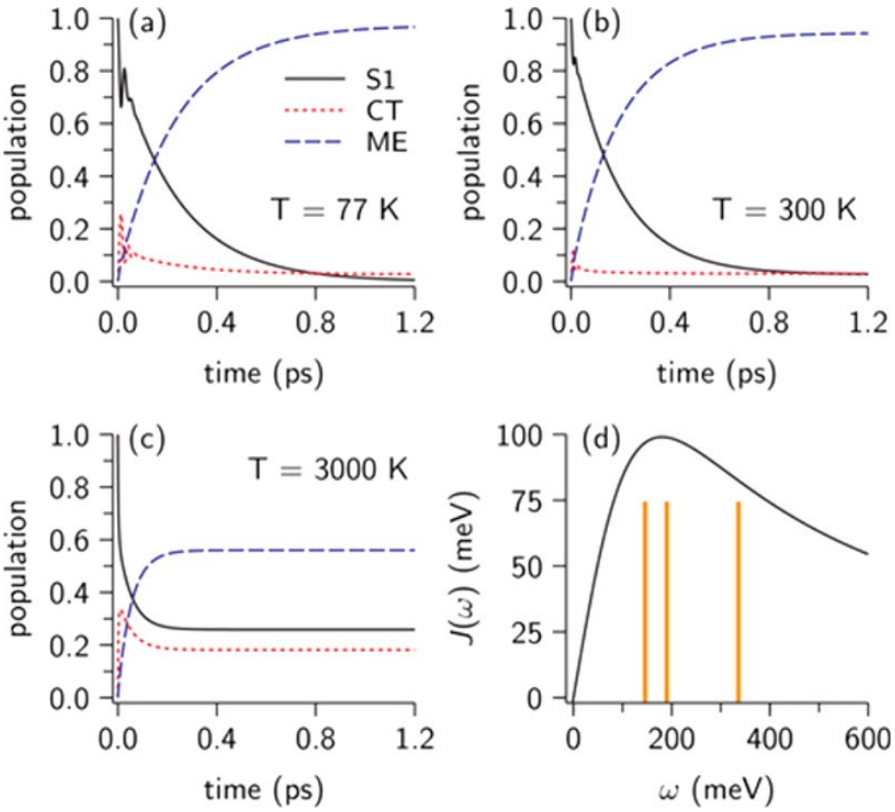

Figure 8.6 Population dynamics of the S_1, CT, and ME states as calculated by the Redfield quantum master equation for a pentacene dimer. Dynamics are calculated at the three temperatures indicated in panels (a)–(c). Panel (d) shows the bath spectral density employed along with the three transition energy differences of the electronic Hamiltonian.

many available phonons to supply or remove the required excess energy. The additional temperature dependence of the rates is depicted in panels (a)-(c), showing that the fission is largely temperature independent until very high temperatures, at which point the rate increases and the steady state population becomes more equally distributed. Such temperature-dependent studies are clearly only accessible via a master equation whose rates obey detailed balance, eq 10.

The ~100 fs rise time for the ME population calculated above from the master equation is longer than the ≤20 fs time determined from 2PPE experiments in Figure 8.1b

and d. One limitation of the calculation may be attributed to the reduced density-of-states of a dimer; work is currently underway to extend this treatment to larger clusters and crystals. Another possibility may be the approximate nature of equating photoemission intensities to state populations. As another future research direction, we plan to extend our density matrix dynamics to include the photoionization step for a more direct comparison with TR-2PPE experiments.

8.6 Conclusions

We present our understanding of singlet fission dynamics in organic semiconductors. Recent measurements by time-resolved two-photon photoemission spectroscopy in crystalline pentacene and tetracene have provided an experimental foundation for the quantum coherent mechanism in singlet fission. However, calculations based on multistate density functional theory showed that the direct electronic coupling between singlet and multiexciton states is too weak to explain the ultrafast formation of multiexciton states observed in experiment. Instead, indirect coupling via charge transfer intermediate states are 2 orders of magnitude stronger. Density matrix modeling with the calculated coupling matrix elements involving singlet, charge transfer, and multiexciton states for the crystalline tetracene lattice satisfactorily accounts for the experimental observation. This modeling reveals the critical roles of the intermediate charge transfer states, the high density of states in the multiexciton manifold, and the environmental dephasing processes in ensuring the ultrafast formation of multiexciton states. We address the origins of microscopic relaxation and dephasing rates and adopt such rates in a quantum master equation description, which yields encouraging results that are in

qualitative agreements with experimental findings on singlet fission. These successful approaches motivate us to take the theoretical effort one step further in the near future by marrying high-level electronic structure calculations with accurate quantum relaxation dynamics for realistic system sizes.

Chapter 9. Free Energy Surfaces of Electron Transfer in Condensed Phase

9.1 Introduction

To demonstrate the accuracy of using multistate density functional theory (MSDFT) in QM/MM molecular dynamics simulations, a simple electron transfer (ET) system is modeled in condensed phase. Here, the MSDFT method[29,37] is used with the self-consistent charge density functional tight-binding method (SCC-DFTB or DFTB)[144] in free energy simulations of the $Fe^{+2}(H_2O)_6/Fe^{+3}(H_2O)_6$ ion pair solvated by explicit water molecules. The electron transfer between the Fe^{+2}/Fe^{+3} electron transfer system has been extensively studied experimentally and computationally.[145–148] It is chosen here to illustrate the capability of MSDFT for studying non-adiabatic electron transfer and for determining solvent reorganization energy using explicitly an electronic structure theory in molecular dynamics simulations. Free energy surfaces for electron-localized diabatic states are computed from the potential of mean force as a function of the energy gap between diabatic states.[37]

9.2 Methodology

The MSDFT method has been implemented into the molecular simulation package CHARMM[149,150] to carry out QM/MM molecular dynamics simulations, where the QM region is treated by MSDFT-DFTB,[1,3,6,7] the bulk solvent is treated by the CHARMM force field potential energy function parameterized for the $Fe^{+2}(H_2O)_6/Fe^{+3}(H_2O)_6$ system. The QM/MM interaction Hamiltonian explicitly includes polarization of the QM electron density by MM point charges. Based on the electron-localized reactant and product diabatic states of Marcus theory,[51] the QM region is

characterized by a set a block-localized Kohn-Sham (BLKS) functions, each defined by a valence bond (VB) structure

$$Fe^{+2}(H_2O)_6 \cdots Fe^{+3}(H_2O)_6; \quad \Psi_0^{BLKS} = \hat{A}\{\Omega_0^1(Fe^{+2}(H_2O)_6)\Omega_0^2(Fe^{+3}(H_2O)_6)\} \tag{1}$$

$$Fe^{+3}(H_2O)_6 \cdots Fe^{+2}(H_2O)_6; \quad \Psi_1^{BLKS} = \hat{A}\{\Omega_1^1(Fe^{+3}(H_2O)_6)\Omega_1^2(Fe^{+2}(H_2O)_6)\} \tag{2}$$

where the electron-localized reactant and product states are indicated by 0 and 1, respectively. The coupling between these diabatic states gives the delocalized adiabatic ground and excited states, which are given as solutions of the following secular equation

$$\begin{vmatrix} H_0 - \varepsilon_g & H_{01} - S_{01}\varepsilon_g \\ H_{01} - S_{01}\varepsilon_g & H_0 - \varepsilon_g \end{vmatrix} = \mathbf{0} \tag{3}$$

where $H_{ij} = \left\langle \Psi_i^{BLKS} \middle| \hat{H} \middle| \Psi_j^{BLKS} \right\rangle$ and $S_{ij} = \left\langle \Psi_i^{BLKS} \middle| \Psi_j^{BLKS} \right\rangle$ for $i,j = 0,1$ and ε_g is the lowest energy root to the secular equation (i.e. the adiabatic ground state energy). The electronic coupling (V_{el}) between states 0 and 1 is defined as the off-diagonal element

$$V_{el} = \left| H_{01} - S_{01}\varepsilon_g \right|. \tag{4}$$

Free energy surfaces of the diabatic and adiabatic states are computed from the potential of mean force using free energy perturbation methods.[37,151] The reaction coordinate is defined as the energy difference between diabatic states

$$X^S = E_0(\Psi_0^{BLKS}) - E_1(\Psi_1^{BLKS}) = \left\langle \Psi_0^{BLKS} \middle| \hat{H} \middle| \Psi_0^{BLKS} \right\rangle - \left\langle \Psi_1^{BLKS} \middle| \hat{H} \middle| \Psi_1^{BLKS} \right\rangle \tag{5}$$

which takes into account solvent fluctuations, indicated by the superscript *S*. To ensure sufficient sampling along the reaction coordinate, especially within the transition state region, a reference potential is used, defined as

$$V_{RP}(\lambda) = (1-\lambda)E_0(\Psi_0^{BLKS}) + \lambda E_1(\Psi_1^{BLKS}). \tag{6}$$

where the coupling parameter (λ) is varied from 0 to 1 in small increments. By running a set molecular dynamics simulations, each at a given value of λ, the entire reaction coordinate is sampled. However, the relative free energy is computed as a function of the coupling parameter λ

$$\Delta G_{RP}(\lambda) = -RT\sum_{i=0}^{1}\ln\left\langle \exp-[V_{RP}(\lambda_{i+1}) - V_{RP}(\lambda_i)]/RT\right\rangle_i \qquad (7)$$

where λ_i is an incremental value of λ from 0 to 1 and $\langle\cdots\rangle_i$ indicates an ensemble average of configurations with a given value of λ_i. The relative free energy for the reactant state is defined to be zero, $\Delta G_{RP}(0) = 0$. To obtain the relative free energy as a function of the reaction coordinate, X^S, an umbrella sampling technique is used to compute the probability that the reference potential at a given value of λ_i samples configurations within a small window of reaction coordinate values. The relative free energy of the adiabatic ground state is then computed as a function of the reaction coordinate X^S

$$\Delta G(X^S) = \Delta G_{RP}(\lambda_i) - RT\ln\left\{\rho^i_{RP}(X^S)\left\langle \exp-[V_g(X^S) - V_{RP}(\lambda_i)]/RT\right\rangle_i\right\} \qquad (8)$$

where $\rho^i_{RP}(X^S)$ is the normalized distribution of configurations with a given value of X^S sampled using the reference potential $V_{RP}(\lambda_i)$. The diabatic free energy surfaces are computed using the same approach, where V_g in eq 8 is replaced by E_0 or E_1 for the reactant and product diabatic states, respectively.

9.3 Computational Details

Electron transfer between an Fe^{+2}/Fe^{+3} ion pair solvated by explicit water molecules is modeled using MSDFT QM/MM molecular dynamics. The QM region consists of the ion pair and twelve water molecules, $Fe^{+2}(H_2O)_6/Fe^{+3}(H_2O)_6$, and is

treated with MSDFT using the SCC-DFTB (or DFTB) method.[144,152,153] Unlike other semiempirical methods based on the neglect of diatomic differential overlap (NDDO) approximation, DFTB properly treats the overlap between non-orthogonal diabatic states (S_{ij}), important in the MSDFT formalism.

The QM region is solvated by 2018 water molecules using the TIP3P water model[154] and five chlorine ions modeled by the CHARMM27 force field.[155,156] A cubic box with a box length of 38 Å was used to set up periodic boundary conditions. Non-bonded potential energy terms were computed using a cutoff distance of 15.0 Å and a switching function between 11.0 and 13.0 Å. The Nosé-Hoover thermostat[157,158] was used to run NPT dynamics at T = 298.15 K and P = 1.0 atm. After 10 ps of equilibration, 100 ps of molecular dynamics were carried out using a timestep of 1 fs, the leap-frog Verlet algorithm,[159,160] and the SHAKE algorithm[161] to constrain all hydrogen distances. Three Fe-Fe distances, 6.0, 8.0, and 10.0 Å, were modeled using a harmonic potential to constrain the Fe-Fe distance. Due to symmetry, free energy surfaces were computed for the reactant side of the reaction coordinate and reflected about X^S = 0.5 to obtain the entire reaction coordinate. All QM/MM simulations were performed using a local version of CHARMM.[149,150]

9.4 Results and Discussion

Free energy surfaces are shown as a function of the reaction coordinate (X^S) for Fe-Fe distances 6.0, 8.0, and 10.0 Å in Figures 9.1 – 9.3. Several key properties of the well-known Marcus theory[51] of ET are reproduced by MSDFT-DFTB QM/MM molecular dynamics simulations. The adiabatic surface is well-represented by the diabatic

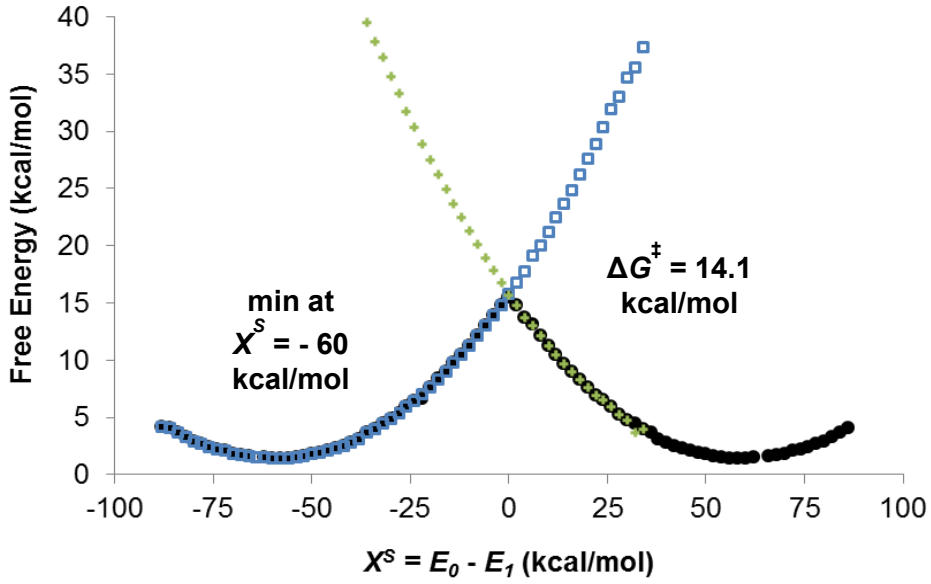

Figure 9.1 Adiabatic (black closed circles) and electron-localized reactant (blue open squares) and product (green closed diamonds) diabatic states of electron transfer in $Fe^{+2}(H_2O)_6/Fe^{+3}(H_2O)_6$ at an Fe-Fe distances of 6.0 Å.

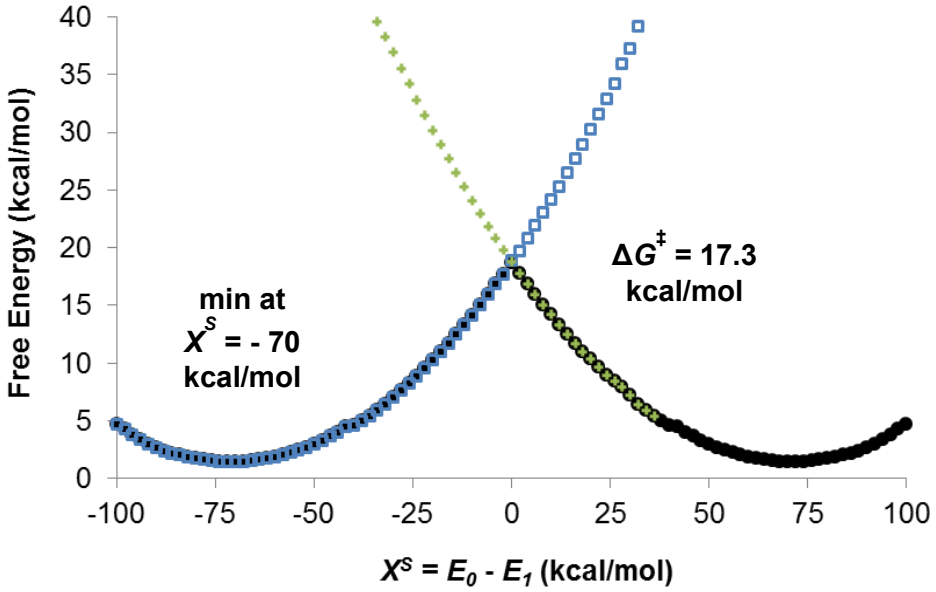

Figure 9.2 Adiabatic (black closed circles) and electron-localized reactant (blue open squares) and product (green closed diamonds) diabatic states of electron transfer in $Fe^{+2}(H_2O)_6/Fe^{+3}(H_2O)_6$ at an Fe-Fe distances of 8.0 Å.

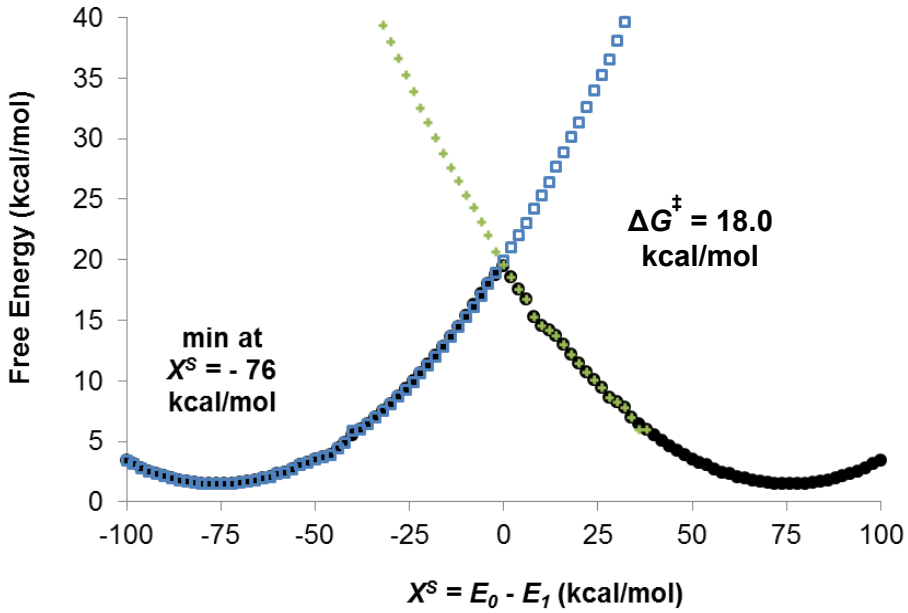

Figure 9.3 Adiabatic (black closed circles) and electron-localized reactant (blue open squares) and product (green closed diamonds) diabatic states of electron transfer in $Fe^{+2}(H_2O)_6/Fe^{+3}(H_2O)_6$ at an Fe-Fe distances of 10.0 Å.

reactant and product states along a majority of the ET coordinate, except for a very small window near the diabatic state crossing point ($X^S = 0.0$), where non-adiabatic coupling leads to "surface hopping" and the diabatic state switches electronic character from Ψ_0^{BLKS} to Ψ_1^{BLKS}.

Several properties have a strong dependence on the Fe-Fe distance, as predicted by Marcus theory of ET. As the Fe-Fe distance increases, the minimum of the reactant diabatic state surface shifts to more negative X^S values while the product state shifts to more positive X^S values. This is accompanied by an increase in the adiabatic free energy barrier ($\Delta G^{\ddagger}$) and the solvent reorganization energy (λ_S). On the other hand, separation of the donor-acceptor sites significantly reduces the electronic coupling (V_{el}) (Table 9.1).

Table 9.1 Distance dependence of X^S at diabatic state minima (min X^S), free energy barrier ($\Delta G^{\ddagger}$), reorganization energy (λ_S), electronic coupling (V_{el}), and rate of electron transfer (k_{ET}).

Fe-Fe Distance (Å)	min X^S (kcal/mol)	$\Delta G^{\ddagger}$ (kcal/mol)	λ_S (kcal/mol)	V_{el} (kcal/mol)	k_{ET} (s^{-1})
6.0	± 60.0	14.1	65.8	6.32×10^{-1}	1.46×10^{1}
8.0	± 70.0	17.3	69.7	1.76×10^{-2}	5.76×10^{-2}
10.0	± 76.0	18.0	75.7	7.60×10^{-4}	1.27×10^{-3}

Table 9.2 Distance dependence of the average overlap integral as a function of X^S.

X^S (kcal/mol)	$\sqrt{\langle S_{01}^2 \rangle} \times 10^{-5}$ R = 6.0 Å	$\sqrt{\langle S_{01}^2 \rangle} \times 10^{-7}$ R = 8.0 Å	$\sqrt{\langle S_{01}^2 \rangle} \times 10^{-8}$ R = 10.0 Å
0	9.12	5.56	2.35
- 10	8.50	4.9	2.73
- 20	8.02	5.89	2.23
- 30	7.57	5.89	2.15
- 40	7.96	6.92	1.96
- 50	7.55	4.83	2.69
- 60	7.55	5.83	1.3
- 70	8.46	7.17	1.54
- 80	7.89	5.05	1.26

Figure 9.4 illustrates the distance dependence of $\sqrt{\langle V_{el}^2 \rangle}$, where <···> indicates a statistical average over configurations in a given bin designated by X^S. Contributing to the distance-dependence of V_{el}, the overlap integral (S_{01}) displays similar distance

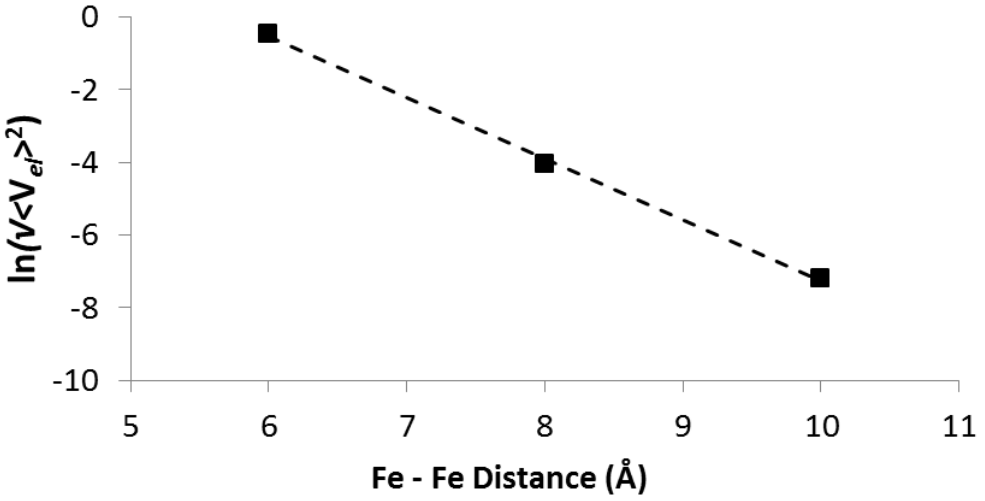

Figure 9.4 Distance dependence of the average electronic coupling $\sqrt{\langle V_{el}^2 \rangle}$ at $X^S = 0.0$ kcal/mol. The slope of the linear fit is 1.68 Å^{-1} and is equivalent to $\beta/2$, where β is the distance decay value ($\beta = 3.36$ Å^{-1}).

dependence (Table 9.2). It is also noted that the average overlap integral $\sqrt{\langle S_{01}^2 \rangle}$ increases near the transition state at $X^S = 0.0$ kcal/mol, where "surface hopping" is expected to occur due to increased electronic coupling.

These distance-dependent factors contribute to the rate of electron transfer (k_{ET}), expressed as

$$k_{ET} = \frac{1}{h} \frac{1}{\sqrt{4\pi\lambda_S k_B T}} \langle V_{el}^2 \rangle \exp\left(\frac{(\Delta G° + \lambda_S)^2}{4\lambda_S k_B T} \right) \quad (9)$$

where h is the Planck constant, k_B is the Boltzmann constant, and $T = 298$ K. The rate of electron transfer has a strong dependence on the Fe-Fe distance (Table 9.1). Computed from the slope of Figure 9.4, a relatively large distance decay constant ($\beta = 3.36$ Å^{-1}) reflects this strong dependence.

9.5 Conclusions

These results demonstrate the accuracy of MSDFT-DFTB in QM/MM molecular dynamics simulations for modeling electronically non-adiabatic ET. The free energy barrier is shown to increase with increasing donor-acceptor distance, as predicted by Marcus theory, while the electronic coupling and rate of electron transfer decease. The current approach can be applied to enzymatic ET reactions. To model condensed phase PCET reactions, a geometrically-defined PT coordinate, such as the difference in bond length between the transferring proton and its donor and acceptor sites $\Delta R_p = R_{DH} - R_{HA}$ can be used to define a two-dimensional sampling space. In practice, this may be done by introducing a harmonic constraint on the PT donor and acceptor atoms to sample a given PT coordinate value. The free energy simulations sampling along the ET coordinate, as described above, would then be repeated for each distance along the PT coordinate. The resulting two-dimensional free energy surface would be analogous to the three-dimensional More O'Ferrall-Jencks diagrams discussed in Chapters 4 and 5, with the exception that the ET coordinate is defined in terms of the diabatic state energy gap. Validation of the MSDFT-DFTB QM/MM method for sampling the ET coordinate through free energy simulations is one step closer to explicitly modeling diabatic states of enzymatic PCET reactions in a solvated protein environment.

Chapter 10. Electrostatic and Dynamical Effects on Hydride Transfer Catalyzed by Dihydrofolate Reductase (DHFR)

10.1 Introduction

The role of protein dynamics in enzyme catalysis continues to be a topic of debate.[22,23,162–164] In general, it is accepted that conformational changes induced by the binding of substrates and/or cofactors enhance catalysis. However, these motions are assumed to be decoupled from the reaction mechanism of catalysis in that the enzyme-substrate complex (i.e. Michaelis complex) reaches an equilibrium distribution before the reaction occurs.[23] In recent years, particular attention has been paid to the dynamical motions of the Michaelis complex that occur within the same time-frame as the catalytic reaction. A prime example is the role of local fluctuations of a loop structure near the active site of dihydrofolate reducatse (DHFR),[40,42,165–168] an enzyme responsible for catalyzing hydride transfer between nicotinamide adenine dinucleotide phosphate (NADPH) and 7,8-dihydrofolate (DHF) to form 5,6,7,8-tetrahydrofolate (THF). It has been suggested that the dynamic flexibility of the M20 loop is essential for hydride transfer catalysis based on the reduced catalytic activity of N23PP/S148A substituted DHFR and the concomitant reduction in its dynamic flexibility within the M20 loop residues.[169] However, arguments have been made against this claim, stating that the increased electrostatic reorganization energy required for catalysis in the mutant variant is responsible for the reduced catalytic activity.[170] Despite a wealth of experimental and computational data on this catalytic reaction, the role of protein dynamics has yet to be resolved.

10.2 Background Information

Given the ubiquitous nature of proton-coupled electron transfer (PCET) reactions in enzyme-catalyzed processes, it is essential to understand the effects of protein dynamics on the potential energy surface, especially with respect to the donor and acceptor sites of electron transfer and proton transfer.[56,163] Protein motions can vary on a time-scale of femtosecond bond vibrations, picosecond to nanosecond local structural fluctuations, and millisecond to second conformational motions.[23] These motions also vary in how they relate to the chemically-relevant step(s) of a reaction mechanism. Certain "rate-promoting vibrations" may be inherently coupled to the reaction coordinate such that quenching of the motion prevents catalysis.[164] Alternatively, protein motions, large or small, may sample an ensemble of configurations that avoids low-energy local minima, thus maintaining a reasonable barrier height for catalysis.[23] Still another view proposes that the active site must be reorganized to reach an optimal transition state structure in which the chemical step occurs.[171] This is akin to Marcus theory of electron transfer[51] in that the solvent reorganization term accounts for the adjustment of the surrounding environment to come into equilibrium with the current electronic state of the system.[172,173]

Central to the discussion of a functional role of protein motions within an enzyme-catalyzed reaction mechanism is the catalysis of hydride transfer by DHFR. Crystallographic evidence suggests that the local conformation of the M20 loop of wt-DHFR changes based on the catalytic cycle.[40] Site-directed mutagenesis studies in which M42 and G121 are replaced by a tryptophan and valine residue, respectively, reported

reduced hydride transfer rates and coupled protein motions outside of the active site.[165,174] Previous work by our group on this double mutant variant of DHFR (dm-DHFR) provides computational evidence of an increased free energy barrier due to reduced dynamic flexibility of the M20 loop in the transition state structure of dm-DHFR compared to wt-DHFR. Furthermore, the increased barrier originates from an overall reduction in $\Delta S^{\ddagger}$ in the dm-DHFR transition state compared to the wt-DHFR transition state ensemble. Lastly, the stabilized closed structure of the M20 loop in dm-DHFR at the transition state is attributed to a third hydrogen bond that is absent in the wt-DHFR transition state structure.

Motivated by the electrostatic reorganization argument of catalytically impaired DHFR mutants,[168,170] the electrostatic environment of the active site of wt-DHFR has been probed experimentally using a deuterium-substituted Y_{100} residue ($[D_4]Y_{100}$).[41] Reported infrared (IR) spectra indicate a shift in hydrogen bonding of the $[D_4]Y_{100}$ residue for different model complexes of substrate- and cofactor-bound complexes of wt-DHFR (Figure 10.1). Both the apoenzyme (DHFR) and holoenzyme (NADPH:DHFR) are characterized by two peaks within the C-D stretching frequency range (2200 to 2300 cm^{-1}). It is assumed that two of the four C-D stretching modes overlap or are too low in intensity to be observed experimentally. The model complex of the Michaelis complex (folate:$NADP^+$:DHFR) displays a third peak at slightly higher frequency, but the strong peak near 2240 cm^{-1} retains a similar intensity as the apoenzyme and NADPH:DHFR complex. The transition state is modeled by a MTX/NADPH-bound enzyme[40] (MTX:NADPH:DHFR) and is remarkably similar to the apoenzyme and the

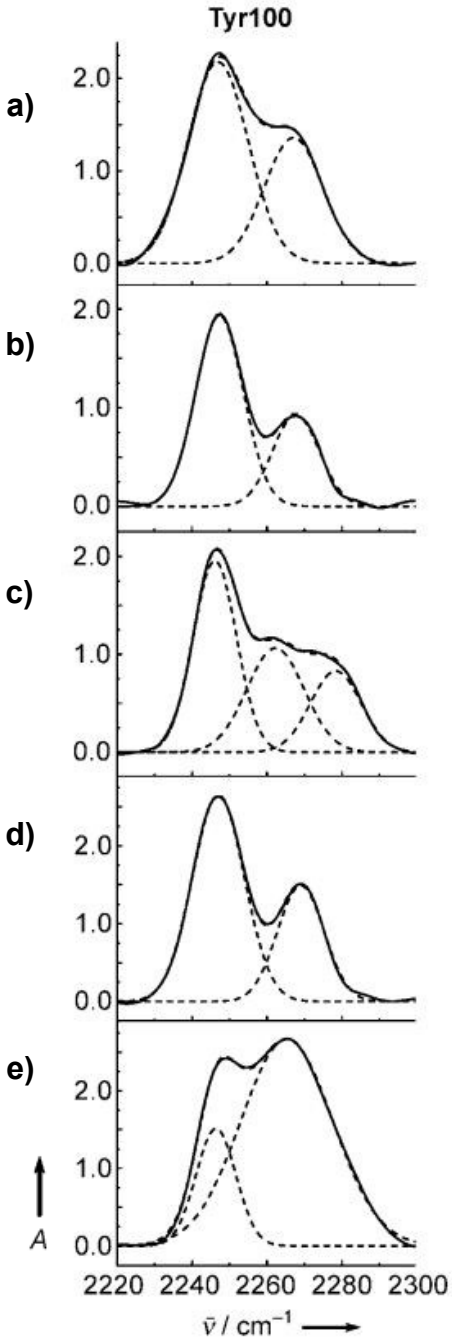

Figure 10.1 IR spectra and fits of $[D_4]Y_{100}$ in a) Apo DHFR, b) NADPH complex, c) folate/NADP+ complex, d) MTX/NADPH complex, and e) folate complex. Reprinted with permission from Groff, D.; Thielges, M. C.; Cellitti, S.; Schultz, P. G.; Romesberg, F. E. Angew. *Chem. Int. Ed.* **2009** *48*, 3478. Copyright 2009 Wiley-VCH Verlag GmbH & Co. KGaA, Weinheim.

NADPH:DHFR complex spectra. Lastly, the product state experimental IR spectra, modeled by the folate-bound enzyme (folate:DHFR), shows the most significant changes with a large increase in the intensity of the higher-frequency mode along with broadening of this peak. Compared to IR spectra of isolated [2,3,4,5-D_4]tyrosine in basic and acidic condictions, this is consistent with deprotonation of the tyrosine residue. It is suggested that the change in C-D IR spectra originates from the strength of the hydrogen bond of the –OH group. Additionally, the unique spectrum of the MTX:NADPH:DHFR complex is proposed to represent a population of a unique set of conformations, similar to a transition state. Here, we investigate the origin of these IR spectra with respect to changes in the dynamical fluctuations and electrostatic environment of the active site of DHFR. As described in the work of Corcelli, Cho, and co-workers,[45,175–177] molecular dynamics simulations are used to simulate IR spectra of wt-DHFR $[D_4]Y_{100}$ in the reactant, transition, and product states of hydride transfer between NADPH and DHF.

10.3 Methodology

As shown by Berens and Wilson,[44] the IR spectrum of a molecular system can be computed from the autocorrelation function of a time-dependent dipole moment calculated for a set of trajectory coordinates of molecular dynamics simulations. Using a semi-empirical QM/MM molecular dynamics approach the expectation values of the QM dipole moment operators ($\hat{\mu}_x$, $\hat{\mu}_y$, and $\hat{\mu}_z$) are computed for the side chain of $[D_4]Y_{100}$ at each MD step.[175] This provides a time-dependent dipole moment vector, $\vec{\mu}(t)$, for a given set of trajectory coordinates. The IR spectra is computed as the spectral density, $C(\omega)$, of the dipole moment autocorrelation function, $C(t)$, defined as

$$C(t) = \langle \vec{\mu}(t) \cdot \vec{\mu}(0) \rangle \tag{1}$$

where $\langle \cdots \rangle$ indicates an ensemble average. In practice, this is done by taking the fast Fourier transform of dipole moment autocorrelation function, converting the time-dependent data to the frequency (ω) domain

$$C(\omega) = FFT[C(t)] = \int_{-\infty}^{\infty} C(t) \exp(-i\omega t) dt \,. \tag{2}$$

10.4 Computational Details

Following previous procedures,[42,43] combined QM/MM molecular dynamics simulations are carried out using a potential developed for DHFR

$$U_{tot} = \langle \Psi(S) | H_{qm}^{\circ}(S) + H_{qm/mm}(S) | \Psi(S) \rangle + U_{mm} + V_{SVB} \tag{3}$$

where $H_{qm}^{\circ}(S)$ is the Hamiltonian of the QM region (S), $H_{qm/mm}(S)$ is the interaction Hamiltonian between the QM and MM regions, U_{mm} is the classical potential energy of the MM region, and V_{SVB} is a simple valence bond (SVB) parameter added to reproduce the experimental free energy of reaction. A semi-empirical AM1 Hamiltonian[178] parameterized for this reaction is used to treat the QM region and the QM/MM interactions, while the MM region is modeled by the CHARMM27 force field,[155] including parameters optimized for NADPH/NADP+ and DHF/THF.[42,43] The QM region is defined as shown in Figure 10.2, where generalized hybrid orbital boundary atoms (B) are used at the β-carbon of $[D_4]Y_{100}$ and the specified carbon atoms of NADPH and DHF.

Using periodic boundary conditions, a cubic box of dimensions of ~60 Å x ~60 Å x ~60 Å was used to solvate the DHFR complex. Histidine residues and all polar amino

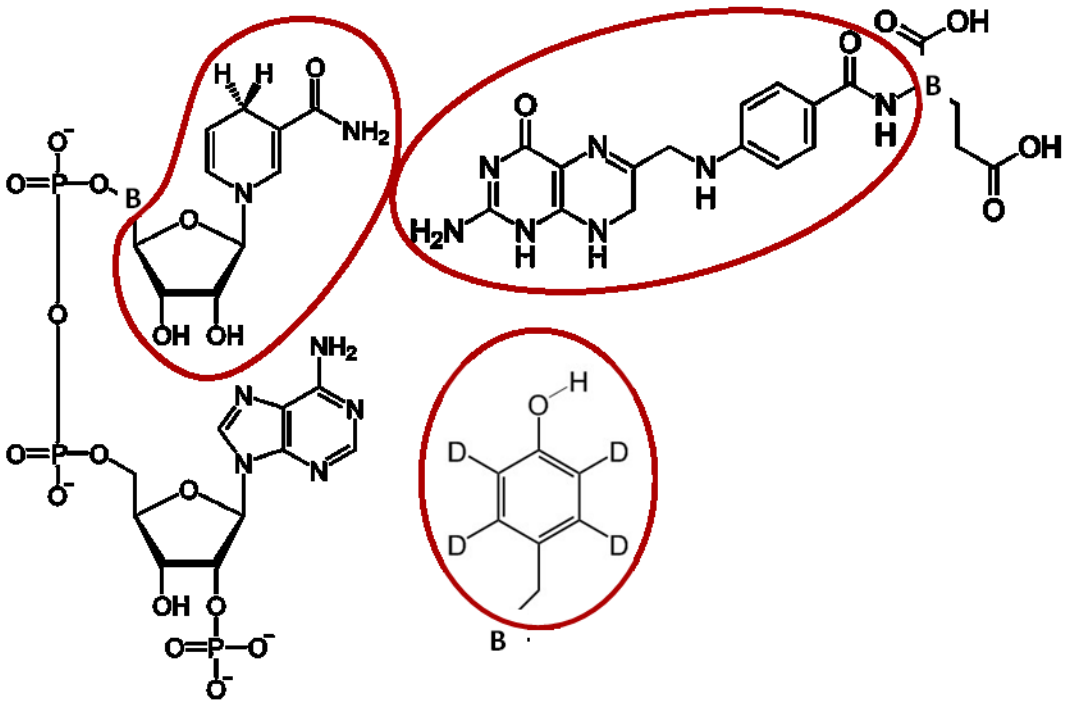

Figure 10.2 Schematic drawing of the QM/MM partitioning of atoms within the active site of wt-DHFR. Atoms circled in red are treated explicitly with a parameterized AM1 model. Boundary carbon atoms are indicated as **B**. All other atoms are treated classically.

acid side chains were protonated and deprotonated as needed to model a neutral solution of pH 7, resulting in 15 units of negative charge. These charges were neutralized by randomly placing 15 sodium ions in the water box. A spherical cutoff distance of 12 Å was used to compute non-bonded interactions where a switching function was used between 10.5 and 11.5 Å.

All QM/MM simulations employed the Nosé-Hoover thermostat[157,158] for NPT ensemble molecular dynamics at $T = 298.15$ and $P = 1.0$ atm. Using the leap-frog Verlet algorithm[159,160] molecular dynamics were carried out using a timestep of 1 fs and the SHAKE algorithm[161] to constrain all hydrogen bond distances in the MM region. Simulations of the reactant and transition states of the DHFR system were restarted from

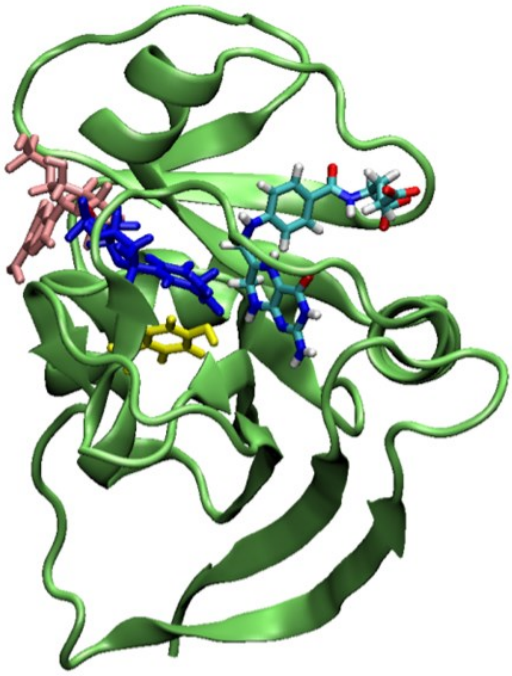

Figure 10.3 Active site configuration from the wt-DHFR reactant state simulation showing the protein backbone (green), NADPH (pink and blue), DHF (atomic coloring: C - cyan, N - blue, O - red, H - white), and $[D_4]Y_{100}$ (yellow).

previous QM/MM simulations[43] using the reference potential described above and a harmonic constraint to sufficiently sample transition state configurations. The initial structure of the wt-DHFR reactant configuration is shown in Figure 10.3, highlighting the relative orientations of the substrate, cofactor, and $[D_4]Y_{100}$ residue. The product state had not been previously modeled by QM/MM molecular dynamics. These simulations were started from a transition state structure where the transferring hydrogen was moved along a linear coordinate between the NADP donor atom and the DHF acceptor atom to a reasonable C-H bond distance (~1 Å). Using this starting structure, the product state was then equilibrated with a harmonic constraint on the QM atoms for 10 ps, at which point the harmonic constraint was removed and the system was equilibrated for an additional

100 ps. The reactant and transition state simulations were each run for a total simulation time of 4.6 ns, while the product state had a shorter simulation time of 3.2 ns.

As a reference, IR spectra of a single [2,3,4,5-D_4]tyrosine ([D_4]Tyr) in acidic and basic conditions are computed using QM/MM MD simulations and. Unless otherwise noted, the same simulation conditions used in the solvated protein complex simulations were used here. A water box of dimensions ~60 Å x ~60 Å x ~60 Å were used to solvate each residue, where a single sodium ion was randomly placed in the simulation box of the deprotonated (anionic) residue. Gaussian 09[139] using B3LYP/6-311+g(d,p) was used to optimize structures of the protonated and deprotoned [D_4]Tyr residues as input for the initial structures of the QM/MM simulations. The solvated systems were equilibrated for 10 ps and ran for a total simulation time of 1.8 ns each.

The QM dipole moment vector was computed for the [D_4]Y_{100} side chain every 4 fs of simulation time. Autocorrelation functions were computed for every 200 ps of simulation time, overlapped by 100 ps. Simulated spectra are plotted using a smoothing function with a bandwidth of 5 cm^{-1}. To remove mixing with rotational motions of the protein in the simulated IR spectra, the instantaneous dipole moment vectors were reoriented with respect to $\vec{\mu}(0)$ of each simulation. The same procedure was used to compute the reference spectra of isolated [D_4]Tyr. All calculations are performed using a locally modified version of CHARMM.[149,150]

10.5 Results and Discussion

10.5.1 Comparison of Simulated IR Spectra to Experiment

Experimental spectra of isolated [D_4]Tyr show two resolved peaks in the 2200-

2300 cm^{-1} range (Figure 10.4). In basic conditions, the relative amplitudes of the peaks shift to favor the high-frequency mode. Simulated spectra of isolated [D_4]Tyr have peaks within the 2300-2400 cm^{-1} range (Figure 10.5). Protonated [D_4]Tyr is characterized by two peaks, while deprotonation results in a third peak at higher frequency and a significant increase in peak intensity. These simulated IR spectra reproduce the experimental trend of favoring higher-frequency modes on going from protonated to deprotonated [D_4]Tyr.

Simulated IR spectra of the [D_4]Y_{100} residue of wt-DHFR in the reactant, transition state, and product states are shown in Figure 10.6. The reactant state is

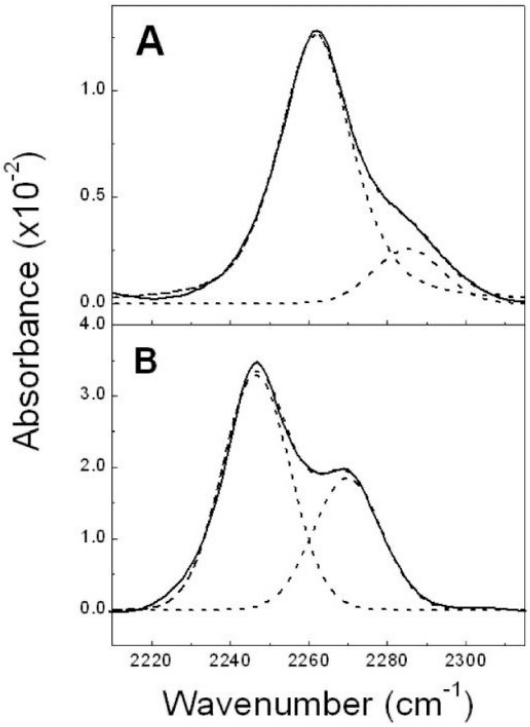

Figure 10.4 IR spectra and fits of [2,3,4,5-D_4]Tyr in a) 1.0 N HCl and b) 1.0 N NaOH. Reprinted with permission from Groff, D.; Thielges, M. C.; Cellitti, S.; Schultz, P. G.; Romesberg, F. E. Angew. *Chem. Int. Ed.* **2009** *48*, 3478. Copyright 2009 Wiley-VCH Verlag GmbH & Co. KGaA, Weinheim.

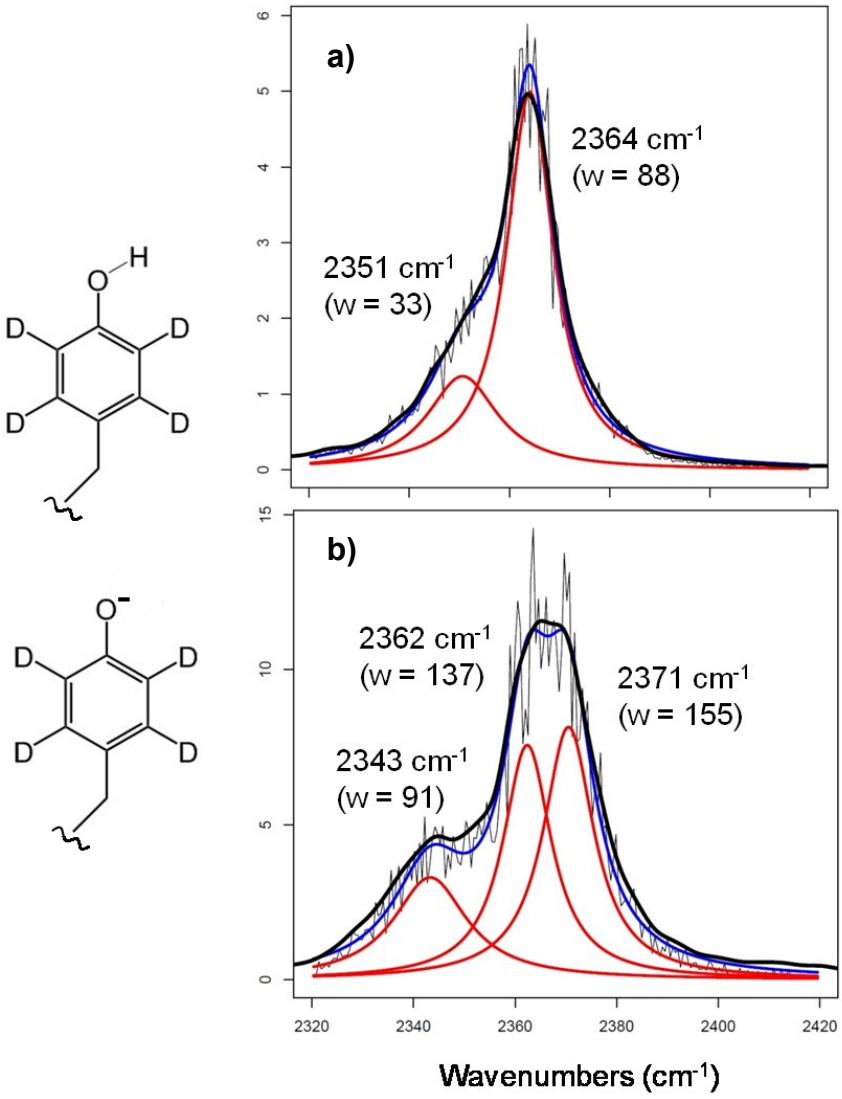

Figure 10.5 Similated IR spectra of a) protonated and b) deprotontated isolated [2,3,4,5-D_4]tyrosine in the C-D stretch frequency range.

characterized by a strong, narrow peak near 2360 cm^{-1}. Progression along the reaction coordinate to the transition state results in widening of this peak and a 5 cm^{-1} shift to higher frequency. The product state shows the most dramatic change with the addition of a second strong peak at about 10 cm^{-1} higher-frequency than the first. The overall trend

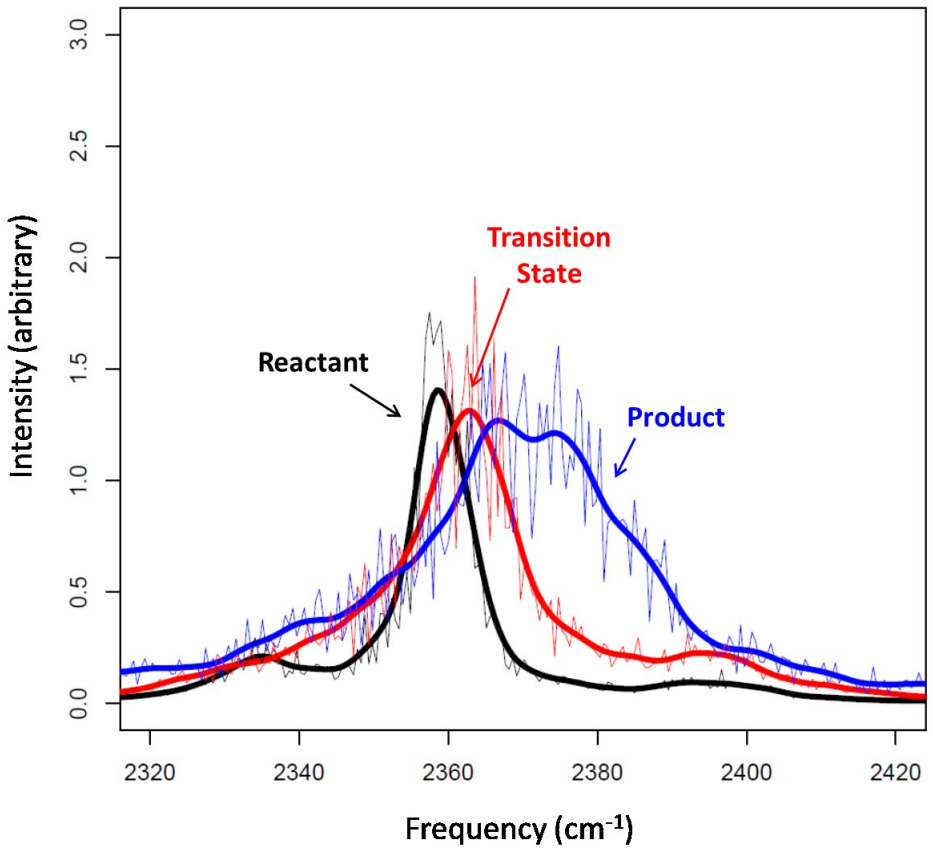

Figure 10.6 Similated IR spectra of $[D_4]Y_{100}$ in the reactant (black), transition state (red), and product (blue) state of wt-DHFR hydride transfer catalysis in the C-D stretch frequency range.

along the reaction coordinate indicates that hydride transfer between NADPH and DHF results in a more deprotonated $[D_4]Y_{100}$ residue, suggesting a stronger hydrogen bond to a neighboring residue or water.

10.5.2 Electrostatic Effects on Simulated IR Spectra

To investigate the origin of the shift in the $[D_4]Y_{100}$ IR spectrum, the electrostatic contribution of the bulk solvent and protein were analyzed, in addition to the electronic effects of the NADPH and DHF molecules. An effective gas-phase spectrum is computed by setting the MM charges of all atoms to zero, including the NADPH and DHF

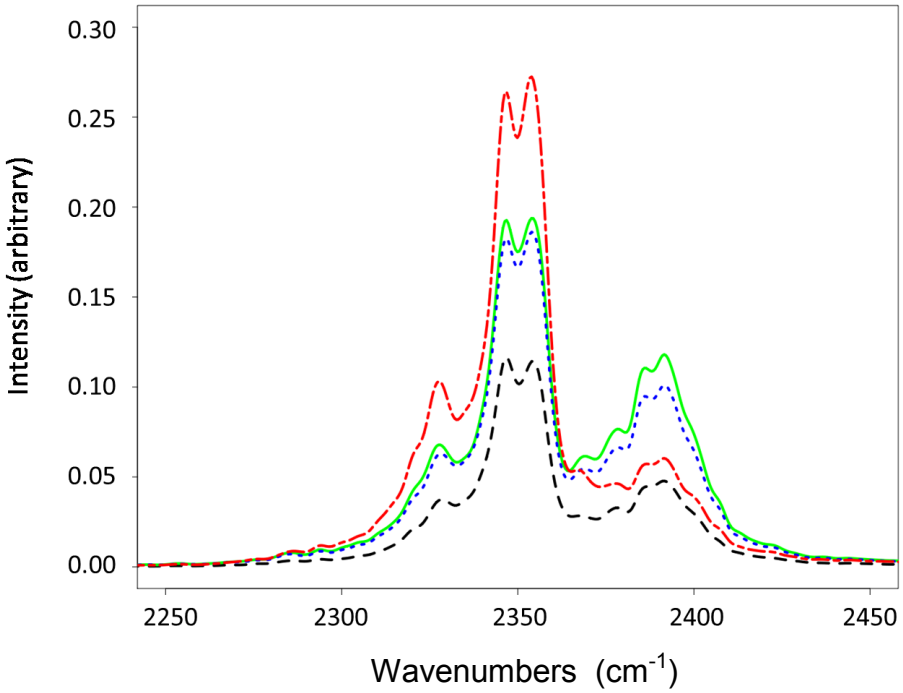

Figure 10.7 Similated IR spectra of $[D_4]Y_{100}$ in the reactant state of wt-DHFR hydride transfer catalysis. Electrostatic charges have been removed to model the gas phase (black dashed line), the solvent and protein environment (excluding NADPH, DHF, and Ile5) (blue dotted line), the solvent/protein/DHF/Ile5 environment (excluding NADPH) (green solid line), and the complete electrostatic environment (red short-long dashed line).

molecules which are excluded from the QM region. Although the electronic effects of the protein environment are neglected in this model, the structural effects of the protein conformation on the local $[D_4]Y_{100}$ structure are taken into account. The resulting gas-phase spectrum is shown in Figure 10.7. As in the original spectra (Figure 10.6), the C-D stretches are characterized by a prominent central peak, in this case near 2350 cm^{-1}. Reorientation of the instantaneous dipole moment vector results in sharper peaks, giving rise to a shoulder just below 2350 cm^{-1} and a smaller peak at higher frequency, just below 2400 cm^{-1}. Recovery of the electrostatic charges of the bulk water molecules, counter ions, and protein residues (excluding Ile5 which is thought to hydrogen bond to

$[D_4]Y_{100}$) increases the intensity of the gas-phase peaks, but leaves the relative intensities of low to high frequency modes unchanged (Figure 10.7). Surprisingly, addition of the Ile5 MM charges has little effect on the solvent/protein spectrum, as does the inclusion of the DHF molecule in the QM region. This indicates little coupling between the frequency of Ile5 and DHF motions and the C-D stretching mode. Analysis of the O-O distance between $[D_4]Y_{100}$ phenolic oxygen and the oxygen of the Ile5 peptide bond suggests that hydrogen bonding is likely based on a typical hydrogen bond O-O distance of 2.8 – 3.0 Å.[179,180] Further inspection of the computed IR spectra indicates a significant reduction in intensity of a single peak near 3400 cm^{-1}, which is attributed to the O-H stretch of $[D_4]Y_{100}$ determined by Gaussian 09[139] frequency calculations on the isolated $[D_4]$Tyr

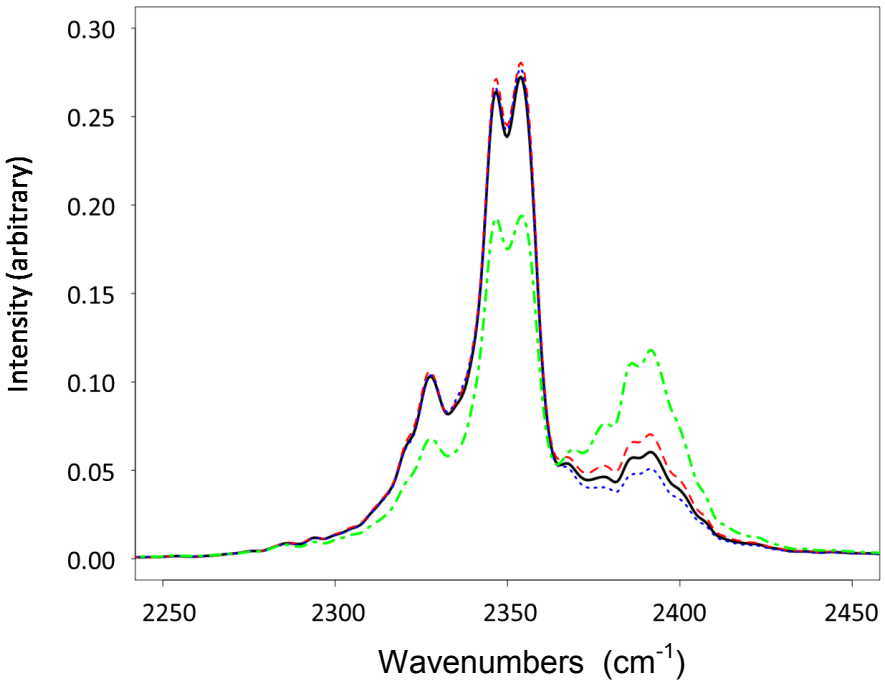

Figure 10.8 Similated IR spectra of $[D_4]Y_{100}$ in the reactant state of wt-DHFR hydride transfer catalysis, where the complete spectrum (black solid) is compared to those that neglect the electrostatic charges of Ile5 (red dashed) and the QM interactions of DHF (blue dotted) and NADPH (green dot-dashed).

residue systems. Thus, our electrostatic model captures the loss of the hydrogen bond acceptor, but it is not reflected in the C-D IR spectrum as anticipated.

Systematic analysis of individual molecules are necessary to identify the origin of the DHFR $[D_4]Y_{100}$ IR spectral shift. Starting with the original spectra recomputed using the reoriented instantaneous dipole moment vectors, Figure 10.8 shows the sequential removal and replacement of different molecule in the active site of wt-DHRF. Clearly, changes in the spectra are negligible for the zeroing of the Ile5 electrostatic charges and for removing DHF from the QM region. This confirms that an interaction between $[D_4]Y_{100}$ and NADPH is responsible for the observed shift in C-D stretching modes.

Additional IR spectra were computed for the product state wt-DHFR complex MD trajectories. The effects of removing THF and $NADP^+$, sequentially, from the QM

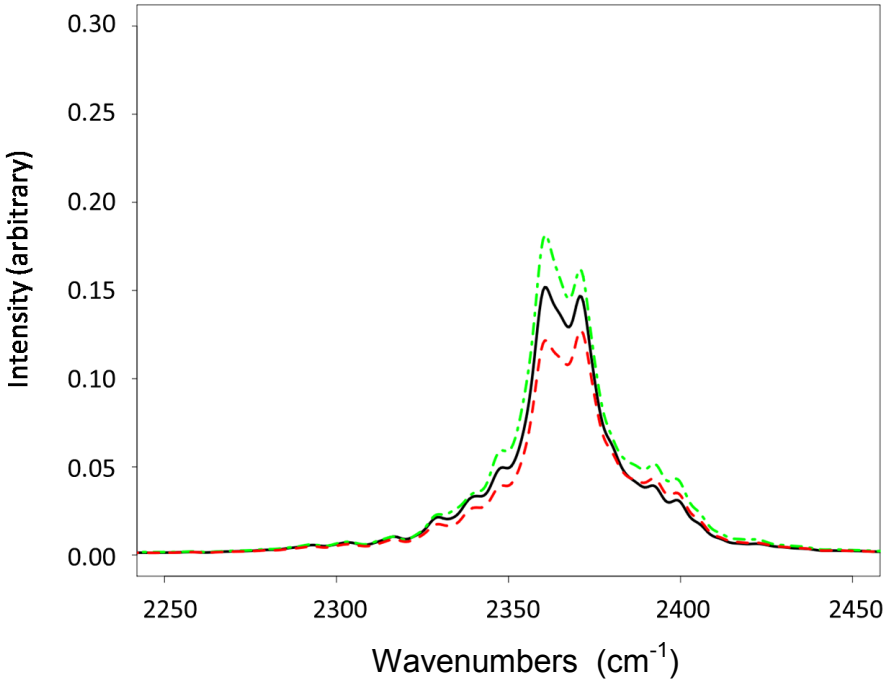

Figure 10.9 Similated IR spectra of $[D_4]Y_{100}$ in the product state of wt-DHFR hydride transfer catalysis, where the complete spectrum (black solid) is compared to those in which the QM interactions of THF (red dashed) and $NADP^+$ (green dot-dashed) have been removed.

region are shown in Figure 10.9 and indicate little change in the C-D spectrum for either of the QM-treated molecules in the product state.

10.6 Conclusions

These observations support a mechanism in which the Michaelis complex samples configurations that involve an electronic interaction between $[D_4]Y_{100}$ and NADPH. It has been suggested that the $[D_4]Y_{100}$ phenol stabilizes the developing positive charge on the NADPH as catalysis progresses from reactants to products.[41] Our results are consistent with this proposed mechanism. The distribution of electron density within the $[D_4]Y_{100}$ side chain is dependent on the inclusion of the electronic effects of the NADPH molecule in the reactant configurations. Interestingly, the product state does not exhibit the same spectral shifts and in fact shows very little dependence on the local electronic environment. To draw connections to previous studies on the dm-DHFR complex,[43] analysis of simulated C-D IR spectra is ongoing and the electrostatic and dynamical effects of the environment continue to be investigated for this catalytic mechanism.

Chapter 11. Bibliography

1. Keough, J. M., Jenson, D. L., Zuniga, A. N. & Barry, B. A. Proton Coupled Electron Transfer and Redox-Active Tyrosine Z in the Photosynthetic Oxygen-Evolving Complex. *J. Am. Chem. Soc.* **133,** 11084–11087 (2011).

2. Minnihan, E. C., Nocera, D. G. & Stubbe, J. Reversible, Long-Range Radical Transfer in E. coli Class Ia Ribonucleotide Reductase. *Acc. Chem. Res.* **46,** 2524–2535 (2013).

3. Njus, D., Wigle, M., Kelley, P. M., Kipp, B. H. & Schlegel, H. B. Mechanism of Ascorbic Acid Oxidation by Cytochrome b561. *Biochemistry* **40,** 11905–11911 (2001).

4. Keough, J. M., Zuniga, A. N., Jenson, D. L. & Barry, B. A. Redox Control and Hydrogen Bonding Networks: Proton-Coupled Electron Transfer Reactions and Tyrosine Z in the Photosynthetic Oxygen-Evolving Complex. *J. Phys. Chem. B* **117,** 1296–1307 (2013).

5. Offenbacher, A. R., Vassiliev, I. R., Seyedsayamdost, M. R., Stubbe, J. & Barry, B. A. Redox-Linked Structural Changes in Ribonucleotide Reductase. *J. Am. Chem. Soc.* **131,** 7496–7497 (2009).

6. Offenbacher, A. R., Burns, L. A., Sherrill, C. D. & Barry, B. A. Redox-Linked Conformational Control of Proton-Coupled Electron Transfer: Y122 in the Ribonucleotide Reductase β2 Subunit. *J. Phys. Chem. B* **117,** 8457–8468 (2013).

7. Barry, B. A., Chen, J., Keough, J., Jenson, D., Offenbacher, A. & Pagba, C. Proton-Coupled Electron Transfer and Redox-Active Tyrosines: Structure and Function of the Tyrosyl Radicals in Ribonucleotide Reductase and Photosystem II. *J. Phys. Chem. Lett.* **3,** 543–554 (2012).

8. Sjödin, M., Styring, S., Wolpher, H., Xu, Y., Sun, L. & Hammarström, L. Switching the Redox Mechanism: Models for Proton-Coupled Electron Transfer from Tyrosine and Tryptophan. *J. Am. Chem. Soc.* **127,** 3855–3863 (2005).

9. Litwinienko, G. & Ingold, K. U. Solvent Effects on the Rates and Mechanisms of Reaction of Phenols with Free Radicals. *Acc. Chem. Res.* **40,** 222–230 (2007).

10. Cukier, R. I. & Nocera, D. G. Proton-Coupled Electron Transfer. *Annual Review of Physical Chemistry* **49,** 337–369 (1998).

11. Hammes-Schiffer, S. & Stuchebrukhov, A. A. Theory of Coupled Electron and Proton Transfer Reactions. *Chem. Rev.* **110,** 6939–6960 (2010).

12. Mayer, J. M., Hrovat, D. A., Thomas, J. L. & Borden, W. T. Proton-Coupled Electron Transfer versus Hydrogen Atom Transfer in Benzyl/Toluene, Methoxyl/Methanol, and Phenoxyl/Phenol Self-Exchange Reactions. *J. Am. Chem. Soc.* **124,** 11142–11147 (2002).

13. Skone, J. H., Soudackov, A. V. & Hammes-Schiffer, S. Calculation of Vibronic Couplings for Phenoxyl/Phenol and Benzyl/Toluene Self-Exchange Reactions: Implications for Proton-Coupled Electron Transfer Mechanisms. *J. Am. Chem. Soc.* **128,** 16655–16663 (2006).

14. Tishchenko, O., Truhlar, D. G., Ceulemans, A. & Nguyen, M. T. A Unified Perspective on the Hydrogen Atom Transfer and Proton-Coupled Electron Transfer Mechanisms in Terms of Topographic Features of the Ground and Excited Potential Energy Surfaces As Exemplified by the Reaction between Phenol and Radicals. *J. Am. Chem. Soc.* **130,** 7000–7010 (2008).

15. Herrick, J. & Sclavi, B. Ribonucleotide reductase and the regulation of DNA replication: an old story and an ancient heritage. *Molecular Microbiology* **63,** 22–34 (2007).

16. Cerqueira, N. M. F. S. A., Pereira, S., Fernandes, P. A. & Ramos, M. J. Overview of Ribonucleotide Reductase Inhibitors: An Appealing Target in Anti-Tumour Therapy. *Current Medicinal Chemistry* **12,** 1283–1294 (2005).

17. Uhlin, U. & Eklund, H. Structure of ribonucleotide reductase protein R1. *, Published online: 18 August 1994; | doi:10.1038/370533a0* **370,** 533–539 (1994).

18. Nordlund, P., Sjöberg, B.-M. & Eklund, H. Three-dimensional structure of the free radical protein of ribonucleotide reductase. *Nature* **345,** 593–598 (1990).

19. Stubbe, J., Nocera, D. G., Yee, C. S. & Chang, M. C. Y. Radical Initiation in the Class I Ribonucleotide Reductase: Long-Range Proton-Coupled Electron Transfer? *Chem. Rev.* **103,** 2167–2202 (2003).

20. Kirby, J. P., Roberts, J. A. & Nocera, D. G. Significant Effect of Salt Bridges on Electron Transfer. *J. Am. Chem. Soc.* **119,** 9230–9236 (1997).

21. Gao, J., Ma, S., Major, D. T., Nam, K., Pu, J. & Truhlar, D. G. Mechanisms and Free Energies of Enzymatic Reactions. *Chem. Rev.* **106,** 3188–3209 (2006).

22. Garcia-Viloca, M., Gao, J., Karplus, M. & Truhlar, D. G. How Enzymes Work: Analysis by Modern Rate Theory and Computer Simulations. *Science* **303,** 186–195 (2004).

23. Nagel, Z. D. & Klinman, J. P. Tunneling and Dynamics in Enzymatic Hydride Transfer. *Chem. Rev.* **106,** 3095–3118 (2006).

24. Soudackov, A. & Hammes-Schiffer, S. Multistate continuum theory for multiple charge transfer reactions in solution. *The Journal of Chemical Physics* **111,** 4672–4687 (1999).

25. Hammes-Schiffer, S. Theoretical Perspectives on Proton-Coupled Electron Transfer Reactions. *Acc. Chem. Res.* **34,** 273–281 (2001).

26. Cukier, R. I. Proton-Coupled Electron Transfer Reactions: Evaluation of Rate Constants. *J. Phys. Chem.* **100,** 15428–15443 (1996).

27. Cukier, R. I. Mechanism for Proton-Coupled Electron-Transfer Reactions. *J. Phys. Chem.* **98,** 2377–2381 (1994).

28. Mayer, J. M. Simple Marcus-Theory-Type Model for Hydrogen-Atom Transfer/Proton-Coupled Electron Transfer. *J. Phys. Chem. Lett.* **2,** 1481–1489 (2011).

29. Song, L. & Gao, J. On the Construction of Diabatic and Adiabatic Potential Energy Surfaces Based on Ab Initio Valence Bond Theory†. *J. Phys. Chem. A* **112,** 12925–12935 (2008).

30. Cembran, A., Song, L., Mo, Y. & Gao, J. Block-Localized Density Functional Theory (BLDFT), Diabatic Coupling, and Their Use in Valence Bond Theory for Representing Reactive Potential Energy Surfaces. *J. Chem. Theory Comput.* **5,** 2702–2716 (2009).

31. Cembran, A., Provorse, M. R., Wang, C., Wu, W. & Gao, J. The Third Dimension of a More O'Ferrall–Jencks Diagram for Hydrogen Atom Transfer in the Isoelectronic Hydrogen Exchange Reactions of (PhX)2H• with X = O, NH, and CH2. *J. Chem. Theory Comput.* **8,** 4347–4358 (2012).

32. Cukier, R. I. Proton-Coupled Electron Transfer through an Asymmetric Hydrogen-Bonded Interface. *J. Phys. Chem.* **99,** 16101–16115 (1995).

33. Soudackov, A. & Hammes-Schiffer, S. Theoretical Study of Photoinduced Proton-Coupled Electron Transfer through Asymmetric Salt Bridges. *J. Am. Chem. Soc.* **121,** 10598–10607 (1999).

34. Warren, J. J. & Mayer, J. M. Tuning of the Thermochemical and Kinetic Properties of Ascorbate by Its Local Environment: Solution Chemistry and Biochemical Implications. *J. Am. Chem. Soc.* **132,** 7784–7793 (2010).

35. Sajenko, I., Pilepić, V., Jakobušić Brala, C. & Uršić, S. Solvent Dependence of the Kinetic Isotope Effect in the Reaction of Ascorbate with the 2,2,6,6-Tetramethylpiperidine-1-oxyl Radical: Tunnelling in a Small Molecule Reaction. *J. Phys. Chem. A* **114,** 3423–3430 (2010).

36. Truhlar, D. G., Isaacson, A. D. & Garrett, B. C. in *Theory of Chemical Reaction Dynamics* (ed. Baer, M.) 65–137 (CRC Press, 1985).

37. Mo, Y. & Gao, J. An Ab Initio Molecular Orbital−Valence Bond (MOVB) Method for Simulating Chemical Reactions in Solution. *J. Phys. Chem. A* **104,** 3012–3020 (2000).

38. Song, L., Mo, Y. & Gao, J. An Effective Hamiltonian Molecular Orbital-Valence Bond (MOVB) Approach for Chemical Reactions as Applied to the Nucleophilic Substitution Reaction of Hydrosulfide Ion and Chloromethane. *J. Chem. Theory Comput.* **5,** 174–185 (2009).

39. Chan, W.-L., Berkelbach, T. C., Provorse, M. R., Monahan, N. R., Tritsch, J. R., Hybertsen, M. S., Reichman, D. R., Gao, J. & Zhu, X.-Y. The Quantum Coherent Mechanism for Singlet Fission: Experiment and Theory. *Acc. Chem. Res.* **46,** 1321–1329 (2013).

40. Sawaya, M. R. & Kraut, J. Loop and Subdomain Movements in the Mechanism of Escherichia coli Dihydrofolate Reductase: Crystallographic Evidence†,‡. *Biochemistry* **36,** 586–603 (1997).

41. Groff, D., Thielges, M. C., Cellitti, S., Schultz, P. G. & Romesberg, F. E. Efforts Toward the Direct Experimental Characterization of Enzyme Microenvironments: Tyrosine100 in Dihydrofolate Reductase. *Angewandte Chemie International Edition* **48,** 3478–3481 (2009).

42. Garcia-Viloca, M., Truhlar, D. G. & Gao, J. Reaction-Path Energetics and Kinetics of the Hydride Transfer Reaction Catalyzed by Dihydrofolate Reductase†. *Biochemistry* **42,** 13558–13575 (2003).

43. Fan, Y., Cembran, A., Ma, S. & Gao, J. Connecting Protein Conformational Dynamics with Catalytic Function As Illustrated in Dihydrofolate Reductase. *Biochemistry* **52,** 2036–2049 (2013).

44. Berens, P. H. & Wilson, K. R. Molecular dynamics and spectra. I. Diatomic rotation and vibration. *The Journal of Chemical Physics* **74,** 4872–4882 (1981).

45. Miller, C. S. & Corcelli, S. A. Carbon−Deuterium Vibrational Probes of Amino Acid Protonation State. *J. Phys. Chem. B* **113,** 8218–8221 (2009).

46. Mayer, J. M. PROTON-COUPLED ELECTRON TRANSFER: A Reaction Chemist's View. *Annual Review of Physical Chemistry* **55,** 363–390 (2004).

47. Cukier, R. I. A Theory that Connects Proton-Coupled Electron-Transfer and Hydrogen-Atom Transfer Reactions†. *J. Phys. Chem. B* **106,** 1746–1757 (2002).

48. Warren, J. J., Tronic, T. A. & Mayer, J. M. Thermochemistry of Proton-Coupled Electron Transfer Reagents and its Implications. *Chem. Rev.* **110,** 6961–7001 (2010).

49. Litwinienko, G. & Ingold, K. U. Abnormal Solvent Effects on Hydrogen Atom Abstraction. 2. Resolution of the Curcumin Antioxidant Controversy. The Role of Sequential Proton Loss Electron Transfer. *J. Org. Chem.* **69,** 5888–5896 (2004).

50. Levich, V. G., Dogonadze, R. R., German, E. D., Kuznetsov, A. M. & Kharkats, Y. I. Theory of homogeneous reactions involving proton transfer. *Electrochimica Acta* **15,** 353–367 (1970).

51. Marcus, R. A. Chemical and Electrochemical Electron-Transfer Theory. *Annual Review of Physical Chemistry* **15,** 155 (1964).

52. Irebo, T., Zhang, M.-T., Markle, T. F., Scott, A. M. & Hammarstrom, L. Spanning Four Mechanistic Regions of Intramolecular Proton-Coupled Electron Transfer in a Ru(bpy)(3)(2+) - Tyrosine Complex. *J. Am. Chem. Soc.* **134,** 16247–16254 (2012).

53. Soudackov, A. & Hammes-Schiffer, S. Derivation of rate expressions for nonadiabatic proton-coupled electron transfer reactions in solution. *The Journal of Chemical Physics* **113,** 2385–2396 (2000).

54. Edwards, S. J., Soudackov, A. V. & Hammes-Schiffer, S. Analysis of Kinetic Isotope Effects for Proton-Coupled Electron Transfer Reactions†. *J. Phys. Chem. A* **113,** 2117–2126 (2009).

55. Hammes-Schiffer, S. & Soudackov, A. V. Proton-Coupled Electron Transfer in Solution, Proteins, and Electrochemistry†. *J. Phys. Chem. B* **112,** 14108–14123 (2008).

56. Hatcher, E., Soudackov, A. V. & Hammes-Schiffer, S. Proton-Coupled Electron Transfer in Soybean Lipoxygenase: Dynamical Behavior and Temperature Dependence of Kinetic Isotope Effects. *J. Am. Chem. Soc.* **129,** 187–196 (2007).

57. Hatcher, E., Soudackov, A. & Hammes-Schiffer, S. Nonadiabatic Proton-Coupled Electron Transfer Reactions: Impact of Donor−Acceptor Vibrations, Reorganization Energies, and Couplings on Dynamics and Rates. *J. Phys. Chem. B* **109,** 18565–18574 (2005).

58. Hazra, A., Soudackov, A. V. & Hammes-Schiffer, S. Role of Solvent Dynamics in Ultrafast Photoinduced Proton-Coupled Electron Transfer Reactions in Solution. *J. Phys. Chem. B* **114,** 12319–12332 (2010).

59. Soudackov, A., Hatcher, E. & Hammes-Schiffer, S. Quantum and dynamical effects of proton donor-acceptor vibrational motion in nonadiabatic proton-coupled electron transfer reactions. *The Journal of Chemical Physics* **122,** 014505 (2004).

60. Valero, R., Song, L., Gao, J. & Truhlar, D. G. Perspective on Diabatic Models of Chemical Reactivity as Illustrated by the Gas-Phase SN2 Reaction of Acetate Ion with 1,2-Dichloroethane. *J. Chem. Theory Comput.* **5,** 1–22 (2009).

61. Abraham, M. H., Grellier, P. L., Prior, D. V., Morris, J. J. & Taylor, P. J. Hydrogen bonding. Part 10. A scale of solute hydrogen-bond basicity using log K values for complexation in tetrachloromethane. *J. Chem. Soc., Perkin Trans. 2* 521–529 (1990). doi:10.1039/P29900000521

62. Snelgrove, D. W., Lusztyk, J., Banks, J. T., Mulder, P. & Ingold, K. U. Kinetic Solvent Effects on Hydrogen-Atom Abstractions: Reliable, Quantitative Predictions via a Single Empirical Equation1. *J. Am. Chem. Soc.* **123,** 469–477 (2001).

63. Litwinienko, G. & Ingold, K. U. Abnormal Solvent Effects on Hydrogen Atom Abstractions. 1. The Reactions of Phenols with 2,2-Diphenyl-1-picrylhydrazyl (dpph•) in Alcohols. *J. Org. Chem.* **68,** 3433–3438 (2003).

64. Foti, M. C., Daquino, C. & Geraci, C. Electron-Transfer Reaction of Cinnamic Acids and Their Methyl Esters with the DPPH• Radical in Alcoholic Solutions. *J. Org. Chem.* **69,** 2309–2314 (2004).

65. Foti, M. C. Solvent effects on the activation parameters of the reaction between an α-tocopherol analogue and dpph•: The role of H-bonded complexes. *International Journal of Chemical Kinetics* **44,** 524–531 (2012).

66. Mayer, J. M. Understanding Hydrogen Atom Transfer: From Bond Strengths to Marcus Theory. *Acc. Chem. Res.* **44,** 36–46 (2011).

67. Warren, J. J. & Mayer, J. M. Predicting organic hydrogen atom transfer rate constants using the Marcus cross relation. *PNAS* **107,** 5282–5287 (2010).

68. Mo, Y. & Peyerimhoff, S. D. Theoretical analysis of electronic delocalization. *The Journal of Chemical Physics* **109,** 1687–1697 (1998).

69. Mo, Y., Gao, J. & Peyerimhoff, S. D. Energy decomposition analysis of intermolecular interactions using a block-localized wave function approach. *The Journal of Chemical Physics* **112,** 5530–5538 (2000).

70. Cave, R. J. & Newton, M. D. Generalization of the Mulliken-Hush treatment for the calculation of electron transfer matrix elements. *Chemical Physics Letters* **249,** 15–19 (1996).

71. Cave, R. J. & Newton, M. D. Calculation of electronic coupling matrix elements for ground and excited state electron transfer reactions: Comparison of the generalized Mulliken–Hush and block diagonalization methods. *The Journal of Chemical Physics* **106,** 9213–9226 (1997).

72. Subotnik, J. E., Yeganeh, S., Cave, R. J. & Ratner, M. A. Constructing diabatic states from adiabatic states: Extending generalized Mulliken–Hush to multiple charge centers with Boys localization. *The Journal of Chemical Physics* **129,** 244101 (2008).

73. Subotnik, J. E., Cave, R. J., Steele, R. P. & Shenvi, N. The initial and final states of electron and energy transfer processes: Diabatization as motivated by system-solvent interactions. *The Journal of Chemical Physics* **130,** 234102 (2009).

74. Nakamura, H. & Truhlar, D. G. Direct diabatization of electronic states by the fourfold way. II. Dynamical correlation and rearrangement processes. *The Journal of Chemical Physics* **117,** 5576–5593 (2002).

75. Li, Z. H., Valero, R. & Truhlar, D. G. Improved direct diabatization and coupled potential energy surfaces for the photodissociation of ammonia. *Theor Chem Account* **118,** 9–24 (2007).

76. Thiel, A. & Köppel, H. Proposal and numerical test of a simple diabatization scheme. *The Journal of Chemical Physics* **110,** 9371–9383 (1999).

77. Sirjoosingh, A. & Hammes-Schiffer, S. Proton-Coupled Electron Transfer versus Hydrogen Atom Transfer: Generation of Charge-Localized Diabatic States. *J. Phys. Chem. A* **115,** 2367–2377 (2011).

78. Sirjoosingh, A. & Hammes-Schiffer, S. Diabatization Schemes for Generating Charge-Localized Electron–Proton Vibronic States in Proton-Coupled Electron Transfer Systems. *J. Chem. Theory Comput.* **7,** 2831–2841 (2011).

79. Mo, Y., Bao, P. & Gao, J. Energy decomposition analysis based on a block-localized wavefunction and multistate density functional theory. *Phys. Chem. Chem. Phys.* **13,** 6760–6775 (2011).

80. Mo, Y., Song, L. & Lin, Y. Block-Localized Wavefunction (BLW) Method at the Density Functional Theory (DFT) Level. *J. Phys. Chem. A* **111,** 8291–8301 (2007).

81. Dederichs, P. H., Blügel, S., Zeller, R. & Akai, H. Ground States of Constrained Systems: Application to Cerium Impurities. *Phys. Rev. Lett.* **53,** 2512–2515 (1984).

82. Kaduk, B., Kowalczyk, T. & Van Voorhis, T. Constrained Density Functional Theory. *Chemical Reviews* **112,** 321–370 (2012).

83. Wu, Q. & Voorhis, T. V. Extracting electron transfer coupling elements from constrained density functional theory. *The Journal of Chemical Physics* **125,** 164105 (2006).

84. Wu, Q., Cheng, C.-L. & Voorhis, T. V. Configuration interaction based on constrained density functional theory: A multireference method. *The Journal of Chemical Physics* **127,** 164119 (2007).

85. Wu, Q., Kaduk, B. & Voorhis, T. V. Constrained density functional theory based configuration interaction improves the prediction of reaction barrier heights. *The Journal of Chemical Physics* **130,** 034109 (2009).

86. Difley, S. & Van Voorhis, T. Exciton/Charge-Transfer Electronic Couplings in Organic Semiconductors. *J. Chem. Theory Comput.* **7,** 594–601 (2011).

87. Markle, T. F., Tenderholt, A. L. & Mayer, J. M. Probing Quantum and Dynamic Effects in Concerted Proton–Electron Transfer Reactions of Phenol–Base Compounds. *J. Phys. Chem. B* **116,** 571–584 (2012).

88. DiLabio, G. A. & Johnson, E. R. Lone Pair−π and π−π Interactions Play an Important Role in Proton-Coupled Electron Transfer Reactions. *J. Am. Chem. Soc.* **129,** 6199–6203 (2007).

89. Costentin, C., Robert, M. & Savéant, J.-M. Adiabatic and Non-adiabatic Concerted Proton−Electron Transfers. Temperature Effects in the Oxidation of Intramolecularly Hydrogen-Bonded Phenols. *J. Am. Chem. Soc.* **132,** 2845–2845 (2010).

90. Inagaki, T., Yamamoto, T. & Kato, S. Proton-coupled electron transfer of the phenoxyl/phenol couple: Effect of Hartree-Fock exchange on transition structures. *Journal of Computational Chemistry* **32,** 3081–3091 (2011).

91. Shaik, S. & Hiberty, P. C. *A Chemist's Guide to Valence Bond Theory*. (John Wiley & Sons, Inc., 2008).

92. Shaik, S. S. What happens to molecules as they react? A valence bond approach to reactivity. *J. Am. Chem. Soc.* **103,** 3692–3701 (1981).

93. Shaik, S. & Shurki, A. Valence Bond Diagrams and Chemical Reactivity. *Angewandte Chemie International Edition* **38,** 586–625 (1999).

94. Shaik, S. & Hiberty, P. C. *Review of Computational Chemistry* **20,** 1 (2004).

95. Li, C., Danovich, D. & Shaik, S. Blended hydrogen atom abstraction and proton-coupled electron transfer mechanisms of closed-shell molecules. *Chem. Sci.* **3,** 1903–1918 (2012).

96. Lai, W., Li, C., Chen, H. & Shaik, S. Hydrogen-Abstraction Reactivity Patterns from A to Y: The Valence Bond Way. *Angewandte Chemie International Edition* **51,** 5556–5578 (2012).

97. Cembran, A., Payaka, A., Lin, Y.-L., Xie, W., Mo, Y., Song, L. & Gao, J. A Non-Orthogonal Block-Localized Effective Hamiltonian Approach for Chemical and Enzymatic Reactions. *J. Chem. Theory Comput.* **6,** 2242–2251 (2010).

98. Mo, Y. & Gao, J. Ab initio QM/MM simulations with a molecular orbital-valence bond (MOVB) method: application to an SN2 reaction in water. *Journal of Computational Chemistry* **21,** 1458–1469 (2000).

99. Leininger, T., Stoll, H., Werner, H.-J. & Savin, A. Combining long-range configuration interaction with short-range density functionals. *Chemical Physics Letters* **275,** 151–160 (1997).

100. Ukai, T., Nakata, K., Yamanaka, S., Takada, T. & Yamaguchi, K. A CAS-DFT study of fundamental degenerate and nearly degenerate systems. *Molecular Physics* **105,** 2667–2679 (2007).

101. Kurzweil, Y., Lawler, K. V. & Head-Gordon, M. Analysis of multi-configuration density functional theory methods: theory and model application to bond-breaking. *Molecular Physics* **107,** 2103–2110 (2009).

102. Gao, J. & Truhlar, D. G. Quantum Mechanical Methods for Enzyme Kinetics. *Annual Review of Physical Chemistry* **53,** 467–505 (2002).

103. Pu, J., Gao, J. & Truhlar, D. G. Multidimensional Tunneling, Recrossing, and the Transmission Coefficient for Enzymatic Reactions. *Chem. Rev.* **106,** 3140–3169 (2006).

104. Major, D. T. & Gao, J. An Integrated Path Integral and Free-Energy Perturbation−Umbrella Sampling Method for Computing Kinetic Isotope Effects of Chemical Reactions in Solution and in Enzymes. *J. Chem. Theory Comput.* **3,** 949–960 (2007).

105. Chirgwin, B. H. & Coulson, C. A. The Electronic Structure of Conjugated Systems. VI. *Proc. R. Soc. Lond. A* **201,** 196–209 (1950).

106. Coulson, C. A. & Danielson, U. *Arkiv for fysik* **8,** 245 (1954).

107. Becke, A. D. Density-functional thermochemistry. III. The role of exact exchange. *The Journal of Chemical Physics* **98,** 5648–5652 (1993).

108. Lee, C., Yang, W. & Parr, R. G. Development of the Colle-Salvetti correlation-energy formula into a functional of the electron density. *Phys. Rev. B* **37,** 785–789 (1988).

109. Lingwood, M., Hammond, J. R., Hrovat, D. A., Mayer, J. M. & Borden, W. T. MPW1K Performs Much Better than B3LYP in DFT Calculations on Reactions that Proceed by Proton-Coupled Electron Transfer (PCET). *J. Chem. Theory Comput.* **2,** 740–745 (2006).

110. Cohen, A. J., Mori-Sánchez, P. & Yang, W. Insights into Current Limitations of Density Functional Theory. *Science* **321,** 792–794 (2008).

111. Lynch, B. J., Fast, P. L., Harris, M. & Truhlar, D. G. Adiabatic Connection for Kinetics. *J. Phys. Chem. A* **104,** 4811–4815 (2000).

112. Schmidt, M. W., Baldridge, K. K., Boatz, J. A., Elbert, S. T., Gordon, M. S., Jensen, J. H., Koseki, S., Matsunaga, N., Nguyen, K. A., Su, S., Windus, T. L., Dupuis, M. & Montgomery, J. A. General atomic and molecular electronic structure system. *Journal of Computational Chemistry* **14,** 1347–1363 (1993).

113. Porter, R. N., Stevens, R. M. & Karplus, M. Symmetric H3: A Semiempirical and Ab Initio Study of a Simple Jahn–Teller System. *The Journal of Chemical Physics* **49,** 5163–5178 (1968).

114. Shaik, S., Wu, W., Dong, K., Song, L. & Hiberty, P. C. Identity Hydrogen Abstraction Reactions, X• + H−X‘ → X−H + X‘• (X = X‘ = CH3, SiH3, GeH3, SnH3, PbH3): A Valence Bond Modeling. *J. Phys. Chem. A* **105,** 8226–8235 (2001).

115. Song, L., Mo, Y., Zhang, Q. & Wu, W. XMVB: A program for ab initio nonorthogonal valence bond computations. *Journal of Computational Chemistry* **26,** 514–521 (2005).

116. Song, L., Song, J., Mo, Y. & Wu, W. An efficient algorithm for energy gradients and orbital optimization in valence bond theory. *Journal of Computational Chemistry* **30,** 399–406 (2009).

117. Shaik, S., Schlegel, H. B. & Wolfe, S. *Theoretical Aspects of Physical Organic Chemistry: The SN2Mechanism*. (Wiley, 1992).

118. Shaik, S., Kumar, D., de Visser, S. P., Altun, A. & Thiel, W. Theoretical Perspective on the Structure and Mechanism of Cytochrome P450 Enzymes†. *Chem. Rev.* **105,** 2279–2328 (2005).

119. Wu, W., Su, P., Shaik, S. & Hiberty, P. C. Classical Valence Bond Approach by Modern Methods. *Chem. Rev.* **111,** 7557–7593 (2011).

120. Creutz, C. Complexities of ascorbate as a reducing agent. *Inorg. Chem.* **20,** 4449–4452 (1981).

121. Wayner, D. D. M., Burton, G. W., Ingold, K. U., Barclay, L. R. C. & Locke, S. J. The relative contributions of vitamin E, urate, ascorbate and proteins to the total peroxyl radical-trapping antioxidant activity of human blood plasma. *Biochimica et Biophysica Acta (BBA) - General Subjects* **924,** 408–419 (1987).

122. Kirsch, M. & Groot, H. de. Ascorbate Is a Potent Antioxidant against Peroxynitrite-induced Oxidation Reactions EVIDENCE THAT ASCORBATE ACTS BY RE-REDUCING SUBSTRATE RADICALS PRODUCED BY PEROXYNITRITE. *J. Biol. Chem.* **275,** 16702–16708 (2000).

123. Njus, D. & Kelley, P. M. The secretory-vesicle ascorbate-regenerating system: A chain of concerted H+/e−-transfer reactions. *Biochimica et Biophysica Acta (BBA) - Bioenergetics* **1144,** 235–248 (1993).

124. Nakanishi, N., Takeuchi, F. & Tsubaki, M. Histidine Cycle Mechanism for the Concerted Proton/Electron Transfer from Ascorbate to the Cytosolic Haem b Centre of Cytochrome b561: A Unique Machinery for the Biological Transmembrane Electron Transfer. *J Biochem* **142,** 553–560 (2007).

125. Warren, J. J. & Mayer, J. M. Surprisingly Long-Lived Ascorbyl Radicals in Acetonitrile: Concerted Proton−Electron Transfer Reactions and Thermochemistry. *J. Am. Chem. Soc.* **130,** 7546–7547 (2008).

126. O'Malley, P. J. Density Functional Calculations Modelling the Spin Density Distribution, Hyperfine Couplings, and Hydrogen Bonding Environment of the Ascorbate (Vitamin C) Free Radical. *J. Phys. Chem. B* **105,** 11290–11293 (2001).

127. Costanzo, F., Sulpizi, M., Vandevondele, J., Valle, R. G. D. & Sprik, M. Ab initio molecular dynamics study of ascorbic acid in aqueous solution. *Molecular Physics* **105,** 17–23 (2007).

128. Van Acker, S. A. B. E., de Groot, M. J., van den Berg, D.-J., Tromp, M. N. J. L., Donné-Op den Kelder, G., van der Vijgh, W. J. F. & Bast, A. A Quantum Chemical Explanation of the Antioxidant Activity of Flavonoids. *Chem. Res. Toxicol.* **9,** 1305–1312 (1996).

129. Gordon, M. & Schmidt, M. in *Theory and Applications of Computational Chemistry: the first forty years* (eds. Dykstra, C., Frenking, G., Kim, K. & Scuseria, G.) 1167–1189 (Elsevier, 2005).

130. Lin, Y. & Gao, J. Kinetic Isotope Effects of L-Dopa Decarboxylase. *J. Am. Chem. Soc.* **133,** 4398–4403 (2011).

131. Valgimigli, L., Ingold, K. U. & Lusztyk, J. Solvent Effects on the Reactivity and Free Spin Distribution of 2,2-Diphenyl-1-picrylhydrazyl Radicals1. *J. Org. Chem.* **61,** 7947–7950 (1996).

132. Valgimigli, L., Banks, J. T., Ingold, K. U. & Lusztyk, J. Kinetic Solvent Effects on Hydroxylic Hydrogen Atom Abstractions Are Independent of the Nature of the Abstracting Radical. Two Extreme Tests Using Vitamin E and Phenol. *J. Am. Chem. Soc.* **117,** 9966–9971 (1995).

133. Decornez, H. & Hammes-Schiffer, S. Model Proton-Coupled Electron Transfer Reactions in Solution: Predictions of Rates, Mechanisms, and Kinetic Isotope Effects. *J. Phys. Chem. A* **104,** 9370–9384 (2000).

134. Costentin, C., Robert, M. & Savéant, J.-M. Concerted Proton−Electron Transfers: Electrochemical and Related Approaches. *Acc. Chem. Res.* **43,** 1019–1029 (2010).

135. Marcus, R. A. Theoretical relations among rate constants, barriers, and Broensted slopes of chemical reactions. *J. Phys. Chem.* **72,** 891–899 (1968).

136. Miyoshi, A. *BEx1D*. (University of Tokyo, 2004) at <http://www.frad.t.u-tokyo.ac.jp/~miyoshi/bex1d/>.

137. Zheng, J., Zhang, S., Lynch, B. J., Corchado, J. C., Chuang, Y.-Y., Fast, P. L., Hu, W.-P., Liu, Y.-P., Lynch, G. C., Nguyen, K. A., Jackels, C. F., Ramos, A. F., Ellingson, B. A., Melissas, V. S., Villa, J., Rossi, I., Coitiño, E. L., Pu, J., Albu, T. V., Steckler, R., Garrett, B. C., Isaacson, A. D. & Truhlar, D. G. *POLYRATE*, version 2010. (University of Minnesota, 2010) at < http://comp.chem.umn.edu/polyrate/>.

138. Zheng, J., Zhang, S., Corchado, J. C., Chuang, Y.-Y., Coitiño, E. L., Ellingson, B. A. & Truhlar, D. G. *GAUSSRATE*, version 2009-A. (University of Minnesota, 2010) at < http://comp.chem.umn.edu/gaussrate/>.

139. Frisch, M. J., Trucks, G. W., Schlegel, H. B., Scuseria, G. E., Robb, M. A., Cheeseman, J. R., Scalmani, G., Barone, V., Mennucci, B., Petersson, G. A., Nakatsuji, H., Caricato, M., Li, X., Hratchian, H. P., Izmaylov, A. F., Bloino, J., Zheng, G., Sonnenberg, J. L., Hada, M., Ehara, M., Toyota, K., Fukuda, R., Hasegawa, J., Ishida, M., Nakajima, T., Honda, Y., Kitao, O., Nakai, H., Vreven, T., Montgomery, J. A., Jr., Peralta, J. E., Ogliaro, F., Bearpark, M., Heyd, J. J., Brothers, E., Kudin, K. N., Staroverov, V. N., Kobayashi, R., Normand, J., Raghavachari, K., Rendell, A., Burant, J. C., Iyengar, S. S., Tomasi, J., Cossi, M., Rega, N., Millam, N. J., Klene, M., Knox, J. E., Cross, J. B., Bakken, V., Adamo, C., Jaramillo, J., Gomperts, R., Stratmann, R. E., Yazyev, O., Austin, A. J., Cammi, R., Pomelli, C., Ochterski, J. W., Martin, R. L., Morokuma, K., Zakrzewski, V. G., Voth, G. A., Salvador, P., Dannenberg, J. J., Dapprich, S., Daniels, A. D., Farkas, Ö., Foresman, J. B., Ortiz, J. V., Cioslowski, J. & Fox, D. J. *Gaussian 09*, revision D.01. (Gaussian, Inc., 2009) at < http://www.gaussian.com/g_prod/g09.htm>.

140. Senn, H. M. & Thiel, W. QM/MM Methods for Biomolecular Systems. *Angewandte Chemie International Edition* **48,** 1198–1229 (2009).

141. Zimmerman, P. M., Bell, F., Casanova, D. & Head-Gordon, M. Mechanism for Singlet Fission in Pentacene and Tetracene: From Single Exciton to Two Triplets. *J. Am. Chem. Soc.* **133,** 19944–19952 (2011).

142. Yamagata, H., Norton, J., Hontz, E., Olivier, Y., Beljonne, D., Brédas, J. L., Silbey, R. J. & Spano, F. C. The nature of singlet excitons in oligoacene molecular crystals. *The Journal of Chemical Physics* **134,** 204703 (2011).

143. Burdett, J. J., Müller, A. M., Gosztola, D. & Bardeen, C. J. Excited state dynamics in solid and monomeric tetracene: The roles of superradiance and exciton fission. *The Journal of Chemical Physics* **133,** 144506 (2010).

144. Elstner, M., Porezag, D., Jungnickel, G., Elsner, J., Haugk, M., Frauenbheim, T., Suhai, S. & Seifert, G. Self-consistent-charge density-functional tight-binding method for simulations of complex materials properties. *Phys. Rev. B* **58,** 7260–7268 (1998).

145. Bernhard, P., Helm, L., Ludi, A. & Merbach, A. E. Direct measurement of a prominent outer-sphere electron self-exchange: kinetic parameters for the hexaaquaruthenium(II)/(III) couple determined by oxygen-17 and ruthenium-99 NMR. *J. Am. Chem. Soc.* **107,** 312–317 (1985).

146. Bader, J. S., Kuharski, R. A. & Chandler, D. Role of nuclear tunneling in aqueous ferrous–ferric electron transfer. *The Journal of Chemical Physics* **93,** 230–236 (1990).

147. Marchi, M. & Chandler, D. Path-integral calculation of the tunnel splitting in aqueous ferrous–ferric electron transfer. *The Journal of Chemical Physics* **95,** 889–894 (1991).

148. Campaña, A. G., Buñuel, E., Cuerva, J. M. & Cárdenas, D. J. The Role of Water-Based Hydrogen Atom Wires in Long-Range Electron-Transfer Reactions in Aqueous Media for the FeII–FeIII Self-Exchange and Related Systems. *Chem. Eur. J.* **19,** 16187–16191 (2013).

149. Brooks, B. R., Bruccoleri, R. E., Olafson, B. D., States, D. J., Swaminathan, S. & Karplus, M. CHARMM: A program for macromolecular energy, minimization, and dynamics calculations. *Journal of Computational Chemistry* **4,** 187–217 (1983).

150. Brooks, B. R., Brooks III, C. L., Mackerell, Jr., A. D., Nilsson, L., Petrella, R. J., Roux, B., Won, Y., Archontis, G., Bartels, C., Boresch, S., Caflisch, A., Caves, L., Cui, Q., Dinner, A. R., Feig, M., Fischer, S., Gao, J., Hodoscek, M., Im, W., Kuczera, K., Lazaridis, T., Ma, J., Ovchinnikov, V., Paci, E., Pastor, R. W., Post, C. B., Pu, J. Z., Schaefer, M., Tidor, B., Venable, R. M., Woodcock, H. L., Wu, X., Yang, W., York, D. M. & Karplus, M. CHARMM: The biomolecular simulation program. *Journal of Computational Chemistry* **30,** 1545–1614 (2009).

151. Zwanzig, R. Theory of Vibrational Relaxation in Liquids. *The Journal of Chemical Physics* **34,** 1931–1935 (1961).

152. Cui, Q., Elstner, M., Kaxiras, E., Frauenheim, T. & Karplus, M. A QM/MM Implementation of the Self-Consistent Charge Density Functional Tight Binding (SCC-DFTB) Method. *J. Phys. Chem. B* **105,** 569–585 (2001).

153. Zheng, G., Witek, H. A., Bobadova-Parvanova, P., Irle, S., Musaev, D. G., Prabhakar, R., Morokuma, K., Lundberg, M., Elstner, M., Köhler, C. & Frauenheim, T. Parameter Calibration of Transition-Metal Elements for the Spin-Polarized Self-Consistent-Charge Density-Functional Tight-Binding (DFTB) Method: Sc, Ti, Fe, Co, and Ni. *J. Chem. Theory Comput.* **3,** 1349–1367 (2007).

154. Jorgensen, W. L., Chandrasekhar, J., Madura, J. D., Impey, R. W. & Klein, M. L. Comparison of simple potential functions for simulating liquid water. *The Journal of Chemical Physics* **79,** 926–935 (1983).

155. MacKerell, Jr., A. D., Bashford, D., Bellowtt, M., Dunbrack, Jr., R. L., Evanseck, J. D., Field, M. J., Fisher, S., Gao, J., Guo, H., Ha, S., Joseph-McCarthy, D., Kuchnir, L., Kuczera, K., Lau, F. T. K., Mattos, C., Michnich, S., Ngo, T., Nguyen, D. T., Prodhom, B., Reiher, III, W. E., Roux, B., Schlenkrich, M., Smith, J. C., Stote, R., Straub, J., Watanabe, M., Wiórkiewicz-Kuczera, J., Yin, D. & Karplus, M. All-Atom Empirical Potential for Molecular Modeling and Dynamics Studies of Proteins†. *J. Phys. Chem. B* **102,** 3586–3616 (1998).

156. Beglov, D. & Roux, B. Finite representation of an infinite bulk system: Solvent boundary potential for computer simulations. *The Journal of Chemical Physics* **100,** 9050–9063 (1994).

157. Hoover, W. G. Canonical dynamics: Equilibrium phase-space distributions. *Phys. Rev. A* **31,** 1695–1697 (1985).

158. Nosé, S. A molecular dynamics method for simulations in the canonical ensemble. *Molecular Physics* **52,** 255–268 (1984).

159. Hockney, R. W. & Eastwood, J. W. *Computer Simulation Using Particles*. (McGraw-Hill, 1981).

160. Potter, D. *Computational Physics*. (Wiley, 1972).

161. Ryckaert, J.-P., Ciccotti, G. & Berendsen, H. J. C. Numerical integration of the cartesian equations of motion of a system with constraints: molecular dynamics of n-alkanes. *Journal of Computational Physics* **23,** 327–341 (1977).

162. Hilser, V. J. An Ensemble View of Allostery. *Science* **327,** 653–654 (2010).

163. Nashine, V. C., Hammes-Schiffer, S. & Benkovic, S. J. Coupled motions in enzyme catalysis. *Current Opinion in Chemical Biology* **14,** 644–651 (2010).

164. Schwartz, S. D. & Schramm, V. L. Enzymatic transition states and dynamic motion in barrier crossing. *Nat Chem Biol* **5,** 551–558 (2009).

165. Rajagopalan, P. T. R., Lutz, S. & Benkovic, S. J. Coupling Interactions of Distal Residues Enhance Dihydrofolate Reductase Catalysis: Mutational Effects on Hydride Transfer Rates†. *Biochemistry* **41,** 12618–12628 (2002).

166. Sikorski, R. S., Wang, L., Markham, K. A., Rajagopalan, P. T. R., Benkovic, S. J. & Kohen, A. Tunneling and Coupled Motion in the Escherichia coli Dihydrofolate Reductase Catalysis. *J. Am. Chem. Soc.* **126,** 4778–4779 (2004).

167. Boehr, D. D., McElheny, D., Dyson, H. J. & Wright, P. E. The Dynamic Energy Landscape of Dihydrofolate Reductase Catalysis. *Science* **313,** 1638–1642 (2006).

168. Liu, H. & Warshel, A. The Catalytic Effect of Dihydrofolate Reductase and Its Mutants Is Determined by Reorganization Energies†. *Biochemistry* **46,** 6011–6025 (2007).

169. Bhabha, G., Lee, J., Ekiert, D. C., Gam, J., Wilson, I. A., Dyson, H. J., Benkovic, S. J. & Wright, P. E. A Dynamic Knockout Reveals That Conformational Fluctuations Influence the Chemical Step of Enzyme Catalysis. *Science* **332,** 234–238 (2011).

170. Adamczyk, A. J., Cao, J., Kamerlin, S. C. L. & Warshel, A. Catalysis by dihydrofolate reductase and other enzymes arises from electrostatic preorganization, not conformational motions. *PNAS* **108,** 14115–14120 (2011).

171. Warshel, A., Sharma, P. K., Kato, M., Xiang, Y., Liu, H. & Olsson, M. H. M. Electrostatic Basis for Enzyme Catalysis. *Chem. Rev.* **106,** 3210–3235 (2006).

172. Marcus, R. A. Enzymatic catalysis and transfers in solution. I. Theory and computations, a unified view. *The Journal of Chemical Physics* **125,** 194504 (2006).

173. Marcus, R. A. H and Other Transfers in Enzymes and in Solution: Theory and Computations, a Unified View. 2. Applications to Experiment and Computations†. *J. Phys. Chem. B* **111,** 6643–6654 (2007).

174. Agarwal, P. K., Billeter, S. R., Rajagopalan, P. T. R., Benkovic, S. J. & Hammes-Schiffer, S. Network of coupled promoting motions in enzyme catalysis. *PNAS* **99,** 2794–2799 (2002).

175. Kinnaman, C. S., Cremeens, M. E., Romesberg, F. E. & Corcelli, S. A. Infrared Line Shape of an α-Carbon Deuterium-Labeled Amino Acid. *J. Am. Chem. Soc.* **128,** 13334–13335 (2006).

176. Miller, C. S., Ploetz, E. A., Cremeens, M. E. & Corcelli, S. A. Carbon-deuterium vibrational probes of peptide conformation: Alanine dipeptide and glycine dipeptide. *The Journal of Chemical Physics* **130,** 125103 (2009).

177. Yang, S. & Cho, M. IR spectra of N-methylacetamide in water predicted by combined quantum mechanical/molecular mechanical molecular dynamics simulations. *The Journal of Chemical Physics* **123,** 134503 (2005).

178. Dewar, M. J. S., Zoebisch, E. G., Healy, E. F. & Stewart, J. J. P. Development and use of quantum mechanical molecular models. 76. AM1: a new general purpose quantum mechanical molecular model. *J. Am. Chem. Soc.* **107,** 3902–3909 (1985).

179. Hibbert, F. & Emsley, J. in *Advances in Physical Organic Chemistry* (ed. D. Bethell) **Volume 26,** 255–379 (Academic Press, 1991).

180. Perrin, C. L. & Nielson, J. B. 'Strong' Hydrogen Bonds in Chemistry and Biology. *Annual Review of Physical Chemistry* **48,** 511–544 (1997).